

1 **In-Situ observation of New Particle Formation (NPF) in the tropical tropopause layer** 2 **of the 2017 Asian Monsoon Anticyclone - Part I: summary of StratoClim results**

3 Ralf Weigel¹, Christoph Mahnke^{2,8}, Manuel Baumgartner^{1,3}, Antonis Dragoneas^{1,2}, Bärbel Vogel⁴,
4 Felix Ploeger⁴, Silvia Viciani⁵, Francesco D'Amato⁵; Silvia Bucci⁶, Bernard Legras⁶, Beiping Luo⁷,
5 and Stephan Borrmann^{1,2}

6 ¹Institut für Physik der Atmosphäre, Johannes Gutenberg Universität, Mainz, Germany

7 ²Partikelchemie, Max-Planck-Institut für Chemie, Mainz, Germany

8 ³Zentrum für Datenverarbeitung, Johannes Gutenberg University, Mainz, Germany

9 ⁴Institute of Energy and Climate Research (IEK-7), Forschungszentrum Jülich, Jülich, Germany

10 ⁵National Institute of Optics - National Research Council (CNR-INO), Florence, Italy

11 ⁶Laboratoire de Météorologie Dynamique, UMR 8539, CNRS – École Normale Supérieure /
12 Université Pierre et Marie Curie / École Polytechnique, Paris, France

13 ⁷Swiss Federal Institute of Technology, Institute for Atmospheric Science, ETH Zurich,
14 Switzerland

15 ⁸now at the Institute of Energy and Climate Research (IEK-8), Forschungszentrum Jülich, Jülich,
16 Germany

17
18 Correspondence to: R. Weigel (weigelr@uni-mainz.de)

19 **Abstract**

20 During the monsoon season of the year 2017 the airborne StratoClim mission took place in
21 Kathmandu, Nepal with eight mission flights of the M-55 *Geophysica* in the upper troposphere /
22 lower stratosphere (UT/LS) of the Asian Monsoon Anticyclone (AMA) over northern India, Nepal
23 and Bangladesh. More than hundred events of New Particle Formation (NPF) were observed. In
24 total, more than two hours of flight time were spent under NPF conditions as indicated by the
25 abundant presence of nucleation-mode aerosols, i.e. with particle diameters d_p smaller than
26 15 nm, which were *in-situ* detected by means of condensation nuclei counting techniques.
27 Mixing ratios of nucleation-mode particles (n_{nm}) of up to $\sim 50000 \text{ mg}^{-1}$ were measured at heights
28 of 15 – 16 km ($\theta \approx 370 \text{ K}$). NPF was most frequently observed at $\sim 12 - 16 \text{ km}$ altitude ($\theta \approx 355 -$
29 380 K) and mainly below the tropopause. Resulting n_{nm} remained elevated ($\sim 300 - 2000 \text{ mg}^{-1}$)
30 up to altitudes of $\sim 17.5 \text{ km}$ ($\theta \approx 400 \text{ K}$) while under NPF conditions the fraction (f) of
31 submicrometre-sized non-volatile residues ($d_p > 10 \text{ nm}$) remained below 50 %. At $\sim 12 - 14 \text{ km}$
32 ($\theta \approx 355 - 365 \text{ K}$) the minimum of $f (< 15 \%)$ was found, and underneath, the median f generally
33 remains below 25 %. The persistence of particles at nucleation-mode sizes is limited to a few
34 hours, mainly due to coagulation, as demonstrated by a numerical simulation. The frequency of
35 NPF events observed during StratoClim 2017 underlines the importance of the AMA as a source
36 region for UT/LS aerosols and for the formation and maintenance of the ATAL. The observed
37 abundance of NPF-produced nucleation-mode particles within the AMA is not unambiguously
38 attributable to (a) specific source regions in the boundary layer (according to backward
39 trajectory analyses), or (b) the direct supply with precursor material by convective updraught

40 (from correlations of NPF with carbon monoxide), or (c) the recent release of NPF-capable
41 material from the convective outflow (according to air mass transport times in the TTL).
42 Temperature anomalies with ΔT of 2 K (peak-to-peak amplitude), as observed at a horizontal
43 wavelength of $\sim 70 - 100$ km during a level flight of several hours match with NPF detections
44 and represent an additional mechanism for local increases in supersaturation of the NPF
45 precursors. Effective precursor supply and widely distributed temperature anomalies within the
46 AMA can explain the higher frequency of intense NPF observed during StratoClim 2017 than all
47 previous NPF detections with COPAS at TTL levels over Brazil, Northern Australia, or West
48 Africa.

49 **1. Introduction**

50 Aerosol particles in the upper troposphere / lower stratosphere (UT/LS) influence the radiative
51 balance of the Earth's atmosphere, stratospheric chemistry, and properties of cirrus clouds near
52 the tropopause (Kremser et al., 2016). UT/LS aerosols are mainly composed of sulphuric acid
53 (H_2SO_4), nitric acid (HNO_3), water (H_2O), and organic compounds. Additionally, the particles
54 include fractions of non-volatile (or refractory) material (e.g. Froyd et al. (2010); Borrmann et
55 al. (2010); Murphy et al. (2014); Schneider et al. (2020)). Non-volatile components of
56 stratospheric aerosol particles originate from (1) natural tropospheric sources, e.g., volcanoes,
57 biomass burning, or pyro-cumulonimbus, (2) from meteoric ablation, or (3) they are
58 anthropogenic, as, for instance, space debris, rocket exhaust fumes, and products from
59 combustion (Kremser et al. (2016)). Chemical and microphysical processes, which involve the
60 stratospheric aerosol, could be influenced by solutes that, e.g., had previously been constituents
61 of the refractory aerosol compounds. Soot, mineral dust, fly ashes, metal-containing
62 condensates, inorganic salts, and other species probably make up the largest share of the non-
63 volatile components of aerosol particles in the UT/LS. In the tropics, underneath the tropopause,
64 the number of non-volatile fine-mode particles (i.e. smaller than $1 \mu\text{m}$ and larger than 10 nm in
65 diameter d_p) typically exhibits a characteristic minimum, resulting in a fraction of $\sim 20 \%$ (and
66 less) of non-volatile aerosol particles (cf. Borrmann et al. (2010); Weigel et al. (2011)). Above
67 the tropopause, at potential temperatures greater than $390 - 400 \text{ K}$, a maximum contribution of
68 non-volatile aerosol constituents seldom exceeds 50% (*ibid.*). Schneider et al. (2020) recently
69 provided laser ablation mass spectrometric analyses of refractory particles in the LS region
70 between the equator and the Arctic, which indicate detectable signatures of meteoric ablation

71 material at all sample locations in the LS. They assume that the meteoric ablation material is
72 partly present as solute or as insoluble inclusion within stratospheric H₂SO₄-H₂O-droplets.

73 In general, the typical particle size distribution of the stratospheric aerosol is characterised by
74 processes such as formation of new particles and their coagulation, the condensation of
75 saturated vapours, and the evaporation as well as removal when largest particles sediment. In
76 the tropics, above the level of zero net radiative heating where scavenging is lacking in the
77 absence of clouds, aerosol particles are available for isentropic dispersion or upward transport
78 into the stratosphere. Sedimentation or isentropic transport and mixing remove particles from
79 the stratosphere (Thomason and Peter (2006); Kremser et al. (2016)). Moreover, the aerosol
80 removal from the stratosphere occurs with particular efficiency via large-scale air mass
81 subsidence in the polar winter vortex in both, the Arctic (Weigel et al., 2014) and the Antarctic
82 (Campbell and Deshler, 2014).

83 The process of New Particle Formation (NPF), is considered as one of the most important
84 sources of the H₂SO₄-H₂O solution droplets prevailing in the UT and Tropical Tropopause Layer
85 (TTL) (Brock et al., 1995). The reservoir of stratospheric H₂SO₄ is maintained by oxidation of
86 gaseous precursors like sulphur dioxide (SO₂), carbonyl sulphide (OCS), and carbon disulphide
87 (CS₂), or dimethyl sulphide (C₂H₆S) (Thomason and Peter (2006); Kremser et al. (2016)). These
88 species can originate from sea surface emissions, from volcanism or from anthropogenic
89 pollution, and they often undergo long range transport before reaching the TTL (e.g. Law et al.,
90 2010). Sporadically, explosive volcanism injects large quantities of SO₂ directly into the
91 stratosphere. Weaker volcanic eruptions (with a mean vertical explosion index of about four)
92 also contribute significantly by delivering volcanic sulphur species indirectly via the TTL into
93 higher altitudes (Vernier et al. (2011b); Kremser et al. (2016)). Although SO₂ is efficiently bound
94 within clouds during convective uplift and dissolved in cloud hydrometeors, cloud-resolving
95 model calculations suggest that SO₂ proportions, which range from only 30 % (Ekman et al.,
96 2006) until up to 40-90 % (Barth et al., 2001), reach the outflow region of deep convection
97 largely consistent with estimates by Crutzen and Lawrence (2000). Laboratory investigations by
98 Jost et al. (2017) yielded a comparatively moderate retention coefficient (0.2 – 0.5) of SO₂ in the
99 ice phase of clouds, compared to a retention of 100 % for hydrochloric acid (HCl) and for nitric
100 acid (HNO₃) (*ibid.*). Hence, large fractions of the in-cloud dissolved SO₂ leave the cloud ice

101 composite as soon as the cloud particles freeze or when riming occurs. Alternatively, the SO₂,
102 which remains in the cloud ice composite, is entirely released when the ice particles sublimate in
103 the convective outflow region, or below, while the ice particles sediment. Rollins et al. (2017)
104 presented the results of *in-situ* SO₂ measurements at up to 19 km altitude over the Gulf of Mexico
105 and compared these with both model results and satellite observations. Generally, at altitudes
106 between 8 and 15 km, the mean values of SO₂ mixing ratio vary between 5 and 800 pmol mol⁻¹ in
107 the northern hemisphere, between 8 and 120 pmol mol⁻¹ in the tropics, and between 5 and
108 20 pmol mol⁻¹ in the southern hemisphere (Kremser et al., 2016). Enhanced SO₂ mixing ratios in
109 the vicinity of the tropopause are often observed in connection with the uplift of polluted air
110 masses by Warm Conveyor Belts (WBC) (*ibid.*). Apart from sulphuric acid, also other species
111 contribute to particle nucleation and growth, such as organics (Metzger et al. (2010); Kerminen
112 et al. (2010)), amines (Kürten et al. (2018)) or ammonia (e.g. Kirkby et al. (2011); Kürten
113 (2019)). Given the amount of organics (Murphy et al. (2006)) and ammonia species (Höpfner et
114 al. (2019); Stroh and the StratoClim group (2021)), which were found in aerosol particles at
115 UT/TTL heights in the AMA during the StratoClim 2017 mission, such compounds can act as
116 agents promoting NPF in the UT and TTL region.

117 **1.1 New particle formation**

118 New Particle Formation (NPF), comprises (1) the initial combination of molecules into clusters
119 (of ~ 1 nm diameter) and (2) their subsequent growth to larger diameters (Kulmala et al., 2013).
120 Nucleation mode aerosol particles with diameter (d_p) of at least 3 nm frequently form in
121 considerable quantities from gaseous precursors. Once formed, the particles are subject to
122 altering processes (e.g. coagulation, growth by condensation of water vapour and other gases,
123 evaporation, and scavenging). Within the entire atmosphere, NPF seems ubiquitous as was
124 demonstrated by various studies and observations of NPF's occurrence:

- 125 • at or close to the surface (Kulmala et al. (2004); Nieminen et al. (2018)),
- 126 • at elevated altitudes within the boundary layer (e.g. Bianchi et al. (2021); Sellegri et al.
127 (2019); Wehner et al. (2015), Crumeyrolle et al. (2010); Venzac et al. (2008)),
- 128 • in the boundary layer and in the free troposphere under the direct influence by volcanic
129 activity (e.g. Sahyoun et al. (2019)),

130 • up to tropopause altitudes and the TTL region (Kerminen et al. (2018); Williamson et al.
131 (2018); Williamson et al. (2019).

132 Modelling studies suggest that the NPF process constitutes one of the most important
133 contributions (up to 45 %) to global mean tropospheric concentrations of Cloud Condensation
134 Nuclei (CCN) activated at 0.2 % supersaturation (Merikanto et al., 2009). Uncertainties remain
135 concerning the effectiveness of NPF, which complicates the implementation of the NPF
136 mechanism in global scale simulations of aerosol number densities (Yu et al. (2010), Zhang et al.
137 (2010)). Chamber experiments, conducted at temperatures similar to those prevailing in the UT,
138 and also numerical simulations confirm that the UT constitutes an important source region for
139 atmospheric particles (Kürten et al. (2016), Dunne et al. (2016)).

140 Based on airborne *in-situ* observations of high particle number concentrations together with
141 high levels of particle volatility in the cloud-free tropical UT, the conditions of NPF occurrence
142 were described for the first time by Brock et al. (1995). Between 7 and 20 km altitude, fields of
143 recent NPF events were encountered in about 20 % of the probed flight segments (Lee et al.
144 (2004)). High NPF productivity with largest n_{nm} was observed particularly at the bottom TTL, as
145 shown by airborne measurements during missions over Brazil and over North Australia (Weigel
146 et al. (2011)). Recently, a survey of NPF occurrence in the free troposphere (~ 0.2 - 12 km
147 altitude) suggests that the NPF-produced particles persist (zonally almost invariant) as a
148 globally extending band within the tropical UT, thereby covering 40 % of the Earth's surface
149 (Williamson et al., 2019). At altitudes between 12 and 20 km within the tropics, this had also
150 been reported by Borrmann et al. (2010).

151 Between 27 July and 10 August 2017, during the Asian monsoon season, a total of eight scientific
152 flights with the high-altitude research aircraft M-55 *Geophysica* over parts of the Indian
153 subcontinent were performed from Kathmandu, Nepal (27° 42' 3" N, 85° 21' 42" E) during the
154 StratoClim 2017 mission (see Figure 1, and see also Stroh and the StratoClim group (2021)).
155 Some of these flights partly spanned out of Nepalese airspace, to East India, Bangladesh, and to
156 the northern part of the Bay of Bengal. During StratoClim 2017, NPF was frequently observed in
157 the presence of ice cloud particles within cirrus or in anvils of the convective outflow and is
158 discussed in detail in the companion paper (Weigel et al., 2021b). Based on these observations
159 during StratoClim 2017, NPF turned out as largely unaffected by faint ice clouds that typically

160 occur in TTL (*ibid.*). This study aims at discussing the NPF encounters in their entirety as
161 observed during the StratoClim 2017 mission in the UT and TTL region at altitudes of up to
162 20 km in the Asian Monsoon Anticyclone.

163 **1.2 The Asian Monsoon Anticyclone and the ATAL**

164 The Asian Monsoon Anticyclone (AMA) represents one of the most important circulation
165 systems in the UT/LS associated with deep convection over the Indian subcontinent and beyond.
166 From the beginning of June until about the end of August, the large-scale anticyclone persists at
167 altitudes from the UT to the LS regions (e.g. Randel and Park (2006), Park et al. (2007)),
168 extending over longitudes from East Asia to the Middle East/ East Africa (e.g. Vogel et al. (2014),
169 Vogel et al. (2019)). The anticyclonic rotation of the system induces confinement of air inside the
170 AMA's interior (Ploeger et al. (2015)). Air masses in the region of the Asian monsoon are rapidly
171 lifted by convection up to the maximum level of convective outflow (~ 360 K, corresponding to
172 ~ 13 km) followed by a slow diabatic lift superimposed on the anticyclonic motion (e.g. Vogel et
173 al. (2019)). Within the AMA, young air is transported to UT/LS altitudes during boreal summer
174 and in this way various pollutants and other gaseous material (Glatthor et al. (2015); Chirkov et
175 al. (2016); Pan et al. (2016); Santee et al. (2017)) and in particular water vapour (Ploeger et al.
176 (2013)) are lifted into the UT/LS region. Based on satellite studies, the existence of the aerosol
177 layer at tropopause altitudes within the AMA region (ATAL – Asian Tropopause Aerosol Layer)
178 was demonstrated (Vernier et al. (2011a); Thomason and Vernier (2013)). The existence of the
179 ATAL was further confirmed by *in-situ* balloon-borne backscatter measurements between 2013
180 and 2017 at different locations nearby the AMA centre (Vernier et al. (2015); Vernier et al.
181 (2018); Brunamonti et al. (2018); Hanumanthu et al. (2020)) and recent aircraft measurements
182 of Mahnke et al. (2021) or Fujiwara et al. (2021).

183 Hence, the constituents of the rising young air also include precursor material from
184 anthropogenic (Vernier et al. (2015), Yu et al. (2015)) and other sources. The NPF process in the
185 TTL region could contribute significantly to the formation and persistence of ATAL as a source of
186 additional aerosol material (He et al., 2019). Once the boundary layer material has reached
187 UT/LS levels within the AMA, the elevated tropopause potential temperature during the
188 monsoon season allows the material's isentropic dispersion into the “overworld” stratosphere
189 (Pan et al. (2016)). Three-dimensional simulations with the Chemical Lagrangian Model of the

190 Stratosphere (CLaMS) and backward trajectory analyses show that by end of August, during the
191 2008 monsoon season, air masses younger than 6 months reach the top of the AMA at about
192 460 K potential temperature (corresponding to ~ 60 hPa). According to these simulations (Vogel
193 et al. (2019)), air masses are lifted due to diabatic (radiative) heating in an anticyclonic large-
194 scale upward spiral with ascent rates of about 1 K potential temperature per day across the
195 tropopause consistent with the conclusions of previous works (Bergman et al. (2012), Garny and
196 Randel (2016), Ploeger et al. (2017)).

197 **2 *In-situ* instrumentation**

198 **2.1 Total number concentration of sub-micrometre sized particles**

199 Particle number concentrations were *in-situ* measured in 1 Hz resolution by means of a 4-
200 channel condensation nuclei (CN) counter COPAS (COndensation PArTicle counting System, cf.
201 Weigel et al. (2009)). For reduction of the statistical noise, the COPAS 1 Hz-raw data (direct
202 signal of the scattered-light-detectors) are preprocessed by applying a 15-second running
203 average. Three of the four COPAS channels operate with different 50 % detection particle
204 diameters d_{p50} (i.e. 6 nm, 10 nm and 15 nm). The fourth COPAS channel (with $d_{p50} = 10$ nm)
205 detects particles downstream of a heated (270°C) sample flow line, resulting in measured
206 particle mixing ratios of non-volatile (nv) particle residues or refractory particles (e.g. soot,
207 mineral dust, metallic particle material, etc.).

208 **2.1.1 COPAS operation during StratoClim 2017**

209 The sampling is carried out via the forward facing aerosol inlet of COPAS well outside the
210 boundary layer of the aircraft. For stratospheric particle concentrations, the COPAS
211 measurement uncertainty of the StratoClim 2017 data discussed herein is about 15%, which is
212 due to particle counting statistics and uncertainties in the volume flow. The measurement
213 properties of COPAS are described in detail by Weigel et al. (2009), and its performance has
214 been demonstrated by several studies (Curtius et al. (2005); de Reus et al. (2009); Borrmann et
215 al. (2010); Frey et al. (2011); Weigel et al. (2011), and Weigel et al. (2014)).

216 For StratoClim 2017, a new inlet configuration was used, allowing both COPAS instruments to
217 sample through a single aerosol inlet, resulting in an almost doubled flow velocity through the

218 sample tubes and reduced diffusional particle loss. This setup required the reanalysis of the
219 corrections to account for particle loss (Table 1) using the method introduced by von der Weiden et al. (2009) with modifications for
220 low-pressure application. One of the four COPAS channels detects particle number densities of
221 non-volatile particle residues downstream of a heated stainless steel tube (at $\sim 270^\circ\text{C}$)
222 (Appendix A)

224 **2.1.2 NPF identification: definitions and notations**

225 The particle densities are typically measured by COPAS in particle number concentrations N (in
226 cm^{-3} , ambient conditions), but are also presented here as mixing ratio n in units of particles per
227 milligram of air (mg^{-1}) for consistent comparisons of measurements from different pressure
228 levels and for correlations with the mixing ratios of gaseous tracers. Hereafter, the notation n_{10}
229 refers to the mixing ratio of sub-micrometre sized particles with diameters greater than 10 nm.
230 The measurement of n_6 (of particles with $d_p > 6$ nm) and n_{15} ($d_p > 15$ nm) allows for the
231 identification of recent NPF. The notation $n_{10\text{NV}}$ refers to the mixing ratio of non-volatile
232 particles (Appendix A) with corresponding size range as specified for n_{10} . The proportion f of
233 non-volatile particles is given as the ratio $\frac{n_{10\text{NV}}}{n_{10}}$ in percent.

234 Elevated number concentrations N_{nm} of nucleation-mode particles (defined as $N_6 - N_{15} = N_{6-15}$)
235 serve as an indication of recent NPF when additionally the NPF criterion (Equ. 1) is met:

$$236 \quad 0.8 \cdot N_6 - 1.2 \cdot N_{15} > 0. \quad (1)$$

237 This criterion was reassessed for the StratoClim 2017 data set based on the definition used by
238 Weigel et al. (2011) to account for the COPAS detectors' signal-to-noise ratio and the counting
239 statistics. The NPF criterion therefore sets a conservative threshold (*ibid.*) that additionally
240 accounts for the full range of data scattering (i.e. 20 % over periods of invariable N) that exceeds
241 the 15 % uncertainty of the concentrations measured with COPAS. The strict criterion
242 suppresses artificial features that mainly result from the scattering of the measured
243 concentrations and the criterion constrains the data set to the most significant of those that
244 were interpreted as NPF events. Calculated N_{6-15} are then corrected concerning particles'
245 diffusional loss inside the aerosol lines as described in Section 2.1.1 (cf. also Table 1). The

246 calculated number concentrations N_{6-15} are corrected by multiplying the factor κ_L (Table 1),
247 which is a function of the static pressure during the measurements.

248 Provided that the NPF criterion is met, a series of measurement points is denoted as NPF event if
249 the measured number concentration (or mixing ratio) of nucleation-mode particles remains
250 continuously greater than zero for at least five seconds of measurement. In total, 25 cases out of
251 130 individual events had a duration of less than five seconds, therefore for these 25 the number
252 of newly formed particles and the feature duration are uncertain. Mainly those features that are
253 much too short (e.g. lasting only one second) are filtered out by applying the NPF event
254 definition. Based on the mean airspeed and maximum ascent/descent rates of the M-55
255 *Geophysica* ($\sim 154 \pm 39 \text{ m s}^{-1}$; up to 10 m s^{-1}), this definition implies that a feature of elevated
256 N_{nm} lasting over five seconds extends over a horizontal distance of $\sim 770 \text{ m}$ (at constant course)
257 or vertically over up to 50 m.

258 The period of flight time during which the event criterion (Equation 1) is met is referred to as
259 the NPF event duration. From this information, the mean airspeed is used to infer the horizontal
260 extent of NPF fields - with caveats. Such estimates are limited by the assumption that an
261 encounter of elevated N_{nm} (over tens of seconds and minutes) is actually due to a single NPF
262 event and does not consist of a series of possibly overlapping events. In addition, the determined
263 horizontal distances refer to an average flight speed ($\sim 154 \pm 39 \text{ m s}^{-1}$) and the flight attitude is
264 assumed as unchanged during the event duration.

265 NPF events are distinguished by the peak number density of detected nucleation-mode particles
266 and are denoted as

- 267 • *intense* (often used synonymously with *most recent* NPF) if n_{nm} exceeds 10000 mg^{-1} ,
- 268 • *intermediate* for NPF with $1000 \text{ mg}^{-1} < n_{nm} < 10000 \text{ mg}^{-1}$, and
- 269 • *weak* NPF when detected n_{nm} remained below 1000 mg^{-1} , respectively.

270 This classification refers to laboratory studies by (Kirkby et al. (2011), Kürten et al. (2016)),
271 according to which the NPF-rate and the NPF intensity (i.e. its new particle productivity) varies
272 with the degree of supersaturation of the vapour from which the new particles form. Due to the
273 short persistence of the freshly formed particles in the nucleation mode (cf. Section 4.5), an
274 intense NPF event is still proceeding when observed, or it had phased-out very recently (within

275 hours) before the detection. For encounters of weak or intermediate NPF the conclusions
276 concerning the event's age remain ambiguous.

277 **2.2 Particle size distributions from the Ultra-High Sensitive Aerosol** 278 **Spectrometer UHSAS-A**

279 The measurements of the aerosol particle size distributions during StratoClim 2017 were
280 performed with an in-house modified airborne version of the Ultra High Sensitive Aerosol
281 Spectrometer (UHSAS-A; manufacturer DMT Inc., Longmont, CO, USA). The modifications on the
282 flow and pumping system of the UHSAS-A enabled maintaining constant system-flows (sample-,
283 sheath-, purge-flow) through the instrument even under ambient pressures as low as 50 hPa.
284 Details concerning the modified airflow system of the UHSAS-A, the characterisation of the
285 instrument's particle sizing performance and its calibration during the campaign period is
286 provided by Mahnke et al. (2021). The uncertainty of the number concentration measured by
287 the UHSAS-A with 1 Hz resolution was determined to be $\sim 10\%$ for the particle diameter range
288 of $65\text{ nm} < d_p < 1000\text{ nm}$, based on laboratory characterisations of the sample-flow
289 measurement and of the counting efficiency of the instrument (*ibid.*). Due to the unknown in-line
290 temperature of the sample and the wide ambient temperature range throughout
291 StratoClim 2017, a maximum uncertainty of the UHSAS-A measurements is estimated at 25%.
292 Some of the results from the measured particle size distributions and a comparison with other
293 instruments and the Cloud-Aerosol Lidar with Orthogonal Polarization (CALIOP) are presented
294 by Mahnke et al. (2021).

295 **2.3 Carbon monoxide (CO) measurements**

296 During the StratoClim 2017 mission, CO mixing ratios were determined by means of the tunable
297 diode laser (TDL) detection principle, which the analyser Carbon Oxide Laser Detector-2 (COLD-
298 2) spectrometer is based on. According to comprehensive comparisons to the previous
299 instrument version COLD (Cryogenically Operated Laser Diode, 4 s temporal resolution, (Viciani
300 et al., 2008)), the new system implies several improvements (Viciani et al., 2018). The
301 measurement's temporal resolution is improved by a factor of four, the in-flight sensitivity of the
302 COLD-2 spectrometer ranges at about 2 nmol mol^{-1} at integration times of 1 s, and an accuracy of
303 3% is specified for the CO measurement with COLD-2 (Viciani et al., 2018).

304 **2.4 Meteorological measurements**

305 Atmospheric temperature and pressure data were taken from the Unit for Connection with the
306 Scientific Equipment (UCSE, Sokolov and Lepuchov (1998)), which is a part of the avionic system
307 of the M-55 *Geophysica*. UCSE data are available as 1 Hz-resolved ambient pressure (accuracy:
308 ± 1 hPa) and temperature (± 2 K accuracy). Based on these UCSE data, the potential temperature
309 θ along the mission flight tracks is calculated in compliance with the definition by the World
310 Meteorological Organization (WMO (1966)). For the given vertical temperature gradients and
311 for the θ -range over which the StratoClim 2017 flights extended (i.e. up to ~ 477 K), the WMO
312 recommended calculation of θ differs at the most by up to ~ 1 K from the values obtained when
313 using the recently reappraised θ -calculation (Baumgartner et al., 2020).

314 **3 Analytical methods**

315 **3.1 The height of the lapse-rate tropopause and the equivalent latitude**

316 Meteorological data were also taken from ERA-Interim reanalyses by the European Centre of
317 Medium-Range Weather Forecasts (ECMWF) (Dee et al., 2011). Hybrid reanalysis levels in the
318 TTL are located at various pressure heights (i.e. around 177, 154, 133, 113, 96, 80, 67, 55 hPa,
319 respectively) representing a vertical resolution of about one kilometre in this region.

320 The aircraft data are analysed in coordinates relative to the tropopause height and to the
321 monsoon anticyclone center, respectively. The height of the lapse-rate based thermal
322 tropopause was determined based on ERA-Interim data and following the WMO criterion (WMO,
323 1957)The potential temperature θ at tropopause level was interpolated to the 1 Hz-resolved
324 position along the flight track of the M-55 *Geophysica*, and the measurement data were sorted as
325 a function of θ -distance ($\Delta\theta$) to the local tropopause as vertical coordinate.

326 The centre of the AMA was determined based on the anomalous potential vorticity distribution
327 within the monsoon region at the 380 K potential temperature level, where lowest values of the
328 potential vorticity (PV) are found in the AMA centre. The AMA-centred equivalent latitude was
329 calculated for a given closed PV contour as a projection onto polar coordinates (Ploeger et al.,
330 2015). An equivalent latitude of 90° North corresponds to the center of the anticyclone (lowest
331 PV), and the equivalent latitude decreases with increasing distance from the centre, or rather,
332 towards the anticyclone's edge. Note, that the calculation of AMA-centred equivalent latitude is
333 valid within a layer of about ± 10 K around 380 K potential temperature, where a clear negative

334 PV anomaly occurs. The uncertainties of calculated equivalent latitude become significant at
335 levels beyond the ± 30 K range above/below 380 K.

336 **3.2 The Coagulation Model for investigating the particles' persistence in the nucleation** 337 **mode**

338 The model employed in this study numerically solves the discretised coagulation equation (cf.,
339 e.g., Jacobson (2005) and Equation 15.2 therein) as formulated in the numerical chemistry-
340 climate model SOCOL (Solar Climate Ozone Links; Stenke et al. (2013)). For the coagulation of
341 nucleation-mode aerosol particles the Brownian coagulation kernel (Jacobson (2005), Equation
342 15.33 therein) is used. The particles are assumed as spherical, and the model is based on a
343 discretisation of the volume space, wherein the ratio of two subsequent volume size bins is
344 constant, $\frac{V_{k+1}}{V_k} = 1.4$. The particle size range of the first volume size-bin V_1 corresponds to
345 particle diameters of $7.5 \text{ nm} < d_{p,1} < 8.5 \text{ nm}$. With a total number of 40 size bins, the largest
346 particle size included in this investigation is about 635 nm ($= d_{p,40} = (1.4)^{\frac{39}{3}} \cdot d_{p,1}$).

347 The coagulation rate and, thus, the persistence of the nucleation-mode particles, was simulated
348 under given background conditions during observation. As input for the simulation, the aerosol
349 size distribution detected by the UHSAS-A (nominally covering $65 \text{ nm} < d_p < 1000 \text{ nm}$, cf. Section
350 2.2 and Mahnke et al. (2021)) was extended towards smaller diameters by further particle size
351 bins obtained from the measurements with COPAS. For the simulation presented herein, the NPF
352 event on 04 August 2017 (KTM 5) over 26 seconds between 04:04:40 and 04:05:06 UTC
353 (pressure altitude: 110 hPa; ambient air temperature: 196 K) was selected. Each of the two size
354 size intervals of the COPAS measurements in the nucleation mode, i.e. $6 \text{ nm} < d_p < 10 \text{ nm}$ and
355 $10 \text{ nm} < d_p < 15 \text{ nm}$, is divided into three subintervals to adapt to the higher particle size
356 resolution of the coagulation model. The three sub-bins within the size classes 6 – 10 nm and
357 10 – 15 nm were uniformly set to one third of the respective concentration N_{6-10} and N_{10-15} . The
358 difference between the total number concentrations N_{15} (COPAS) and N_{65} (UHSAS-A) yields the
359 number concentration of N_{15-65} . The number concentration N_{15-65} ($\sim 5000 \text{ cm}^{-3}$) was interpolated
360 over 13 sub-bins (with exponential degradation on increasing particles size) such that the size
361 distribution exhibits a continuous transition towards the detection size range of the UHSAS-A.
362 The size-segregated aerosol concentrations measured with the UHSAS-A were interpolated

363 (with respect to particle size) to the resolution of the remaining 21 sub-bins of the coagulation
364 simulation. The particle concentrations $N(d_p)$ over the entire particle size range from the
365 nucleation-mode sizes to up to $d_p = 1 \mu\text{m}$ were converted into an aerosol size distribution
366 $dN/d \log d_p$ in cm^{-3} as a representation of an initial state and input for the coagulation
367 simulation (for more details see the results in Section 4.5).

368 It is worth noting, that for the coagulation simulation, the NPF event is considered as expired, i.e.
369 any fresh supply of nucleation-mode particles due to continuous or renascent NPF is excluded
370 for the simulated runtime of the coagulation process over 24 hours. Generally, constant
371 conditions of atmospheric pressure (p) and temperature (T) are assumed over the 24-hours
372 period for the simulation, as the air is lifted very slowly at TTL levels within the AMA (by $\sim 1 \text{ K}$
373 potential temperature per day, cf. Vogel et al. (2019), corresponding to $\Delta p \approx 1\text{-}1.5 \text{ hPa}$ and
374 $\Delta T < 1 \text{ K}$ per day).

375 **3.3 Analyses of trajectories and the air mass transport history**

376 Fifty – days backward trajectories were calculated for each sampling position along *Geophysica's*
377 flight track in 1 Hz resolution during the StratoClim 2017 mission using the trajectory module of
378 the Chemical Lagrangian Model of the Stratosphere (CLaMS; McKenna et al. (2002), Konopka et
379 al. (2012), Pommrich et al. (2014)) driven by horizontal winds from ERA-5 reanalysis (Hersbach
380 and Dee (2016)). With the vertical resolution of the ERA-5 data a much better representation of
381 convective updraught and tropical cyclones is realised (Hoffmann et al. (2019)) compared to
382 earlier re-analyses (Dee et al. (2011)), in particular, in the region of the Asian summer monsoon
383 (Li et al. (2020)). Further detailed validation of the very new ERA-5 products is required, so ERA
384 interim re-analyses still represent the state of the art until ERA-5 becomes the new standard.

385 For vertical air mass transport velocities, the diabatic approach was applied using the total
386 diabatic heating rate to extract the vertical velocity, thereby including the release of latent heat
387 (for details, see Ploeger et al. (2021)).

388 The CLaMS backward trajectory calculations, which were initialised from each sampling position
389 along the flight track in 1 Hz resolution, were used to allocate the air's latest contact with the
390 model boundary layer at 2 – 3 km above the ground. This allows for investigating the location of
391 the sources influencing the mixing ratios in the air samples taken aboard the M-55 *Geophysica*.

392 **3.4 The age of air since release from convective outflow**

393 The history of a convective air mass is analysed by making use of the TRACZILLA Lagrangian
394 model (Pisso and Legras, 2008), which is a variation of FLEXPART (Stohl et al., 2005). The
395 simulations were based on the release of a cluster of 1000 back-trajectories, representative of a
396 generic aerosol tracer, each launched from a one-second resolved time step along the flight path.
397 The trajectories were traced back over a period of 30 days in the geographical domain (between
398 10°W and 160°E and between equator and 50°N, respectively). The meteorological fields
399 (horizontal winds and radiative heating rates) are taken from ERA-5 reanalyses. The convective
400 influence is then distinguished from uninfluenced cases by high-frequency images (one image
401 per 10 – 15 minutes) of cloud top altitudes from the geostationary satellites MSG1 and Himawari
402 (for details see Bucci et al. (2020)).

403 Investigations by Weigelt et al. (2009) previously approached the influence of convective cloud
404 processes on the number concentrations of aerosols and in particular of nucleation-mode
405 particles in the upper troposphere. In present study, the convective sources were identified as
406 such if the course of a TRACZILLA-modelled trajectory within a certain geographical area is
407 found below the cloud top level, as similarly done by Tzella and Legras (2011) and Tissier and
408 Legras (2016). It is noteworthy that, while the adopted trajectory method bypasses the
409 uncertainties related to the convective representation in the reanalysis by using observation-
410 based information on the convective events, uncertainties still remain. Those arise mainly from
411 uncertainties in the identification of the cloud top from image data of geostationary satellites,
412 the impossibility to account for the entrainment – detrainment – processes, and reanalysis-
413 related uncertainties concerning advection (for more details see Bucci et al. (2020)). In the
414 presented analysis, the air mass age is computed as the difference between the time of release of
415 the cluster and the convective cloud crossing. Since the trajectory cluster can spread in space
416 and bring different contributions from different regions, only the mean age from the dominant
417 convective source (i.e. the mean age from the regions with the highest percentage of convective
418 clouds crossings) is considered in this analysis.

419 **4 Observations and results**

420 Figure 1 shows the flight tracks of the eight mission flights conducted during StratoClim 2017.
421 The vertical indices (visible in Panel b) highlight the flight sections where significantly increased
422 mixing ratios of nucleation-mode particles n_{nm} were encountered, which are attributable to NPF.
423 NPF of varying intensity occurred near or above the southern flank of the Himalayan (features
424 over Nepal and towards Northeast India) and in a distance of more than 500 km away from the
425 mountains (near the coastline of Bangladesh or the Northeast Indian coast towards the Sea of
426 Bengal). Of the entire COPAS measurement time (~ 22.5 hours) at altitudes above 10 km
427 (≥ 350 K potential temperature) about one third (i.e. ~ 9 hours) of the air samples were taken
428 north of 26° N, i.e. mainly in the immediate vicinity of the Himalayan Mountains, over Nepal and
429 neighbouring areas of northeast India. Hence, over the period of the StratoClim field mission
430 during the 2017 monsoon season, the main transport of NPF precursor material into the UT/LS
431 was by convection above the foothills of the Himalayas. The present study aims at a classification
432 of encountered NPF events with regard to:

- 433 1. the height intervals and geographical positions of NPF observations,
- 434 2. the time limits (event duration and day time of occurrence),
- 435 3. spatial dependencies with regard to tropopause height and AMA geometry,
- 436 4. the relationship between NPF and the air's origin and age.

437 It is noteworthy that, during StratoClim 2017, NPF was frequently observed in the presence of
438 ice cloud particles at the bottom TTL of the AMA. The conditions under which in-cloud NPF
439 occurred during StratoClim are discussed in Weigel et al. (2021b). Since the NPF turned out to
440 be almost undisturbed by the presence of cloud elements (until a certain number density and
441 size of the ice particles are reached), for the present study the NPF encounters remain
442 undifferentiated concerning clear-air or in-cloud conditions.

443 **4.1 Vertical distribution of particle number concentrations with respect to** 444 **observations in different tropical regions**

445 Vertical profiles of the total particle number concentration obtained from various field
446 campaigns in the tropics are shown as median with percentiles in Figure 2. The vertical CN
447 profiles from tropical regions of South America and West Africa (TROCCINOX, 2005 and SCOUT-

448 AMMA, 2006, Figure 2, Panels a and b) exhibit merged data of two independent CN-detectors
449 with individual d_{p50} (i.e. N_6 for $\theta > 350$ K and N_4 for $\theta < 350$ K), which were deployed on
450 individual aircraft, the M-55 *Geophysica* and the DLR Falcon-20 (cf. Borrmann et al. (2010) and
451 Weigel et al. (2011)). The dark shaded areas of the vertical profiles illustrate the scatter of
452 number concentrations between the 90th and 99th percentiles. At tropopause altitudes around
453 380 K (indicated by vertical bars), or rather at the bottom TTL, the variability of detected
454 concentration reaches a maximum between 90th and 99th percentile. The increased data scatter
455 indicates the influence of NPF on the class of sub-micrometre sized particles at these TTL levels,
456 resulting in increased and fluctuating particle number concentrations due to the variable
457 production rate of particles by NPF (cf. Section 0). Exclusively above the tropopause within the
458 AMA (Figure 2 c), the scatter of the concentration values of sub-micrometre sized particles
459 remains elevated up to heights of ~ 400 K potential temperature. Up to this point within the
460 AMA, the scatter of the peak number concentrations (90th to 99th percentile range) is
461 significantly increased in reference to the median values, while in other regions above the
462 tropopause (Figure 2 a and b) the profiles of aerosol concentrations show a smoother transition
463 into the stratosphere.

464 For comparison, in Panel d of Figure 2, particle number concentrations $N_{5.3}$ are compiled as a
465 vertical median profile (with percentiles) obtained from airborne measurements with the Nuclei
466 Mode Aerosol Spectrometer (NMASS; Brock et al. (2000)) during several years (2004 – 2007,
467 including winter and summer season) over Central America. These observations differentiate
468 the bottom TTL (here 350 – 379 K) as the region where NPF predominantly occurs with the
469 largest impact on the fine-mode (sub-micrometre sized) aerosol particle concentration (e.g.
470 Borrmann et al. (2010) or Weigel et al. (2011)). However, this vertical profile (Figure 2 d)
471 illustrates additional features at altitudes above the mean tropopause altitude (assumedly
472 located at ~ 380 K). The locally increased concentrations with respect to the median become
473 apparent at $\sim 380 - 390$ K and at $\sim 400 - 410$ K, respectively. Above tropopause levels,
474 significantly increased number concentrations of fine-mode particles, potentially caused by local
475 NPF, were observed over both, Central America (Figure 2 d) and the Indian subcontinent within
476 the AMA (Figure 2 c).

477 **4.2 Mixing ratio of submicron particles, abundance and fraction of refractory particles**
478 **from StratoClim 2017 observations**

479 The entire StratoClim 2017 data set of measured (1 Hz-resolved) particle mixing ratios n_6 and
480 n_{10} is summarized in Figure 3 a as function of potential temperature. The resulting median
481 profile n_6 of the StratoClim 2017 measurements is shown with 25th and 75th percentile (blue
482 profile). This allows for a direct comparison with the corresponding median profiles from earlier
483 COPAS measurements at tropical regions (in red: TROCCINOX, Brazil, 2005 and in dark green:
484 SCOUT-AMMA, West Africa, 2006, cf. Borrmann et al. (2010) and Weigel et al. (2011)). Figure 3 a
485 includes also the median vertical profile of the mixing ratios of fine-mode particles (bright green
486 line), which was obtained from measurements over Central Pacific, at tropical latitudes (Brock et
487 al., 1995).

488 The profiles (n_6 , n_{10} , and n_{nm} in Figure 3 a and b) are structured as:

- 489 1) $\sim 350 - 380$ K: characterised by the largest scatter of the particle mixing ratios and the
490 highest values of up to $5 \cdot 10^4 \text{ mg}^{-1}$, thus, representing the height level of the profile's
491 maximum.
- 492 2) $\sim 380 - 415$ K: the scatter of the particle mixing ratios is still increased though less
493 prominent.
- 494 3) Above ~ 415 K: characterised by a comparatively weak but extant scatter level of
495 particle mixing ratios, which also includes features of the median n_6 profile at $410 -$
496 415 K within the AMA.

497 The course of the median profiles exhibits similar characteristics. The common feature of all
498 median profiles from the tropics is their maximum at about $350 - 360$ K, while the AMA
499 observations indicate a corresponding maximum at slightly higher altitudes (i.e. $355 - 365$ K).
500 Further aloft, the particle mixing ratios obtained from different locations decrease with altitude
501 on similar gradient. In the altitude range between 360 K and 400 K, the tropical data obtained
502 over South America (red) constitute the lowest particle mixing ratios (by median values),
503 whereas all other profiles are almost in line with each other up to 400 K. The vertical median
504 profile of particle mixing ratios determined in the AMA (blue) during StratoClim 2017 exhibit
505 the highest mixing ratios at each height level up to ~ 415 K. Additionally, the AMA profile
506 features a substantial increase of the median mixing ratio at altitudes of $\sim 410 - 415$ K, where

507 the values exceed those from the tropical regions by about 35 %. Above 415 K, the continuation
508 of the tropical profiles from West Africa and Central America (coloured green) with altitude is
509 largely consistent with the particle mixing ratios measured throughout StratoClim 2017, while at
510 these altitudes the measurements from South America (red) show comparatively increased
511 values. Above 440 K, the particle mixing ratio over West Africa (dark green) significantly
512 deviates from those of all other vertical profiles, as visible from the gradual increase of the
513 particle mixing ratio with altitude. This deviation was attributed to the influence of the high-
514 reaching volcanic injections of Soufriere Hills (Borrmann et al., 2010). The 1 Hz-resolved
515 StratoClim 2017 data (grey dots in Figure 3 a) are added to the graph to illustrate how the
516 scatter of measured particle mixing ratios relates to corresponding median profiles.

517 Figure 3 b shows the vertical distribution of the mixing ratio of the nucleation-mode particles
518 n_{nm} (cf. Subsection 0). The flight-by-flight colouration of the data points indicates that increased
519 n_{nm} values were observed during each of the eight StratoClim 2017 mission flights. In addition,
520 Figure 3 b shows the wide range of altitudes over which the layers of increased n_{nm} were
521 observed during the individual flights. Remarkably increased values of n_{nm} were detected up to
522 altitudes as high as 400K.

523 Figure 3 c depicts the 1 Hz-resolved mixing ratios of the non-volatile particles n_{10nv} (cf.
524 Appendix A) as also the resulting median profile of n_{10nv} with 25th and 75th percentiles. Figure
525 3 c additionally shows the median profile of n_6 as in Figure 3 a, which illustrates the vertical
526 progression of n_{10nv} in direct relationship to the NPF-influenced total particle mixing ratio.
527 Figure 3 d illustrates the vertical distribution of the fraction f of non-volatile particles, i.e. the
528 ratio $\frac{n_{10nv}}{n_{10}}$ (cf. Subsection 2.1.2), which is presented in 1 Hz-resolution as also the profiles of
529 resulting median with 25th and 75th percentiles. At lower altitudes (< 350 K), the mixing ratio of
530 non-volatile particles appears low with a relatively large scatter. The local minima of the n_{10nv}
531 profile and of the fraction f coincide with the local maximum of n_6 (i.e. ~ 355 - 375 K). Above
532 370 K, the n_{10nv} profile follows the general decline with height. Above 390 K, both mixing ratios
533 (n_6 and n_{10nv}) decrease uniformly and the fraction f remains almost constant at ~ 45 – 50 % up
534 to altitudes of 430 K. Towards 435 K, the total mixing ratio n_6 nearly stagnates whereas n_{10nv}
535 exhibits slightly dropping mixing ratios.

536 In essence, the vertical profiles of the total particle mixing ratio n_6 and those of the non-volatile
537 particles n_{10nv} are divided into three ranges:

538 A) At the bottom TTL region ($\theta < 375$ K), both n_6 and n_{10nv} are mainly characterised by NPF
539 as indicated by the high mixing ratios of nucleation-mode particles n_{nm} . NPF causes a
540 significant addition to the scatter of the total mixing ratios towards high values, which
541 exceed the median by more than one order of magnitude. In this altitude range, a local
542 deficit of the non-volatile particle compounds favours the occurrence of NPF.

543 B) Further above, i.e. ~ 375 K $< \theta < 415$ K, continued albeit attenuated NPF is identified at
544 tropopause levels within the AMA. The non-volatile particle compounds (n_{10nv}) slightly
545 decrease compared to levels below 375 K. The fraction f however rises towards 40 %.
546 Nevertheless, n_{nm} of 400 - 2000 mg^{-1} at heights of up to ~ 400 K indicate sustainably
547 effective NPF.

548 C) Above 415 K, the values of the total mixing ratio n_6 approach previous observations (e.g.
549 Brock et al. (1995)). The scatter of n_6 and n_{10nv} is considerably decreased at these
550 altitudes. NPF appears to have entirely abated, since at these heights sufficiently high n_{nm}
551 were not observed at all. The median proportion f of non-volatile particles remains at
552 $\sim 40 - 50$ % up to the highest altitude.

553 The steeply dropping vertical profile of the total mixing ratio of the sub-micrometre sized
554 aerosols above ~ 415 K subtly indicates the upper limit of the AMA's influence on the vertical
555 mixing of the UT/LS. From the CO, ozone, and nitrous oxide content in air samples taken
556 throughout StratoClim 2017, von Hobe et al. (2020) concluded that the AMA's interior was
557 largely isolated from stratospheric in-mixing up to altitudes of 10 to 20 K above the tropopause
558 (i.e. $\theta \approx 400$ K). Moreover, they found that mixing processes with stratospheric air are of
559 increasing significance at levels between 400 K and 420 K (*ibid.*). At altitudes above $\theta \approx 440$ K,
560 the median mixing ratios n_6 exhibit a vertically stable continuation after another sharp drop
561 between 435 K and 440 K (Figure 3 a and b). Brunamonti et al. (2018) specified the 440 K level
562 as the top of confinement (TOC) of the AMA for the 2017 monsoon season. So, according to this
563 TOC definition, above 440 K potential temperature ($\gtrsim 18.5 - 19$ km), the median n_6 (Figure 3 a
564 and b) represents stratospheric background values.

565 The ATAL (Vernier et al. (2011a), and see also Höpfner et al. (2019); Mahnke et al. (2021)) is
566 mainly attributed to the uplift of pollution from the boundary layer as concluded from balloon-
567 borne and satellite-based observations (Vernier et al., 2018). The described drop in the aerosol
568 concentration (*ibid.*) at potential temperatures of $\sim 400\text{-}420\text{ K}$ (well above tropopause levels)
569 coincides with the uppermost altitude limit of main NPF activity at $\sim 400\text{ K}$ ($\sim 17.5\text{ km}$)
570 observed during StratoClim 2017 (cf. Figure 3). Here, the most substantial decrease of both
571 mixing ratios n_6 and $n_{10\text{NV}}$ was observed on transit from $\sim 410\text{ K}$ to $\sim 415\text{ K}$ (at $\sim 18\text{ km}$).

572 **4.3 Occurrence frequency of NPF events**

573 Figure 4 shows the 130 individual NPF events sorted according to their duration. Based on the
574 average flight speed (Section 0), and assuming a constant heading during flight, the mean
575 horizontal distance per 10 seconds flight time ranges at about 1.5 km. The spatially most
576 extended uninterrupted NPF signature throughout StratoClim 2017 spanned a mean horizontal
577 distance of $\sim 110\text{ km}$. The hitherto most extended NPF event observed with COPAS at TTL level
578 over South America (Weigel et al. (2011)) lasted over a continuous duration of 262 seconds
579 ($\sim 35.5\text{ km}$ of covered flight distance). Another three individual NPF events were observed
580 above West Africa (*ibid.*) over 20, 83, and 98 seconds ($\sim 3\text{ km}$, $\sim 12\text{ km}$, and $\sim 13\text{ km}$)
581 respectively. Approximately 45 % of 130 NPF events observed throughout StratoClim 2017
582 were of less than 20 seconds duration ($\sim 3\text{ km}$), while the majority ($\sim 75\%$) of NPF
583 observations above the Indian subcontinent extended over less than 80 seconds ($\sim 12\text{ km}$,
584 Figure 4 a. The vertical profile (Figure 4 b) show that above 380 K predominantly short events of
585 less than two minutes duration with comparatively low mixing ratios n_{nm} were encountered.
586 Here, observed NPF events rarely lasted for several minutes (i.e. 5-6 minutes). In the lower TTL
587 range, i.e. below the tropopause, the number of persistent NPF events was higher than above the
588 tropopause, and the mixing ratio of nucleation-mode particles was also more often increased.
589 The highest mixing ratios of nucleation mode particles were measured in events lasting from
590 one to a few (up to about seven) minutes.

591 Figure 5 depicts the diurnal distribution of observed NPF events. The frequency of NPF event
592 observations is analysed as a function of the local daytime (LT) at Kathmandu, Nepal (Figure
593 5 a). Apart from one exception, the occurrence frequency of the NPF events seems evenly
594 distributed over the course of a day. The exception is a time window between 10:00 and 10:30

595 a.m. (LT) when recent particle formation was observed up to 2.5 times more often than at other
596 times of the day. In this time window, about one third of all NPF events (31 of 105 events with
597 durations of more than 5 seconds) was observed, most of which (25 of 31 events) lasted for less
598 than 80 seconds (< 12 km mean horizontal distance). The measurements in this time window
599 occurred at two distinct altitude layers, ~ 360 - 370K and ~ 390 - 400 K. The majority of the
600 StratoClim NPF events in this period (20 of 31 events) were from altitudes above 390 K while
601 ascertained mixing ratios $\overline{n_{nm}}$ never ranged outside ~ 500 - 5000 mg⁻¹ during this day time.
602 Throughout the StratoClim 2017 mission, no further NPF event was observed above 390 K at
603 any earlier day time and only two single events were encountered at these heights during
604 different flights at a later day time (~ 12:20 and ~ 17:30 LT, respectively). Whether this
605 pronounced frequency of NPF occurrence at a particular time of day is due to bias effects would
606 require a larger database. Beyond this, preferred day times when NPF was observed with
607 particular frequency were not identified in the StratoClim observations, while instead, within
608 the same region, a diurnal dependence of NPF was previously concluded based on a larger data
609 set (Hermann et al., 2003). The diurnal dependence of NPF would be expected if H₂SO₄ is
610 assumed to be the main nucleating compound whose production maximum (from the reaction
611 SO₂ + OH) at the local noon time correlates with the solar zenith (cf. Weigel et al. (2011)).

612 Throughout StratoClim 2017, NPF was predominantly observed before local noontime during
613 the mission flights KTM 2, KTM 3, KTM 5 and KTM 7, while all other observations were made
614 mainly during the afternoon. All NPF events, which lasted longer than five seconds, were almost
615 evenly distributed over the day. Furthermore, Figure 5 c indicates that the longest NPF events
616 are not generally associated with highest mean mixing ratios $\overline{n_{nm}}$. The duration of an event is
617 therefore primarily an indicator of the spatial extent of a region where NPF takes place. The
618 derivation of the spatial extent from the duration of individual events, however, bears significant
619 uncertainties, since changes in flight attitude, such as curve manoeuvres or changing flight levels
620 during an event, are not taken into account.

621 The NPF events observed during StratoClim 2017 are among the most frequent and spatially
622 most extended of all those, which have been identified by means of COPAS measurements during
623 previous missions (cf. Borrmann et al. (2010); Weigel et al. (2011)). Only a few events were
624 observed during StratoClim 2017, which lasted more than 100 seconds, but it cannot be

625 excluded that they were actually composed of individual events of smaller extent. Very short
626 events (< 10 s) make up almost 40 % of all NPF events observed. Consequently, hereafter, all
627 events shorter than five seconds (i.e. 25 out of 130 events) are discarded from further analyses.
628 In this way, individual 1-2 second features are filtered from the data. In addition, for the
629 evaluation of individual NPF events, the reliability of the results increases if the arithmetic
630 averaging occurs over more than five data points. Finally, the accuracy of the specified event
631 duration improves as the raw signal processing (Subsection 2.1.3) smooths the temporal
632 salience of short events.

633 **4.4 The occurrence of NPF relative to the tropopause height and the AMA's centre**

634 Figure 6 illustrates the mean mixing ratio of nucleation mode particles $\overline{n_{nm}}$ measured during the
635 individual NPF events as a function of (1) the vertical distance $\overline{\Delta\theta}$ to the lapse rate tropopause
636 (Figure 6, Panels a and c) and (2) the mean equivalent latitude $\overline{\phi_{equ}}$ (Figure 6, Panels b, and d).
637 NPF events above the lapse-rate tropopause (Figure 6 a, positive $\overline{\Delta\theta}$ and up to + 30 K) were
638 mainly observed during the first half of the StratoClim 2017 mission (KTM 2, KTM 3, and KTM 5;
639 on 29 July, 31 July, and on 04 August 2017, respectively, with maximum ceiling > 475 K) or
640 during the last mission flight (KTM 8, on 10 August 2017, maximum ceiling ~ 435 K). All further
641 observations up to $\theta > 425$ K were located below the lapse-rate tropopause (negative $\overline{\Delta\theta}$, down
642 to - 35 K) or in its close vicinity ($\overline{\Delta\theta} \approx 0$ K, e.g. KTM 6, 06 August 2017, maximum ceiling
643 ~ 380 K), i.e. in or above the region of the main convective outflow. **As indicated by Stroh and**
644 **the StratoClim group (2021),** the first half of the StratoClim 2017 mission was characterised by
645 weak convection, while the convective activity increased as the campaign progressed.

646 With respect to the AMA centre, most NPF events were encountered north of 60° equivalent
647 latitude (Figure 6 b). An exception is a flight segment of flight KTM 3 (on 31 July 2017), where
648 weak NPF with mixing ratios $\overline{n_{nm}}$ of $\sim 500 - 1300$ mg^{-1} were detected at the farthest distance
649 from the AMA centre (near the turning point at about 21.5° N and 80° E geographic coordinates,
650 see Figure 1). These measurements (at $\overline{\phi_{equ}} < 60^\circ$ N) were made well above the tropopause since
651 at positive $\overline{\Delta\theta}$ (up to + 10 K) mean CO mixing ratios of $45 - 50$ nmol mol^{-1} (Figure 6, Panels c and
652 d) in agreement with satellite-based CO observations for altitudes of $\sim 16-19$ km within the
653 AMA (Park et al., 2009).

654 Towards the AMA centre ($\overline{\phi_{\text{equ}}} > 60^\circ\text{N}$), the NPF events are distributed over the entire range of
655 $\overline{\Delta\theta}$. Here, weak NPF with several hundreds of nucleation-mode particles per milligram were
656 observed well above the lapse-rate tropopause ($\overline{\Delta\theta} \approx +28\text{ K}$). The vertical distribution of the
657 NPF events indicates that those events with the highest $\overline{n_{\text{nm}}}$ and mainly elevated CO mixing
658 ratios (65 nmol mol⁻¹ to ~ 137 nmol mol⁻¹) were encountered exclusively below the lapse-rate
659 tropopause (to minimum $\overline{\Delta\theta}$ of -35 K). Regarding a relationship between (a) the relative
660 position to the AMA centre and (b) the effectiveness of vertical transport or the NPF rate, the
661 StratoClim 2017 data show: between 60°N and 90°N equivalent latitude, there is no indication
662 that the mixing ratios of $\overline{n_{\text{nm}}}$ and CO depend on the position with respect to the AMA centre.
663 Close to the AMA centre (60°N - 90° N) and in an altitude range of almost $\pm 30\text{ K}$ around
664 tropopause heights, both the distribution of CO-enriched air masses and the occurrence of NPF
665 appear as largely independent from $\overline{\phi_{\text{equ}}}$.

666 **4.5 Persistence of particles in the nucleation mode**

667 Coagulation represents one of the main processes limiting the persistence of nucleation mode
668 particles, i.e. the duration during which freshly formed particles remain in the size range of the
669 nucleation mode. At elevated number densities, the highly diffusive nucleation-mode particles
670 collide and coagulate with each other and with the present background aerosols on short time
671 scales. Gaseous precursors, which are saturated or supersaturated under NPF conditions, may
672 condense and additionally contribute to the growth of particles out of the nucleation-mode size
673 range, which is considered as a secondary process.

674 The aerosol size distribution, which was compiled from the measurements during a NPF event
675 as input for the coagulation simulation (cf. Section 3.2), is depicted in Figure 7 (black circles with
676 horizontal bars indicating the width of their respective particle size bins of the model). The
677 simulated change of the initial aerosol size distribution due to coagulation is shown in one-hour
678 steps in different colours and line types (Figure 7 a). From this simulation, the temporal decay of
679 N_{nm} was derived (Figure 7 b, solid black line), whereby the gradient of this decay illustrates the
680 coagulation rate. The sequence of the simulated size distributions indicates that the initial
681 amount of nucleation-mode particles is reduced by coagulation within a few hours. Within the
682 first hour after an expired NPF event the nucleation mode is no longer predominant in the
683 overall size distribution, as seen from the maximum of the distribution at $d_p > 15\text{ nm}$ after one

684 hour of simulated coagulation (solid red line in Figure 7 a). Hence, with adopted instruments for
685 the detection of nucleation mode particles, a clear NPF signature is identified only while NPF is
686 just proceeding or for a very short time immediately after an expired NPF event.

687 The concentration of nucleation-mode particles N_{nm} decreases steeply over time (Figure 7 b).
688 From initially $\sim 13000 \text{ cm}^{-3}$ of nucleation-mode particles ($\sim 75\%$ of N_{total}) at the earliest stage,
689 N_{nm} falls below 1000 cm^{-3} ($\sim 20\%$ of N_{total}) within about 1 hour (the grey shaded areas serve for
690 reference). The detection of 1000 cm^{-3} of nucleation-mode particles, however, would be
691 interpreted as a NPF event of intermediate strength (cf. Section 0). In addition, coagulation leads
692 to N_{nm} below 100 cm^{-3} ($< 5\%$ of N_{total}) during less than four hours and to N_{nm} of less than 10 cm^{-3}
693 within nine hours. The efficiently proceeding coagulation impedes the identification of NPF
694 based on *in-situ* detections and it is required to be at the NPF site at the right time. This
695 circumstance is corroborated by tests concerning the sensitivity of the simulation to varying
696 input parameters. For these tests, the input in the nucleation mode was modified while keeping
697 constant background aerosol conditions. In three further simulation runs, the initial N_{nm} was
698 multiplied by the factors 0.1, 10 and 100, respectively ($N_{nm,0.1}$, $N_{nm,10}$, $N_{nm,100}$, dashed lines in
699 Figure 7 b). Increased initial concentrations of nucleation-mode particles, $N_{nm,10}$ and $N_{nm,100}$, last
700 only for about 15 minutes compared to the original N_{nm} (black line in Figure 7 b). The initial
701 values $\sim 10^5$ or $\sim 10^6 \text{ cm}^{-3}$ drop very quickly due to elevated coagulation rates, and in both of
702 these cases, $N_{nm,10}$ and $N_{nm,100}$ fall below 1000 cm^{-3} within less than one hour. The threshold of
703 100 cm^{-3} is crossed after less than 2 hours ($N_{nm,10}$) or after 30 minutes ($N_{nm,100}$). Therefore, NPF
704 events, which produce much higher concentrations of nucleation-mode particles, require even
705 shorter time periods for a successful detection (e.g. by COPAS) after their expiration. However,
706 for the simulation of decreased concentrations ($N_{nm,0.1}$), the coagulation rates remain nearly
707 constant, as indicated from the almost identical decays of $N_{nm,0.1}$ and N_{nm} (Figure 7 b). Simulated
708 concentration of nucleation-mode particles fall below 100 cm^{-3} within almost the same time
709 from the initial values $N_{nm,0.1}$ or $N_{nm,10}$, respectively. Further investigations on the sensitivity of
710 the simulation to the assumed pressure and temperature conditions as simulation input did not
711 reveal any significant dependence, unless the input is varied by more than $\pm 10 \text{ hPa}$ and $\pm 18 \text{ K}$
712 from used values of respective parameter (not shown herein).

713 Based on these estimations, the detection of elevated N_{nm} indicates that an event with high NPF-
714 rates is currently proceeding, or a recently expired NPF event was observed. Detections of lower
715 values of N_{nm} could indicate a) intermediate or weak (currently proceeding) NPF at low
716 supersaturation of the NPF precursor or b) a NPF event (e.g. of high particle productivity) that
717 has phased-out several hours before the observation. NPF is measured *in-situ* while the
718 formation event is currently in progress or at most a few hours later. Therefore, the short
719 periods of time available for a clear NPF detection and the yet frequent NPF encounters on each
720 measurement flight during StratoClim 2017 indicate the prevalence of such events within the
721 AMA.

722 5 NPF's connection to ground sources and vertical transport

723 5.1 NPF in relationship to CO as pollution indicator

724 NPF events with moderate numbers of nucleation-mode particles ($< 1000 \text{ cm}^{-3}$) in the lower TTL
725 region were previously attributed to CO mixing ratios above $\sim 70 \text{ nmol mol}^{-1}$ (60 - 70 nmol mol^{-1}
726 were assumed as a typical CO background in the pristine marine boundary layer, cf. Weigel et al.
727 (2011)). Elevated amounts of nucleation-mode particles (of up to $\sim 6000 \text{ cm}^{-3}$) at altitudes of
728 $350 \text{ K} < \theta < 360 \text{ K}$ were associated with significantly increased CO mixing ratios of more than
729 85 nmol mol^{-1} (*ibid.*). These results, mainly based on two single NPF events over West Africa
730 (SCOUT AMMA 2008), could have indicated a correlation between NPF rates and CO- load from
731 pollution. However, almost a hundred of individual event observations (Section 4.4 and Figure 6,
732 Panels c and d) indicate, that the relationship between pollution level and NPF-rates is less
733 direct than expected. In Figure 8, the 1 Hz-resolved data of synchronous detections of CO and
734 particle mixing ratio during the entire StratoClim 2017 mission are compared. To illustrate the
735 relative scattering of both n_6 and n_{nm} , the total particle mixing ratio n_6 is shown in the
736 background (grey dots) and the mixing ratio of particles in nucleation mode n_{nm} , (dots coloured
737 with respect to θ) is displayed in the foreground.

738 At altitudes below the tropopause (below $\sim 380 \text{ K}$), where NPF-rates lead to highest n_{nm} , the
739 relationship between the 1 Hz-resolved n_6 or n_{nm} and the CO mixing ratio is highly variable. At
740 CO levels of $80 - 100 \text{ nmol mol}^{-1}$, the scatter of n_{nm} ranges from 700 mg^{-1} to the absolute
741 maximum of about 50000 mg^{-1} . This maximum n_{nm} is exclusively reached at CO mixing ratios of
742 $100 \pm 2.5 \text{ nmol mol}^{-1}$. At the maximum CO mixing ratio (i.e. $\sim 150 \text{ nmol mol}^{-1}$), particle mixing

743 ratios n_{nm} of about 6000 mg⁻¹ (median value) were detected. Within a range of CO content
744 between 85 and 130 nmol mol⁻¹, the n_{nm} (median) mixing ratios ranged consistently between
745 2000 and 10000 mg⁻¹, apart from the notable exception at about 100 nmol mol⁻¹. CO mixing
746 ratios between 60 nmol mol⁻¹ and 80 nmol mol⁻¹ were detected just below or at tropopause
747 levels (yellow to orange colours) coincidentally with decreasing n_{nm} from about 3000 mg⁻¹ to
748 values below 1000 mg⁻¹. For CO mixing ratios below 60 nmol mol⁻¹, n_{nm} almost stagnates
749 between 300 and 1300 mg⁻¹. At tropopause levels and aloft, the decreasing CO mixing ratio as
750 well as abating NPF (expressed in decreasing n_{nm} values) likely result from both the degradation
751 of CO (cf. von Hobe et al. (2020)) and the lacking supply of NPF precursor material by direct
752 transport. According to von Hobe et al. (2020) any indication is missing that convection
753 penetrated the tropopause during the StratoClim 2017 period. However, Lee et al. (2019)
754 investigated the TTL-hydrating influence of an overshooting event that occurred in the Sichuan
755 Basin about 1.5 days before the StratoClim measurements southbound of Kathmandu over
756 northeast India (M-55 *Geophysica*, KTM 7 on 8 August, 2017). Hence, there is no clear indication
757 for a direct relationship between CO enriched (polluted) air and the NPF rate.

758 **5.2 NPF and air mass origin in the boundary layer**

759 The assignment of certain measurement sections of elevated n_{nm} to possible source regions of
760 NPF precursors is carried out in two steps:

761 (1) The backward trajectories were traced down to the boundary layer (BL) for each
762 measurement point (cf. Section 3.3) at which NPF was detected (Figure 9 a and b). In this way,
763 the geographical position of the last BL contact of the air before the observations (1 Hz
764 resolution) of elevated n_{nm} (≥ 300 mg⁻¹) is obtained throughout the StratoClim 2017 mission
765 (Panel a). In addition, the geographical position of the trajectories' fastest uplift during their
766 transport history was determined (Panel b).

767 (2) The ERA-5 reanalysis data were examined with regard to the transport time of the
768 trajectories between the position in the BL and the coordinates of the measurement point
769 (Figure 10 a and b). The transport time is then coupled with the geographical position of the last
770 BL contact of the air before the NPF observations (Panel a) and the position of the trajectories'
771 fastest uplift in their transport history (Panel b).

772 According to the distribution of the trajectories' latest BL contact with reference to the n_{nm}
773 mixing ratio (Figure 9 a), hardly any systematic structure is visible (the close-up views in Panels
774 a.1 and a.2 provide a new scaling and arrangement of the points of identical data set). The
775 possible source regions are distributed over the entire region almost independently of the NPF
776 intensity. The last BL contact of some trajectories was at locations far away from the monsoon
777 region (e.g. in the West: the east coast of Africa and the Gulf of Aden; in the East: Indochina, the
778 South China Sea and as far as the Philippine Sea). The entire possible source area of NPF
779 precursors ranges from the north of India and the Arabian Sea, Pakistan, Afghanistan, Southwest
780 China, Taiwan, the Philippines, and the Bay of Bengal.

781 Locations of fastest vertical updraught are more compactly distributed (Figure 9 b, close-up
782 views in Panels b.1 and b.2) and better reflect the contours of an area where efficient convection
783 frequently occurs within the monsoon region. Fastest updraught with simultaneously increased
784 n_{nm} is found in the Kathiawar region on the Indian west coast towards the Arabian Sea, or in the
785 far north of India (in the areas around Ladakh, Himachal Pradesh, and eastern Punjab). In areas
786 of the central Tibetan Plateau, some sites were identified with elevated n_{nm} , where also the
787 fastest vertical upward transport occurred. Finally, the shape of the Himalayan Mountains is
788 traced by the locations with the fastest vertical air mass transport over a wide range of n_{nm} .

789 Also the shortest transport times from the BL are found around the Himalayan mountains and
790 their foothills. Whereas the transport times from locations of air's last BL contact, which fall
791 south of 25°N, west of 72°W, or east of 96°W, are rarely shorter than 10 days. In Figure 10 (a and
792 b, cf. also respective close-up view), the contour of the Himalayan mountain chain is clearly
793 reproduced by the distribution of the data points (transport times of less than ~ 5 days and
794 fastest vertical updraught). Hence, for the duration of the StratoClim 2017 mission, the
795 convective uplift mainly occurred within the AMA. This more compact regional distribution of
796 vertical uplift (Figure 10 b) is possibly related to the occurrence of a *vertical conduit* for upward
797 transport in the monsoon, as conjectured by Bergman et al. (2013). Figure 10 also indicates air
798 masses of elevated n_{nm} , which have experienced convective uplift over Tajikistan and northern
799 Afghanistan as well as over regions around the Yellow Sea, the Korean Peninsula or Japan, hence,
800 far away from the AMA system.

801 Both graphics, Figure 9 and Figure 10, finally show that the region of the air's last BL contact and
802 the location of the fastest vertical uplift do not necessarily coincide. Similarly, the locations of
803 the fastest updraught do not always match the shortest transport times, but for most cases in the
804 immediate vicinity of the Himalayas this correlation is clearly visible from the StratClim 2017
805 data set. Ultimately, it cannot be excluded that, within the free troposphere, the air is subject to
806 loading from various source regions (not exclusively from the location of the last BL contact)
807 prior to its convective uplift. Of course, this finding complicates an unambiguous apportioning of
808 NPF to specific source regions of precursors in the BL.

809 The vertical distribution of the n_{nm} mixing ratios as a function of the air mass transport time
810 from the BL is shown in Figure 11:

811 1) Above 380 K, almost all observations of enhanced n_{nm} are associated with air mass
812 transport times of more than 12 days. At 380 ± 3 K, none of the detected n_{nm} is connected to air
813 mass transport times of less than 12 days. Several times higher n_{nm} (with 10^3 - 10^4 mg^{-1}) were
814 detected below 380 K in air masses, which had experienced more than 25 days of transport time
815 from the BL.

816 2) Below 380 K, the transport times are variably distributed over the altitude range
817 between 350 K and 380 K. The air masses with shortest transport times are located in the height
818 interval between 360 K and 370 K. As shown by a recently published investigation, these air
819 masses have presumably reached the ~ 360 K level (altitude of the main convective outflow)
820 very quickly by an effective convective transport and are then moved further aloft, towards
821 370 K, with much lower ascent rates (Vogel et al., 2019) due to the prevailing air mass uplift
822 within the AMA.

823 3) On occasion, very short transport times were found with maximum n_{nm} at altitudes of
824 about 367 K and 370 K. However, the highest n_{nm} are mostly not observed in air with such short
825 transport times. Within 370 ± 3 K, the detected n_{nm} reach extreme values (~ 50000 mg^{-1}) in air
826 with transport times of up to 15 days. Above 370 K and below 355 K none of the maximum n_{nm} is
827 associated with transport times of less than 6 days, and here, the highest n_{nm} were detected in
828 air with transport times of up to 25 days. Therefore, based on the observations and the
829 trajectories analysed here, the altitude band of the main convective outflow is limited to a range
830 between 355 – 370 K.

831 **5.3 The relationship between NPF and convective outflow**

832 For the following analysis, which is summarised in Figure 12, the vertical distribution of the
833 mean mixing ratios $\overline{n_{nm}}$ of respective NPF event (cf. Sections 0 and 4.4) are juxtaposed with

- 834 a) a measure for the convective contribution to the composition of the probed air mass and
- 835 b) the mean transport time within the TTL since their release from the top of individual
836 convective cells (cf. Section 3.4 for both variables).

837 Figure 12 a broadly confirms the general understanding that the main outflow region of deep
838 convection is well below the tropical tropopause (i.e. at 350 - 370 K) and aloft the air is still
839 rising, but at a much lower vertical velocity. At altitudes above ~ 380 K, the observed NPF events
840 with $\overline{n_{nm}} < 2000$ mg⁻¹ generally remain in the lower range of moderate intensity (cf. Section 0),
841 although there was one of the rare observations of overshooting convection up to levels ~ 385 K
842 where NPF was detected in coincidence with ice cloud elements (cf. Weigel et al. (2021b)).
843 Hence, if in exceptional cases the outflow region of deep convection extends above the 380 K-
844 level, as indicated by the presence of ice cloud elements, then high NPF rates are not necessarily
845 to be expected. Below 380 K, about two thirds of all events are connected to convective influence
846 by more than 75 %. However, a remarkable proportion of observations below 380 K indicates
847 convective contributions of less than 60 % and down to 25 %. Below ~ 375 K, mean mixing
848 ratios $\overline{n_{nm}}$ of 1000-2000 mg⁻¹ were associated with 100 % convective contribution, and mixing
849 ratios of more than 10000 mg⁻¹ were sometimes observed in air masses with ~ 30 % convective
850 contribution.

851 For the observed NPF events, Figure 12 b shows the mean age of the probed air masses since
852 their release from the top of individual convective cells. Above ~ 380 K, the air escaped the
853 convection top mainly 12 days (or more) prior to its probing. Two events at ~ 382 K and at
854 ~ 385 K, respectively, indicate a more recent convective uplift, within 5 days before the air was
855 sampled. Despite the comparatively short transport times, here, the observed $\overline{n_{nm}}$ remained
856 below 2000 mg⁻¹. At altitudes below ~ 380 K, the air predominantly resided within the TTL
857 region for less than 5 days prior to the observation. Nevertheless, some of the comparatively
858 intensive NPF events (with $\overline{n_{nm}} \approx 7000 - 15000$ mg⁻¹ at ~ 360 K - 375 K) were observed in air,
859 which has been released from associated clouds' top more than a week (and up to two weeks)
860 prior to the measurements. It should be considered, however, that short air mass transport

861 times within the TTL are indicated also for NPF events with minor convective contribution
862 (< 50 %).

863 From the StratoClim 2017 data base emerges that NPF occurs at the lower TTL (i.e. below the
864 tropopause) of the AMA in air masses that have been lifted by convection in time intervals
865 ranging from 5 days to about two weeks. However, it remains unclear whether in some of the
866 observed events the air samples were taken at a very advanced stage of NPF. Therefore, it can
867 only be surmised whether or how often the short time period was missed during which NPF is
868 detectable by aircraft-based measurements. Potential uncertainties remain to be considered in
869 connection with the uncertainty of the reanalysis data and the representation of the transport
870 history of the air masses.

871 **6 Potential impact of gravity waves on vapours' supersaturation**

872 If the lifted precursor material would be suitable for NPF and sufficiently enriched right upon
873 release from the convective outflow, the relationship between elevated n_{nm} and convective
874 transport should be clearer than observed (cf. Section 5). The lack of an unambiguous
875 relationship indicates that the recently transported material is deposited in the TTL but not
876 immediately consumed, e.g., by NPF although the presence of ammonium in the aerosol phase
877 (Höpfner et al. (2019); Wang et al. (2020)) or organics should promote the NPF of H_2SO_4 in the
878 TTL even at low supersaturations (Metzger et al. (2010); Kerminen et al. (2010); Kirkby et al.
879 (2011); Kürten (2019);(Wang et al., 2020)). The supersaturation required for initiating NPF
880 could temporally result from local cooling. Gravity waves (GWs) represent low-frequency
881 inertial perturbations of the initial atmospheric state. Such a perturbation is expressed
882 particularly by a change in velocity of the vertical wind component. The passage of a GW is
883 associated with a change in the vertical displacement of an air parcel and thus causes locally an
884 adiabatic heating/cooling by a certain absolute value ΔT .

885 Piani et al. (2000) provided simulations of GWs initiated by deep convection. Their studies
886 reveal a concentric propagation of GWs at altitudes above 15 km and up to ~ 40 km with
887 wavelengths in the horizontal of about 40 km and of $\sim 4 - 7$ km in the vertical. Similar results
888 were found to be typical by other simulation studies concerning GW propagation at mid-
889 latitudes (Song et al. (2003) and Chun and Kim (2008)) or in the tropics (Lane and Moncrieff,
890 2008). Investigations related to GWs in connection with the monsoon are sparse, e.g. Wright and

891 Gille (2011) and Ern and Preusse (2012) used satellite observations (High Resolution Dynamics
892 Limb Sounder) which, however, are limited to detections of GWs with horizontal wavelengths
893 greater than ~ 300 km. Despite the numerous observational studies concerning GW properties
894 (Alexander et al., 2010), the indirect retrieval of GWs' horizontal wavelengths remains uncertain
895 by a factor of two (or more), whereas instrumental limitations inhibit the GW detection at
896 horizontal wavelengths smaller than 100 km. Based on radiosonde measurements (Vincent and
897 Alexander, 2000), a 6-year averaged amplitude of 1.5 K is reported as an effect of GWs, with a
898 single-case example of ~ 4 K-amplitude around 20 km altitude in the tropics.

899 Satellite images over the Indian subcontinent (e.g. from MSG-1 or HIMAWARI, cf.
900 <https://www.eorc.jaxa.jp/ptree/index.html>) indicate quite frequent occurrences of convective
901 plumes in the sampling areas during the StratoClim 2017 mission period, which occasionally
902 arranged in chains of convective cells along the Himalayan foothills. The StratoClim flight KTM 6
903 on 06 August 2017 enabled NPF observations immediately connected to convection, which
904 penetrated through the flight level on passage at constant flight altitude. The corresponding part
905 of the time series shown in Figure 13 covers the probing period in the air sector over
906 Bangladesh and the Bay of Bengal (cf. Figure 1). Two phases of NPF observations are highlighted
907 (hatched areas in Figure 13), immediately before and after the period between 09:20 and 09:30
908 (UTC), during which the flight altitude changed from 16.2 km to about 13.8 km with subsequent
909 re-ascent to 16.2 km. The manoeuvre above the northern part of the Bay of Bengal also marks
910 the turning point of the mission flight path and the two flanking NPF phases were encountered
911 over the mainland near the coastlines of East India and Bangladesh (cf. Figure 1 b). The
912 outbound and return sections of the flight passed through the same convectively active region,
913 and the same convective system was likely probed at opposite positions.

914 Within the limits of the displayed time series (Figure 13 a) constant flight altitude and pressure
915 level were maintained, except for the turning manoeuvre, which was disregarded in the
916 following discussion. The mixing ratios n_6 , n_{10} and n_{15} coincidentally exhibited increased values
917 of variable strength (Figure 13 b), whereas during both NPF phases the particle mixing ratios
918 n_{nm} are elevated (> 10000 mg $^{-1}$) or peak up to values of more than 20000 mg $^{-1}$. The course of n_{nm}
919 is not mirrored by the CO signal (Figure 13 d), e.g. n_{nm} is at maximum values when CO is still at
920 intermediate levels of ~ 110 nmol mol $^{-1}$. In both NPF phases, the peaks of air's CO content (130 -
921 140 nmol mol $^{-1}$, Figure 13 d) were accompanied by increasing mixing ratios n_{10nv} by a factor of

922 up to two compared to the background (Figure 13 b), indicating the passage through the
923 convective outflow plume, which also contained non-volatile aerosol material that was lifted
924 together with gaseous pollutants.

925 During the periods of the NPF observations, however, the ambient air temperature T_{amb} (Figure
926 13 e) visibly fluctuates in the order of ± 1 K around the respective mean temperature
927 ($T_{\text{mean}} = 193$ K with standard deviation below 1 K). Over the NPF period, the time series of the
928 temperature fluctuation ($T_{\text{amb}} - T_{\text{mean}}$, Figure 13 e) exhibits the shape of a wave.

929 Figure 14 shows close-ups of the time series covering slightly more than one hour of
930 measurement on level flight, including the two periods of observed NPF (Panels a and b,
931 respectively). The curves exhibit the untreated 1 Hz temperature data set ($T_{1\text{Hz}}$) and the noise-
932 filtered data set (T_{201}). The filtering was applied using a running average over 201 data points
933 (see Appendix B for details). The filtered data (T_{201}) is additionally approximated with an
934 overlaid wave fit (cf. Appendix B and Table 2), which aimed at the requirement to reproduce the
935 temperature variation, in particular during the periods of NPF observation. The noise level over
936 the intervals of the mapped time series holds a fairly constant standard deviation σ of about
937 ± 0.25 K. In maxima, the scattering peaks slightly above the 3σ noise level (i.e. about ± 0.75 K),
938 which likely accounts for the largest proportion of uncertainty in the temperature data for this
939 measurement period. The applied fit functions reproduce the wave-like character of the
940 temperature fluctuation during two NPF events with estimated wavelengths between 70 km and
941 100 km (for the higher frequency, while in the range of 400 km for the lower frequency). The
942 quality of approximating the noise-reduced data by overlaid wave fit provides indications that
943 the observed temperature fluctuation is subject to a wave that coincides well with the
944 occurrence of NPF.

945 It would go beyond the scope of this study to clearly attribute this temperature fluctuation to the
946 GW activity initiated by one specific or several convective systems. However, the amplitude and
947 wavelength of the observed fluctuation correspond qualitatively and quantitatively to the values
948 typical for GWs. Simplified estimates reveal that an increase of the H_2SO_4 saturation ratio by a
949 factor of about 1.75 – 2 readily occurs when the initial ambient temperature (e.g. at $T_0 \approx 190$ K)
950 drops by 2 K (cf. Appendix B). If NPF is initialised by a negative temperature anomaly under

951 supersaturated conditions, the newly formed nucleation-mode particles hardly evaporate at re-
952 rising temperatures (e.g. when the GW-induced temperature anomaly becomes positive).

953 The horizontal extent of GW-induced temperature anomalies, which can range from a few to
954 hundreds of kilometres, is generally comparable with the magnitude of the horizontal extent of
955 observed NPF fields (cf. Sections 0 and 4.3 as well as Figure 5 c). Since the time offset between
956 NPF observation and NPF initiation is not exactly known, it is not straightforward to connect
957 individual NPF events to specific incidents of GW-induced temperature anomalies. Moreover,
958 during the monsoon season, several widely distributed, convective systems may induce GWs at
959 the same time and the resulting, spatially propagating, temperature anomalies could interfere at
960 TTL heights. The amplification of temperature anomalies inherent with such interferences is
961 neither locally resolvable nor quantifiable. Hence, GW-induced temperature anomalies can
962 additionally promote the occurrence of NPF.

963 **7 Summary and Conclusions**

964 Between 27 July and 10 August 2017 the airborne StratoClim 2017 mission took place in
965 Kathmandu, Nepal, with eight mission flights (~ 22.5 hours of COPAS measurement time above
966 10 km, $\theta \gtrsim 350$ K) up to altitudes of 20 km ($\theta \approx 475$ K) with the Russian high-altitude research
967 aircraft M-55 *Geophysica*. The presented analysis comprises the description and discussion of
968 numerous events of New Particle Formation (NPF), which were observed in the UT/LS region of
969 the Asian Monsoon Anticyclone (AMA) over northern India, Nepal and Bangladesh.

970 In total, a duration of 2 hours and 38.5 minutes was spent under NPF conditions in the region of
971 the Tropical Tropopause Layer (TTL), where enhanced quantities of nucleation-mode particles
972 of up to $\sim 50000 \text{ mg}^{-1}$ ($\approx 11000 \text{ cm}^{-3}$) were detected at heights of 15 – 16 km (~ 370 K). The
973 majority of NPF observations with high numbers of nucleation-mode particles
974 ($6 \text{ nm} < d_p < 15 \text{ nm}$) were observed below the tropopause ($\sim 12\text{-}16$ km, $\sim 355 - 380$ K), at the
975 lower TTL. NPF with intermediate ($\sim 1000 - 2000 \text{ mg}^{-1}$) or low ($\sim 300 - 500 \text{ mg}^{-1}$) mixing ratios
976 of nucleation-mode particles were also observed around the tropopause (~ 380 K) and up to
977 about 17.5 km altitude (400 K). The frequency of intense NPF observed during StratoClim 2017
978 exceeds all previous NPF detections with COPAS in the TTL over Brazil, Australia, and West
979 Africa (TROCCINOX 2005, SCOUT-O3 2005, SCOUT-AMMA 2006, cf. Borrmann et al. (2010);
980 Weigel et al. (2011)). The maximum of detected nucleation-mode particles ($\sim 50000 \text{ mg}^{-1}$,

981 correspondent to $\sim 11000 \text{ cm}^{-3}$ under ambient conditions at $360 \text{ K} < \theta < 370 \text{ K}$) is in comparable
982 orders of magnitude to the earlier COPAS observations (*ibid*). The horizontal extent of the NPF
983 fields during StratoClim 2017, ranging from a few hundred metres to about one hundred
984 kilometres, well compares to previous COPAS observations in the tropics.

985 Mainly due to coagulation, the persistence of nucleation-mode particles ($d_p < 15 \text{ nm}$) in the
986 presence of the background aerosol population is limited to few hours only. Within the
987 supersaturated environment under NPF conditions, co-condensation of gaseous species other
988 than NPF precursors further promotes the growth of nucleation-mode particles. The
989 comparatively short persistence of the particles in the nucleation-mode size range implies:

- 990 • Within 2 hours after a NPF event, the number concentration of nucleation-mode particles
991 decays due to coagulation by more than one order of magnitude.
- 992 • About 3-4 hours after a NPF event, the reduced number of nucleation-mode particles
993 impedes the identification of NPF events based on aircraft-borne *in-situ* measurements.
- 994 • Low and intermediate numbers of nucleation-mode particles result from either moderate
995 and just proceeding NPF or from an event with elevated NPF-rate that has phased-out over
996 more than two hours before the measurement.
- 997 • Identified NPF events with high amounts of nucleation-mode particles i.e. ($> 10000 \text{ mg}^{-1}$)
998 have occurred very shortly (less than one hour) prior to the measurement or are just
999 proceeding when detected.

1000 The supersaturated conditions, under which NPF occurs also favour the co-condensation of
1001 gaseous substances (Yu et al., 2017). Whether coagulation or condensation predominantly
1002 contributes to the composition of the background aerosol remains open. Most likely, both
1003 processes impact the formation and persistence of the ATAL (Vernier et al. (2011a), and see also
1004 Höpfner et al. (2019); Mahnke et al. (2021)), which was mainly attributed to the uplift of
1005 pollution from the boundary layer (Vernier et al. (2018); Brunamonti et al. (2018); Hanumanthu
1006 et al. (2020)).

1007 Generally, a refractory core with diameter greater than 10 nm was detected in almost every
1008 second particle above 395 K and up to 475 K. In addition to the local particle source by NPF,
1009 additional particulate material is vertically transported by the updraught within the AMA (cf.

1010 also Section 6). At altitudes above 18 km, the contribution of meteoric particles from further
1011 aloft was found by means of *in-situ* aerosol mass spectrometry during StratoClim 2017
1012 (Schneider et al., 2020).

1013 At altitudes of up to 17.5 km, the fresh particles from NPF are in place for being lifted by a
1014 sufficiently effective transport mechanism to indirectly supply the stratospheric (Junge) aerosol
1015 layer. However, whether aerosol material subsides from TTL levels to mid-tropospheric
1016 altitudes and possibly contributes to cloud formation, as suggested by Andreae et al. (2018) to
1017 happen in the Amazon region, depends on the efficiency of downward transport, and on the
1018 aerosol's capability as CCN. Condensation of gaseous species other than those involved in the
1019 NPF process, and internal chemical conversion of various solutes within a particle influence the
1020 aerosols' CCN capabilities. The required transport times to reach altitudes far above or below
1021 the TTL range over several days to weeks and stay in contrast to the short persistence (hours) of
1022 nucleation-mode particles.

1023 Moreover, the StratoClim 2017 measurements revealed:

1024 (1) that highest n_{nm} values were predominantly found to coincide with intermediate to elevated
1025 CO mixing ratios of ~ 100 nmol mol⁻¹. Beyond that, the mixing ratio of nucleation-mode particles
1026 ($\sim 700 - 20000$ mg⁻¹) is largely independent of the CO content (between 80 and 145 nmol mol⁻¹)
1027 of the air at the lower TTL.

1028 (2) The most intensive uplift of air was confirmed to occur over the Himalayan mountain chain
1029 and its foothills. However, particular source regions of NPF precursors were not ascertainable
1030 within the BL. No indication was found that the most intense NPF was connected to short
1031 durations of air mass transport from the BL into the TTL.

1032 (3) The convective contribution to the air mass composition did not determine the intensity of
1033 the observed NPF. The release of the precursor material in the outflow region of the convective
1034 top had occurred up to 6 days before the NPF observation. Occasionally, however, air mass
1035 residence times of more than 6 days and up to 14 days were found at TTL levels prior to the NPF
1036 detection while the entire data set covers residence times from ~ 3 hours to about 26 days.

1037 For the period of the StratoClim 2017 mission, the observed NPF rates are not unambiguously
1038 attributable to a) a specific source region in the BL, or b) the effectiveness of the convective
1039 vertical transport, or c) the recent release of NPF-capable material from the convective outflow.

1040 Nevertheless, it is the convective uplift, which intermittently supplies the lower TTL by NPF
1041 precursor material. At altitudes well above tropopause levels, such an immediate supply by
1042 convection is lacking and could alternatively only proceed by the slow uplift superimposed on
1043 the anticyclonic ascent of the AMA (~ 1 K per day, Vogel et al. (2019); von Hobe et al. (2020)).

1044 Alternatively, adiabatic cooling could induce sufficient supersaturation of a NPF precursor e.g.
1045 due to temperature anomalies associated with gravity waves (GW). Presented case study based
1046 on a continuous level flight segment (flight KTM 6 on 06 August 2017), revealed wave-like
1047 temperature anomalies with a peak-to-peak amplitude of $\Delta T = 2$ K and a horizontal wavelength
1048 of 70 – 100 km, which matched well with two independent NPF events. Hence, the vertical
1049 propagation of GW-induced temperature anomalies can initialise NPF above tropopause levels,
1050 a) where ambient air temperatures re-increase with altitude (from observational data with
1051 $\Delta T \approx 1.5$ K per $\Delta \theta = 10$ K), which principally counteracts the supersaturation of a precursor, and
1052 b) where in the absence of deep convection a direct supply of precursor material from below is
1053 lacking.

1054 The observations made during StratoClim 2017 demonstrate that frequent NPF with high
1055 production of nucleation-mode particles is capable of directly affecting the extent and
1056 persistence of the Asian Tropopause Aerosol Layer (ATAL). The continuous supply of freshly
1057 formed aerosol material, which coagulates both internally and with the background aerosol, and
1058 which itself provides a surface for the condensation of supersaturated gaseous substances,
1059 contributes significantly to the available aerosol material that composes the ATAL. In this case,
1060 the chemical composition of the ATAL aerosol includes significant fractions of the material,
1061 which was previously involved in the NPF process and the particles' condensational growth,
1062 which is subject to further investigation using the StratoClim 2017 data set.

1063 Data availability:

1064 *The data shown in this study are available at the StratoClim campaign database at*

1065 <https://stratoclim.icg.kfa-juelich.de/AfcMain/CampaignDataBase>

1066 *or they may be provided by respective PI upon request*

1067 Author contribution

1068 *RW evaluated and analysed the data, created the figures, and drafted the manuscript with contributions by CM,*
1069 *MB, and AD. SB participated in the data analyses and the manuscript drafting. The code of the coagulation*
1070 *simulation was provided by BPL, and the code was adapted by MB while the calculations were performed by*
1071 *CM. BV, FP contributed with meteorological re-analyses, BV, SiB, and BL performed the air mass trajectory*
1072 *analyses. SV and FD'A took care of the CO data. UCSE data were delivered by GB. The manuscript was*
1073 *reviewed by CM, MB, AD, BV, FP, SV, FD'A, SiB, BL, BPL, and SB.*

1074 **Competing interests**

1075 *The authors declare no competing interests.*

1076 **Acknowledgements**

1077 The contributions from the technical staff at the workshops of the MPI for Chemistry and the
1078 Institute for Physics of the Atmosphere (Mainz University), as well as the Myasishchev Design
1079 Bureau (MDB) were essential. In particular, we acknowledge support of T. Böttger, M. Flanz and
1080 W. A. Schneider. We thank Y.-H. Kim, P. Spichtinger, H. Tost, M. Szakáll, A. Theis, and A.
1081 Miltenberger, T. Thornberry and the ACCLIP-team for very helpful discussions. Many thanks to
1082 T. Peter for the planning of flight KTM 6 on 06 August 2017. The extraordinary commitment of F.
1083 Stroh in realisation of the campaign and the leadership of the entire StratoClim project by M. Rex
1084 are gratefully acknowledged. We very much thank the MDB crew and the M-55 Geophysica
1085 pilots. Some of our research leading to the presented results received funding from the
1086 European Research Council under the European Union's Seventh Framework Program
1087 (FP/2007-2013)/ERC Grant Agreement No. 321040 (EXCATRO). The StratoClim project was
1088 funded by the EU (FP7/2007–2018 Grant No. 603557) and also supported by the German
1089 “Bundesministerium für Bildung und Forschung” (BMBF) under the joint ROMIC-project
1090 SPITFIRE (01LG1205A). The work presented includes contributions to the China-NSFC-DFG
1091 2020 project ATALtrack (BO 1829/12-1 and VO 1276/6-1). We explicitly thank the officials of
1092 the Nepalese government authorities, research institutions, and Tribhuvan Airport as well as of
1093 the German Embassy for their extraordinary support and hospitality, which enabled our field
1094 campaign and research.

1095 **Appendix A : The detection of non-volatile particles with COPAS**

1096 COPAS includes a vaporiser based on an established and commonly used technique. One of the
1097 four COPAS channels is equipped with a heated stainless steel tube (at $\sim 270^\circ\text{C}$) to vaporise
1098 volatile compounds upstream of one of the particle detectors. The specific heating temperature
1099 is chosen with the aim to vaporise mainly stratospheric particle species, which typically consist
1100 of aqueous solutions of sulphuric acid ($\text{H}_2\text{SO}_4\text{-H}_2\text{O}$) and/or nitric acid ($\text{HNO}_3\text{-H}_2\text{O}$), which
1101 reportedly volatilise at 180°C (Rosen, 1971). In addition, most of volatile and several semi-
1102 volatile organic compounds can evaporate at colder temperatures than 270°C . Conversely, this
1103 means that an undeterminable proportion of semi-volatile and probably highly oxidised
1104 organics, whose role as agents in NPF has been identified by Kurtén et al. (2008) or Riccobono et
1105 al. (2014), can pass through the preheater without being significantly altered. Downstream of

1106 the heated tube section, the re-condensation of evaporated species is not completely excludable.
1107 Due to the high diffusivity of e.g. H₂SO₄ molecules (a factor of up to 0.5 of the diffusivity of H₂O,
1108 cf. Tang et al. (2014)), the re-condensation is expected to occur predominantly at the tube's
1109 inner walls, since thermophoresis drives the vapour molecules from the previously heated air
1110 sample towards the cold walls. Such a re-condensation affects the particles' size not their
1111 number, and condensation on the largest of the non-volatile residues is favoured over the
1112 smaller ones (i.e. those with $d_p < 10$ nm). The working principle of the COPAS aerosol vaporiser
1113 was demonstrated by means of laboratory experiments with pure H₂SO₄-H₂O particles of several
1114 sizes and at pressure conditions between 70 – 300 hPa (Weigel et al., 2009); more than 98 % of
1115 the sub-micrometre sized H₂SO₄-H₂O particles were volatilised. As the refractory material, which
1116 could be detectable with COPAS, is unlikely to be generated by the heater itself, such
1117 instrumental artefacts are largely excluded. To avoid artefacts as a result, e.g., of re-suspension
1118 of aerosol material, which had been deposited on the tube's inner walls during previous
1119 operations, the sample lines were flush-cleaned with ethanol and distilled water, at least before
1120 every second mission flight. Inefficiencies of the vaporiser, e.g. due to diminished heat transfer
1121 from the tube's inner wall to the passing aerosol particles, particularly at low atmospheric
1122 pressures, would cause the number (fraction) of detected refractory particles to be unexpectedly
1123 high (≈ 100 %) over extended measurement periods, which was not observed throughout the
1124 field missions (cf. Borrmann et al. (2010); Weigel et al. (2011)). Conversely, instrumental
1125 artefacts inherent with the vaporiser's tube length, e.g. particle loss, would lead to comparatively
1126 low number concentrations of detected refractory particles. Diffusional loss effects increase with
1127 decreasing pressure, but thermophoresis counteracts the particles' diffusion towards the hot
1128 tube walls. With the same vaporiser system, Weigel et al. (2014) observed rising mixing ratios of
1129 refractory aerosol, most likely from meteoric ablation, with altitude at stratospheric levels inside
1130 the polar vortex, while outside the vortex the amount of refractory aerosols nearly stagnated
1131 over the corresponding altitude range, additionally confirming the principle function of the
1132 vaporiser.

1133 **Appendix B: Case study analysis of observed temperature anomaly**

1134 For analysing the observed temperature anomaly in the time intervals of the NPF events a
1135 running average is used as filter to suppress the high-frequency noise on the temperature data.
1136 The running average over 201 measurement points (i.e. over 100 data points before and 100

1137 data points after each 1 Hz-temperature measurement) is used; Figure A- 1 illustrates the
 1138 effectiveness of the filtering. As a result of subtracting the low-pass filtered temperature data
 1139 (T_{201}) from the initial 1 Hz-resolved temperature data (T_{1Hz}), the high-frequency noise remains
 1140 (red dots in Figure A- 1). The noise scatters around the zero level with a maximum amplitude of
 1141 about ± 0.75 K. The filtering by the running mean turns out as equally effective inside and
 1142 outside the observed NPF events with presumed temperature fluctuation. The indicated
 1143 reference lines for the $\pm 1 \sigma$ and $\pm 3 \sigma$ levels (where σ denotes the standard deviation) illustrate
 1144 the noise amplitude, which remains fairly constant (during NPF and away from observed NPF
 1145 events) over the entire period and also almost within the $\pm 3 \sigma$ - range. The course of the T_{201}
 1146 curves thus represents the temperature fluctuation by excluding the noise, which underlies the
 1147 measurement. The T_{201} curve is approximated by a wave fit (T_{Fit}) for reproducing the
 1148 temperature fluctuation in the filtered data set (T_{201}) particularly during the periods of NPF
 1149 observation (cf. Section 6 and Figure 14).

1150 The basic form of the wave fit function is:

1151
$$f(x, a, b, c, d) = d + a \cdot \sin(b x + c) \quad \mathbf{A- 1}$$

1152 with

1153 x = horizontal distance derived from time UTC, day seconds, and mean airspeed,

1154 a = the amplitude

1155 b = the frequency

1156 c = the phase shift

1157 d = the offset

1158 For each of the two time periods with identified NPF, an individual fit was determined with the
 1159 parameters from Table 2 and each fit consists of a sum of two functions of the type defined in
 1160 Equation A-1. During the NPF event the difference between the two curves, T_{201} and T_{Fit} (Figure
 1161 A- 1), shows, that the overlaid wave fit approximates the filtered data with a smaller deviation
 1162 than given with the $\pm 1 \sigma$ - noise level. The difference between the 1 Hz-temperature signal and
 1163 the wave fit is also shown in Figure A- 1. During the NPF event, the subtraction of the wave fit
 1164 from the 1 Hz-data has almost the same effect as the subtraction of the filter T_{201} from T_{1Hz} ,
 1165 therefore, in the NPF period, the deviation between the two sets of data ($T_{1Hz} - T_{Fit}$) corresponds
 1166 mainly to the noise of the temperature measurement. Away from the NPF event, the deviation of

1167 the wave fit from T_{1Hz} and T_{201} increases as the approximation of the temperature data by the
 1168 wave function was constrained to the NPF period.

1169 **Appendix C: The impact of a temperature anomaly on the saturation ratio of H_2SO_4**

1170 The passage of a gravity wave is associated with adiabatic heating/cooling by a certain amount
 1171 ΔT . According to Vincent and Alexander (2000) (cf. also Section 6), the maximum realistic value
 1172 of ΔT is ~ 4 K. Smaller temperature perturbations occur more frequently. An air parcel at
 1173 pressure p_0 and temperature T_0 , which is vertically and adiabatically displaced, changes its
 1174 pressure and temperature to the new values p and $T = T_0 + \Delta T$. The question arises as to how
 1175 temperature anomalies influence the occurrence of NPF. In this context, NPF is initialised when
 1176 the saturation of a nucleating gas or gas mixture exceeds a certain level. Pure sulphuric acid is
 1177 certainly not the exclusive gas species involved in NPF, but if temperature anomalies sufficiently
 1178 affect the saturation ratio of pure H_2SO_4 , then additional agents such as ammonium (Höpfner et
 1179 al., 2019) or organics (Kürten, 2019) could more readily favour the initiation of NPF.

1180 Adiabaticity of the process is presumed and by approximating the gas constant R and the heat
 1181 capacity c_p with the values for dry air ($R \approx R_a$ and $c_p \approx c_{pa}$), the ideal gas equation can be
 1182 converted such that the mixing-ratio $q_{H_2SO_4}$ of sulphuric acid is related to its partial pressure
 1183 $p_{H_2SO_4}$. Since the conditions within the AMA change rather slowly, the mixing of air masses is
 1184 considered as negligible. Hence, the concentration of each gas species within the air parcel
 1185 remains invariant to the vertical displacement. In the following, $p_{H_2SO_4, 0}$ is the sulphuric acid
 1186 partial pressure within the unperturbed air parcel. Denoting the saturation vapour pressure of
 1187 sulphuric acid by p_{sat} , the ratio of the saturation ratio of the unperturbed air parcel and the
 1188 displaced air parcel reads as

$$\begin{aligned}
 \frac{S}{S_0} &:= \frac{\frac{p_{H_2SO_4}}{p_{sat}(T)}}{\frac{p_{H_2SO_4,0}}{p_{sat}(T_0)}} = \frac{p_{H_2SO_4}}{p_{H_2SO_4,0}} \frac{p_{sat}(T_0)}{p_{sat}(T)} \\
 &= \frac{p}{p_0} \frac{p_{sat}(T_0)}{p_{sat}(T)} \\
 &= \left(\frac{T}{T_0}\right)^{\frac{c_{pa}}{R_a}} \frac{p_{sat}(T_0)}{p_{sat}(T)}
 \end{aligned}$$

$$\begin{aligned}
1193 \quad &= \left(\frac{T_0 + \Delta T}{T_0} \right)^{\frac{c_{pa}}{R_a}} \frac{p_{sat}(T_0)}{p_{sat}(T_0 + \Delta T)} \\
1194 \quad &= \left(1 + \frac{\Delta T}{T_0} \right)^{\frac{c_{pa}}{R_a}} \frac{p_{sat}(T_0)}{p_{sat}(T_0 + \Delta T)} \\
1192 \quad &\approx \frac{p_{sat}(T_0)}{p_{sat}(T_0 + \Delta T)} . \qquad \qquad \qquad \mathbf{A-2}
\end{aligned}$$

1195 Figure A- 2 exhibits the quotient $\frac{S}{S_0}$ (i.e. the factorial increase of the saturation ratio S in
1196 reference to an initial saturation ratio S_0 at undisturbed conditions, including supersaturated
1197 states) for several initial states of ambient air temperature T_0 (from 185 K to 250 K) and for a
1198 range of temperature anomalies with ΔT of up to 4 K. It is to be emphasised that these
1199 calculations relate specifically to the impact of temperature anomalies on the supersaturation of
1200 pure H_2SO_4 . These estimates based on ordinary precursors (i.e. H_2SO_4 - H_2O) do not allow for
1201 conclusions concerning the NPF efficiency of complex systems of precursor compositions (e.g.
1202 including ammonia or organics). The demonstrated effect, however, is qualitatively transferable
1203 to any gaseous substance while the nucleation of particles from the gas-phase requires
1204 sufficiently high saturation ratios of the respective species or gas mixture and may be of
1205 particular interest in the context of the CLOUD experiments at CERN with H_2SO_4 (cf. Stolzenburg
1206 et al. (2020)) under variable conditions and various admixtures.

1207 **References**

- 1208 Alexander, M. J., Geller, M., McLandress, C., Polavarapu, S., Preusse, P., Sassi, F., Sato, K.,
1209 Eckermann, S., Ern, M., Hertzog, A., Kawatani, Y., Pulido, M., Shaw, T. A., Sigmond, M., Vincent, R.,
1210 and Watanabe, S.: Recent developments in gravity-wave effects in climate models and the global
1211 distribution of gravity-wave momentum flux from observations and models, *Q J Roy Meteor Soc*,
1212 136, 1103-1124, 10.1002/qj.637, 2010.
- 1213 Andreae, M. O., Afchine, A., Albrecht, R., Holanda, B. A., Artaxo, P., Barbosa, H. M. J., Borrmann, S.,
1214 Cecchini, M. A., Costa, A., Dollner, M., Fütterer, D., Järvinen, E., Jurkat, T., Klimach, T., Konemann,
1215 T., Knote, C., Krämer, M., Krisna, T., Machado, L. A. T., Mertes, S., Minikin, A., Pöhlker, C., Pöhlker,
1216 M. L., Pöschl, U., Rosenfeld, D., Sauer, D., Schlager, H., Schnaiter, M., Schneider, J., Schulz, C., Spanu,
1217 A., Sperling, V. B., Voigt, C., Walser, A., Wang, J., Weinzierl, B., Wendisch, M., and Ziereis, H.:
1218 Aerosol characteristics and particle production in the upper troposphere over the Amazon
1219 Basin, *Atmos Chem Phys*, 18, 921-961, 10.5194/acp-18-921-2018, 2018.
- 1220 Barth, M. C., Stuart, A. L., and Skamarock, W. C.: Numerical simulations of the July 10, 1996,
1221 Stratospheric-Tropospheric Experiment: Radiation, Aerosols, and Ozone (STERAO)-Deep
1222 Convection experiment storm: Redistribution of soluble tracers, *J Geophys Res-Atmos*, 106,
1223 12381-12400, Doi 10.1029/2001jd900139, 2001.
- 1224 Baumgartner, M., Weigel, R., Achatz, U., Harvey, A. H., and Spichtinger, P.: Reappraising the
1225 appropriate calculation of a common meteorological quantity: Potential Temperature, *Atmos.*
1226 *Chem. Phys. Discuss.*, 2020, 1-43, 10.5194/acp-2020-361, 2020.
- 1227 Bergman, J. W., Jensen, E. J., Pfister, L., and Yang, Q.: Seasonal differences of vertical-transport
1228 efficiency in the tropical tropopause layer: On the interplay between tropical deep convection,
1229 large-scale vertical ascent, and horizontal circulations, *J Geophys Res-Atmos*, 117, Artn
1230 D0530210.1029/2011jd016992, 2012.
- 1231 Bergman, J. W., Fierli, F., Jensen, E. J., Honomichl, S., and Pan, L. L.: Boundary layer sources for the
1232 Asian anticyclone: Regional contributions to a vertical conduit, *J Geophys Res-Atmos*, 118, 2560-
1233 2575, 10.1002/jgrd.50142, 2013.
- 1234 Bianchi, F., Junninen, H., Bigi, A., Sinclair, V. A., Dada, L., Hoyle, C. R., Zha, Q., Yao, L., Ahonen, L. R.,
1235 Bonasoni, P., Buenrostro Mazon, S., Hutterli, M., Laj, P., Lehtipalo, K., Kangasluoma, J., Kerminen,
1236 V. M., Kontkanen, J., Marinoni, A., Mirme, S., Molteni, U., Petäjä, T., Riva, M., Rose, C., Sellegri, K.,
1237 Yan, C., Worsnop, D. R., Kulmala, M., Baltensperger, U., and Dommen, J.: Biogenic particles formed
1238 in the Himalaya as an important source of free tropospheric aerosols, *Nat Geosci*, 14, 4-9,
1239 10.1038/s41561-020-00661-5, 2021.
- 1240 Borrmann, S., Kunkel, D., Weigel, R., Minikin, A., Deshler, T., Wilson, J. C., Curtius, J., Volk, C. M.,
1241 Homan, C. D., Ulanovsky, A., Ravegnani, F., Viciani, S., Shur, G. N., Belyaev, G. V., Law, K. S., and
1242 Cairo, F.: Aerosols in the tropical and subtropical UT/LS: in-situ measurements of submicron
1243 particle abundance and volatility, *Atmos Chem Phys*, 10, 5573-5592, 10.5194/acp-10-5573-
1244 2010, 2010.
- 1245 Brock, C. A., Hamill, P., Wilson, J. C., Jonsson, H. H., and Chan, K. R.: Particle Formation in the
1246 Upper Tropical Troposphere: A Source of Nuclei for the Stratospheric Aerosol, *Science*, 270,
1247 1650-1653, 10.2307/2887916, 1995.
- 1248 Brock, C. A., Schröder, F., Kärcher, B., Petzold, A., Busen, R., and Fiebig, M.: Ultrafine particle size
1249 distributions measured in aircraft exhaust plumes, *Journal of Geophysical Research:*
1250 *Atmospheres*, 105, 26555-26567, 10.1029/2000jd900360, 2000.

- 1251 Brunamonti, S., Jorge, T., Oelsner, P., Hanumanthu, S., Singh, B. B., Kumar, K. R., Sonbawne, S.,
1252 Meier, S., Singh, D., Wienhold, F. G., Luo, B. P., Boettcher, M., Poltera, Y., Jauhiainen, H., Kayastha,
1253 R., Karmacharya, J., Dirksen, R., Naja, M., Rex, M., Fadnavis, S., and Peter, T.: Balloon-borne
1254 measurements of temperature, water vapor, ozone and aerosol backscatter on the southern
1255 slopes of the Himalayas during StratoClim 2016-2017, *Atmos Chem Phys*, 18, 15937-15957,
1256 10.5194/acp-18-15937-2018, 2018.
- 1257 Bucci, S., Legras, B., Sellitto, P., D'Amato, F., Viciani, S., Montori, A., Chiarugi, A., Ravegnani, F.,
1258 Ulanovsky, A., Cairo, F., and Stroh, F.: Deep convective influence on the UTLS composition in the
1259 Asian Monsoon Anticyclone region: 2017 StratoClim campaign results, *Atmos. Chem. Phys.*
1260 *Discuss.*, 2020, 1-29, 10.5194/acp-2019-1053, 2020.
- 1261 Campbell, P., and Deshler, T.: Condensation nuclei measurements in the midlatitude (1982–
1262 2012) and Antarctic (1986–2010) stratosphere between 20 and 35 km, *Journal of Geophysical*
1263 *Research: Atmospheres*, 119, 2013JD019710, 10.1002/2013jd019710, 2014.
- 1264 Chirkov, M., Stiller, G. P., Laeng, A., Kellmann, S., von Clarmann, T., Boone, C. D., Elkins, J. W.,
1265 Engel, A., Glatthor, N., Grabowski, U., Harth, C. M., Kiefer, M., Kolonjari, F., Krummel, P. B., Linden,
1266 A., Lunder, C. R., Miller, B. R., Montzka, S. A., Muhle, J., O'Doherty, S., Orphal, J., Prinn, R. G., Toon,
1267 G., Vollmer, M. K., Walker, K. A., Weiss, R. F., Wiegele, A., and Young, D.: Global HCFC-22
1268 measurements with MIPAS: retrieval, validation, global distribution and its evolution over 2005–
1269 2012, *Atmos Chem Phys*, 16, 3345-3368, 10.5194/acp-16-3345-2016, 2016.
- 1270 Chun, H.-Y., and Kim, Y.-H.: Secondary waves generated by breaking of convective gravity waves
1271 in the mesosphere and their influence in the wave momentum flux, *Journal of Geophysical*
1272 *Research: Atmospheres*, 113, 10.1029/2008jd009792, 2008.
- 1273 Crumeyrolle, S., Manninen, H. E., Sellegri, K., Roberts, G., Gomes, L., Kulmala, M., Weigel, R., Laj, P.,
1274 and Schwarzenboeck, A.: New particle formation events measured on board the ATR-42 aircraft
1275 during the EUCAARI campaign, *Atmos. Chem. Phys.*, 10, 6721-6735, 10.5194/acp-10-6721-2010,
1276 2010.
- 1277 Crutzen, P. J., and Lawrence, M. G.: The impact of precipitation scavenging on the transport of
1278 trace gases: A 3-dimensional model sensitivity study, *J Atmos Chem*, 37, 81-112, Doi
1279 10.1023/A:1006322926426, 2000.
- 1280 Curtius, J., Weigel, R., Vossing, H. J., Wernli, H., Werner, A., Volk, C. M., Konopka, P., Krebsbach, M.,
1281 Schiller, C., Roiger, A., Schlager, H., Dreiling, V., and Borrmann, S.: Observations of meteoric
1282 material and implications for aerosol nucleation in the winter Arctic lower stratosphere derived
1283 from in situ particle measurements, *Atmos Chem Phys*, 5, 3053-3069, DOI 10.5194/acp-5-3053-
1284 2005, 2005.
- 1285 de Reus, M., Borrmann, S., Bansemmer, A., Heymsfield, A. J., Weigel, R., Schiller, C., Mitev, V., Frey,
1286 W., Kunkel, D., Kurten, A., Curtius, J., Sitnikov, N. M., Ulanovsky, A., and Ravegnani, F.: Evidence
1287 for ice particles in the tropical stratosphere from in-situ measurements, *Atmos Chem Phys*, 9,
1288 6775-6792, DOI 10.5194/acp-9-6775-2009, 2009.
- 1289 Dee, D. P., Uppala, S. M., Simmons, A. J., Berrisford, P., Poli, P., Kobayashi, S., Andrae, U.,
1290 Balsameda, M. A., Balsamo, G., Bauer, P., Bechtold, P., Beljaars, A. C. M., van de Berg, L., Bidlot, J.,
1291 Bormann, N., Delsol, C., Dragani, R., Fuentes, M., Geer, A. J., Haimberger, L., Healy, S. B., Hersbach,
1292 H., Hólm, E. V., Isaksen, I., Kållberg, P., Köhler, M., Matricardi, M., McNally, A. P., Monge-Sanz, B.,
1293 Morcrette, J. J., Park, B. K., Peubey, C., de Rosnay, P., Tavolato, C., Thépaut, J. N., and Vitart, F.:
1294 The ERA-Interim reanalysis: configuration and performance of the data assimilation system, *Q J*
1295 *Roy Meteor Soc*, 137, 553-597, 10.1002/qj.828, 2011.

- 1296 Dunne, E. M., Gordon, H., Kürten, A., Almeida, J., Duplissy, J., Williamson, C., Ortega, I. K., Pringle,
1297 K. J., Adamov, A., Baltensperger, U., Barmet, P., Benduhn, F., Bianchi, F., Breitenlechner, M., Clarke,
1298 A., Curtius, J., Dommen, J., Donahue, N. M., Ehrhart, S., Flagan, R. C., Franchin, A., Guida, R., Hakala,
1299 J., Hansel, A., Heinritzi, M., Jokinen, T., Kangasluoma, J., Kirkby, J., Kulmala, M., Kupc, A., Lawler, M.
1300 J., Lehtipalo, K., Makhmutov, V., Mann, G., Mathot, S., Merikanto, J., Miettinen, P., Nenes, A.,
1301 Onnela, A., Rap, A., Reddington, C. L. S., Riccobono, F., Richards, N. A. D., Rissanen, M. P., Rondo, L.,
1302 Sarnela, N., Schobesberger, S., Sengupta, K., Simon, M., Sipilä, M., Smith, J. N., Stozkhov, Y., Tomé,
1303 A., Tröstl, J., Wagner, P. E., Wimmer, D., Winkler, P. M., Worsnop, D. R., and Carslaw, K. S.: Global
1304 atmospheric particle formation from CERN CLOUD measurements, *Science*, 354, 1119-1124,
1305 10.1126/science.aaf2649, 2016.
- 1306 Ekman, A. M. L., Wang, C., Strom, J., and Krejci, R.: Explicit simulation of aerosol physics in a
1307 cloud-resolving model: Aerosol transport and processing in the free troposphere, *Journal of the*
1308 *Atmospheric Sciences*, 63, 682-696, Doi 10.1175/Jas3645.1, 2006.
- 1309 Ern, M., and Preusse, P.: Gravity wave momentum flux spectra observed from satellite in the
1310 summertime subtropics: Implications for global modeling, *Geophys Res Lett*, 39,
1311 10.1029/2012gl052659, 2012.
- 1312 Frey, W., Borrmann, S., Kunkel, D., Weigel, R., de Reus, M., Schlager, H., Roiger, A., Voigt, C., Hoor,
1313 P., Curtius, J., Kramer, M., Schiller, C., Volk, C. M., Homan, C. D., Fierli, F., Di Donfrancesco, G.,
1314 Ulanovsky, A., Ravegnani, F., Sitnikov, N. M., Viciani, S., D'Amato, F., Shur, G. N., Belyaev, G. V.,
1315 Law, K. S., and Cairo, F.: In situ measurements of tropical cloud properties in the West African
1316 Monsoon: upper tropospheric ice clouds, Mesoscale Convective System outflow, and subvisual
1317 cirrus, *Atmos Chem Phys*, 11, 5569-5590, DOI 10.5194/acp-11-5569-2011, 2011.
- 1318 Froyd, K. D., Murphy, D. M., Lawson, P., Baumgardner, D., and Herman, R. L.: Aerosols that form
1319 subvisible cirrus at the tropical tropopause, *Atmos Chem Phys*, 10, 209-218, DOI 10.5194/acp-
1320 10-209-2010, 2010.
- 1321 Fujiwara, M., Sakai, T., Nagai, T., Shiraishi, K., Inai, Y., Khaykin, S., Xi, H. S., Shibata, T., Shiotani, M.,
1322 and Pan, L. L.: Lower-stratospheric aerosol measurements in eastward-shedding vortices over
1323 Japan from the Asian summer monsoon anticyclone during the summer of 2018, *Atmos Chem*
1324 *Phys*, 21, 3073-3090, 10.5194/acp-21-3073-2021, 2021.
- 1325 Garny, H., and Randel, W. J.: Transport pathways from the Asian monsoon anticyclone to the
1326 stratosphere, *Atmos. Chem. Phys.*, 16, 2703-2718, 10.5194/acp-16-2703-2016, 2016.
- 1327 Glatthor, N., Hopfner, M., Baker, I. T., Berry, J., Campbell, J. E., Kawa, S. R., Krysztofiak, G., Leyser,
1328 A., Sinnhuber, B. M., Stiller, G. P., Stinecipher, J., and von Clarmann, T.: Tropical sources and sinks
1329 of carbonyl sulfide observed from space, *Geophys Res Lett*, 42, 10082-10090,
1330 10.1002/2015gl066293, 2015.
- 1331 Hanumanthu, S., Vogel, B., Müller, R., Brunamonti, S., Fadnavis, S., Li, D., Ölsner, P., Naja, M., Singh,
1332 B. B., Kumar, K. R., Sonbawne, S., Jauhiainen, H., Vömel, H., Luo, B., Jorge, T., Wienhold, F. G.,
1333 Dirkson, R., and Peter, T.: Strong variability of the Asian Tropopause Aerosol Layer (ATAL) in
1334 August 2016 at the Himalayan foothills, *Atmos. Chem. Phys. Discuss.*, 2020, 1-42, 10.5194/acp-
1335 2020-552, 2020.
- 1336 He, Q., Ma, J., Zheng, X., Yan, X., Vömel, H., Wienhold, F. G., Gao, W., Liu, D., Shi, G., and Cheng, T.:
1337 Observational evidence of particle hygroscopic growth in the upper troposphere-lower
1338 stratosphere (UTLS) over the Tibetan Plateau, *Atmos. Chem. Phys.*, 19, 8399-8406, 10.5194/acp-
1339 19-8399-2019, 2019.

- 1340 Hermann, M., Heintzenberg, J., Wiedensohler, A., Zahn, A., Heinrich, G., and Brenninkmeijer, C. A.
 1341 M.: Meridional distributions of aerosol particle number concentrations in the upper troposphere
 1342 and lower stratosphere obtained by Civil Aircraft for Regular Investigation of the Atmosphere
 1343 Based on an Instrument Container (CARIBIC) flights, *J Geophys Res-Atmos*, 108, Artn
 1344 411410.1029/2001jd001077, 2003.
- 1345 Hersbach, H., and Dee, D. P.: ERA5 reanalysis is in production, *ECMWF Newsletter*, 147, 7, 2016.
- 1346 Hoffmann, L., Günther, G., Li, D., Stein, O., Wu, X., Griessbach, S., Heng, Y., Konopka, P., Müller, R.,
 1347 Vogel, B., and Wright, J. S.: From ERA-Interim to ERA5: the considerable impact of ECMWF's
 1348 next-generation reanalysis on Lagrangian transport simulations, *Atmos Chem Phys*, 19, 3097-
 1349 3124, 10.5194/acp-19-3097-2019, 2019.
- 1350 Höpfner, M., Ungermann, J., Borrmann, S., Wagner, R., Spang, R., Riese, M., Stiller, G., Appel, O.,
 1351 Batenburg, A. M., Bucci, S., Cairo, F., Dragoneas, A., Friedl-Vallon, F., Hünig, A., Johansson, S.,
 1352 Krasauskas, L., Legras, B., Leisner, T., Mahnke, C., Möhler, O., Molleker, S., Müller, R., Neubert, T.,
 1353 Orphal, J., Preusse, P., Rex, M., Saathoff, H., Strohm, F., Weigel, R., and Wohltmann, I.: Ammonium
 1354 nitrate particles formed in upper troposphere from ground ammonia sources during Asian
 1355 monsoons, *Nat Geosci*, 12, 608-612, 10.1038/s41561-019-0385-8, 2019.
- 1356 Jacobson, M. Z.: *Fundamentals of Atmospheric Modeling*, Cambridge University Press., New York,
 1357 813 pp., 2005.
- 1358 Jost, A., Szakáll, M., Diehl, K., Mitra, S. K., and Borrmann, S.: Chemistry of riming: the retention of
 1359 organic and inorganic atmospheric trace constituents, *Atmos. Chem. Phys.*, 17, 9717-9732,
 1360 10.5194/acp-17-9717-2017, 2017.
- 1361 Kerminen, V. M., Petaja, T., Manninen, H. E., Paasonen, P., Nieminen, T., Sipila, M., Junninen, H.,
 1362 Ehn, M., Gagne, S., Laakso, L., Riipinen, I., Vehkamäki, H., Kurten, T., Ortega, I. K., Dal Maso, M.,
 1363 Brus, D., Hyvarinen, A., Lihavainen, H., Leppä, J., Lehtinen, K. E. J., Mirme, A., Mirme, S., Horrak, U.,
 1364 Berndt, T., Stratmann, F., Birmili, W., Wiedensohler, A., Metzger, A., Dommen, J., Baltensperger,
 1365 U., Kiendler-Scharr, A., Mentel, T. F., Wildt, J., Winkler, P. M., Wagner, P. E., Petzold, A., Minikin, A.,
 1366 Plass-Dulmer, C., Poschl, U., Laaksonen, A., and Kulmala, M.: Atmospheric nucleation: highlights
 1367 of the EUCAARI project and future directions, *Atmos Chem Phys*, 10, 10829-10848,
 1368 10.5194/acp-10-10829-2010, 2010.
- 1369 Kerminen, V. M., Chen, X. M., Vakkari, V., Petäjä, T., Kulmala, M., and Bianchi, F.: Atmospheric new
 1370 particle formation and growth: review of field observations, *Environ Res Lett*, 13, Artn
 1371 10300310.1088/1748-9326/Aadf3c, 2018.
- 1372 Kirkby, J., Curtius, J., Almeida, J., Dunne, E., Duplissy, J., Ehrhart, S., Franchin, A., Gagne, S., Ickes,
 1373 L., Kurten, A., Kupc, A., Metzger, A., Riccobono, F., Rondo, L., Schobesberger, S., Tsagkogeorgas, G.,
 1374 Wimmer, D., Amorim, A., Bianchi, F., Breitenlechner, M., David, A., Dommen, J., Downard, A., Ehn,
 1375 M., Flagan, R. C., Haider, S., Hansel, A., Hauser, D., Jud, W., Junninen, H., Kreissl, F., Kvashin, A.,
 1376 Laaksonen, A., Lehtipalo, K., Lima, J., Lovejoy, E. R., Makhmutov, V., Mathot, S., Mikkilä, J.,
 1377 Minginette, P., Mogo, S., Nieminen, T., Onnela, A., Pereira, P., Petaja, T., Schnitzhofer, R., Seinfeld, J.
 1378 H., Sipila, M., Stozhkov, Y., Stratmann, F., Tome, A., Vanhanen, J., Viisanen, Y., Vrtala, A., Wagner, P.
 1379 E., Walther, H., Weingartner, E., Wex, H., Winkler, P. M., Carslaw, K. S., Worsnop, D. R.,
 1380 Baltensperger, U., and Kulmala, M.: Role of sulphuric acid, ammonia and galactic cosmic rays in
 1381 atmospheric aerosol nucleation, *Nature*, 476, 429-U477, 10.1038/nature10343, 2011.
- 1382 Konopka, P., Ploeger, F., and Müller, R.: Entropy- and static stability-based Lagrangian model
 1383 grids in: *Geophysical Monograph Series: Lagrangian Modeling of the Atmosphere*, edited by Lin,
 1384 J., 200, 99-109, <https://doi.org/10.1029/2012GM001253>, 2012.

- 1385 Kremser, S., Thomason, L. W., von Hobe, M., Hermann, M., Deshler, T., Timmreck, C., Toohey, M.,
1386 Stenke, A., Schwarz, J. P., Weigel, R., Fueglistaler, S., Prata, F. J., Vernier, J.-P., Schlager, H., Barnes,
1387 J. E., Antuña-Marrero, J.-C., Fairlie, D., Palm, M., Mahieu, E., Notholt, J., Rex, M., Bingen, C.,
1388 Vanhellemont, F., Bourassa, A., Plane, J. M. C., Klocke, D., Carn, S. A., Clarisse, L., Trickl, T., Neely,
1389 R., James, A. D., Rieger, L., Wilson, J. C., and Meland, B.: Stratospheric aerosol - Observations,
1390 processes, and impact on climate, *Rev Geophys*, 2015RG000511, 10.1002/2015rg000511, 2016.
- 1391 Kulmala, M., Vehkamäki, H., Petaja, T., Dal Maso, M., Lauri, A., Kerminen, V. M., Birmili, W., and
1392 McMurry, P. H.: Formation and growth rates of ultrafine atmospheric particles: a review of
1393 observations, *J Aerosol Sci*, 35, 143-176, 10.1016/j.jaerosci.2003.10.003, 2004.
- 1394 Kulmala, M., Kontkanen, J., Junninen, H., Lehtipalo, K., Manninen, H. E., Nieminen, T., Petaja, T.,
1395 Sipila, M., Schobesberger, S., Rantala, P., Franchin, A., Jokinen, T., Jarvinen, E., Aijala, M.,
1396 Kangasluoma, J., Hakala, J., Aalto, P. P., Paasonen, P., Mikkilä, J., Vanhanen, J., Aalto, J., Hakola, H.,
1397 Makkonen, U., Ruuskanen, T., Mauldin, R. L., Duplissy, J., Vehkamäki, H., Back, J., Kortelainen, A.,
1398 Riipinen, I., Kurten, T., Johnston, M. V., Smith, J. N., Ehn, M., Mentel, T. F., Lehtinen, K. E. J.,
1399 Laaksonen, A., Kerminen, V. M., and Worsnop, D. R.: Direct Observations of Atmospheric Aerosol
1400 Nucleation, *Science*, 339, 943-946, 10.1126/science.1227385, 2013.
- 1401 Kürten, A., Bianchi, F., Almeida, J., Kupiainen-Maatta, O., Dunne, E. M., Duplissy, J., Williamson, C.,
1402 Barmet, P., Breitenlechner, M., Dommen, J., Donahue, N. M., Flagan, R. C., Franchin, A., Gordon, H.,
1403 Hakala, J., Hansel, A., Heinritzi, M., Ickes, L., Jokinen, T., Kangasluoma, J., Kim, J., Kirkby, J., Kupc,
1404 A., Lehtipalo, K., Leiminger, M., Makhmutov, V., Onnela, A., Ortega, I. K., Petaja, T., Praplan, A. P.,
1405 Riccobono, F., Rissanen, M. P., Rondo, L., Schnitzhofer, R., Schobesberger, S., Smith, J. N., Steiner,
1406 G., Stozhkov, Y., Tome, A., Trostl, J., Tsagkogeorgas, G., Wagner, P. E., Wimmer, D., Ye, P. L.,
1407 Baltensperger, U., Carslaw, K., Kulmala, M., and Curtius, J.: Experimental particle formation rates
1408 spanning tropospheric sulfuric acid and ammonia abundances, ion production rates, and
1409 temperatures, *J Geophys Res-Atmos*, 121, 12377-12400, 10.1002/2015jd023908, 2016.
- 1410 Kürten, A., Li, C., Bianchi, F., Curtius, J., Dias, A., Donahue, N. M., Duplissy, J., Flagan, R. C., Hakala,
1411 J., Jokinen, T., Kirkby, J., Kulmala, M., Laaksonen, A., Lehtipalo, K., Makhmutov, V., Onnela, A.,
1412 Rissanen, M. P., Simon, M., Sipilä, M., Stozhkov, Y., Tröstl, J., Ye, P., and McMurry, P. H.: New
1413 particle formation in the sulfuric acid–dimethylamine–water system: reevaluation of CLOUD
1414 chamber measurements and comparison to an aerosol nucleation and growth model, *Atmos.*
1415 *Chem. Phys.*, 18, 845-863, 10.5194/acp-18-845-2018, 2018.
- 1416 Kürten, A.: New particle formation from sulfuric acid and ammonia: nucleation and growth
1417 model based on thermodynamics derived from CLOUD measurements for a wide range of
1418 conditions, *Atmos. Chem. Phys.*, 19, 5033-5050, 10.5194/acp-19-5033-2019, 2019.
- 1419 Kurtén, T., Loukonen, V., Vehkamäki, H., and Kulmala, M.: Amines are likely to enhance neutral
1420 and ion-induced sulfuric acid-water nucleation in the atmosphere more effectively than
1421 ammonia, *Atmos Chem Phys*, 8, 4095-4103, DOI 10.5194/acp-8-4095-2008, 2008.
- 1422 Lane, T. P., and Moncrieff, M. W.: Stratospheric Gravity Waves Generated by Multiscale Tropical
1423 Convection, *Journal of the Atmospheric Sciences*, 65, 2598-2614, 10.1175/2007jas2601.1, 2008.
- 1424 Lee, K. O., Dauhut, T., Chaboureaud, J. P., Khaykin, S., Kramer, M., and Rolf, C.: Convective hydration
1425 in the tropical tropopause layer during the StratoClim aircraft campaign: pathway of an
1426 observed hydration patch, *Atmos Chem Phys*, 19, 11803-11820, 10.5194/acp-19-11803-2019,
1427 2019.
- 1428 Lee, S. H., Wilson, J. C., Baumgardner, D., Herman, R. L., Weinstock, E. M., LaFleur, B. G., Kok, G.,
1429 Anderson, B., Lawson, P., Baker, B., Strawa, A., Pittman, J. V., Reeves, J. M., and Bui, T. P.: New

- 1430 particle formation observed in the tropical/subtropical cirrus clouds, *J Geophys Res-Atmos*, 109,
1431 Artn D2020910.1029/2004jd005033, 2004.
- 1432 Li, D., Vogel, B., Muller, R., Bian, J. C., Gunther, G., Ploeger, F., Li, Q., Zhang, J. Q., Bai, Z. X., Vomel, H.,
1433 and Riese, M.: Dehydration and low ozone in the tropopause layer over the Asian monsoon
1434 caused by tropical cyclones: Lagrangian transport calculations using ERA-Interim and ERA5
1435 reanalysis data, *Atmos Chem Phys*, 20, 4133-4152, 10.5194/acp-20-4133-2020, 2020.
- 1436 Mahnke, C., Weigel, R., Cairo, F., Vernier, J.-P., Afchine, A., Krämer, M., Mitev, V., Matthey, R.,
1437 Viciani, S., D'Amato, F., Ploeger, F., Deshler, T., and Borrmann, S.: The ATAL within the 2017
1438 Asian Monsoon Anticyclone: Microphysical aerosol properties derived from aircraft-borne in
1439 situ measurements, *Atmos. Chem. Phys. Discuss.*, acp-2020-1241 2021.
- 1440 McKenna, D. S., Konopka, P., Grooss, J. U., Günther, G., Müller, R., Spang, R., Offermann, D., and
1441 Orsolini, Y.: A new Chemical Lagrangian Model of the Stratosphere (CLaMS) - 1. Formulation of
1442 advection and mixing, *J Geophys Res-Atmos*, 107, Artn 430910.1029/2000jd000114, 2002.
- 1443 Merikanto, J., Spracklen, D. V., Mann, G. W., Pickering, S. J., and Carslaw, K. S.: Impact of nucleation
1444 on global CCN, *Atmos Chem Phys*, 9, 8601-8616, 10.5194/acp-9-8601-2009, 2009.
- 1445 Metzger, A., Verheggen, B., Dommen, J., Duplissy, J., Prevot, A. S. H., Weingartner, E., Riipinen, I.,
1446 Kulmala, M., Spracklen, D. V., Carslaw, K. S., and Baltensperger, U.: Evidence for the role of
1447 organics in aerosol particle formation under atmospheric conditions, *P Natl Acad Sci USA*, 107,
1448 6646-6651, 10.1073/pnas.0911330107, 2010.
- 1449 Murphy, D. M., Cziczo, D. J., Froyd, K. D., Hudson, P. K., Matthew, B. M., Middlebrook, A. M., Peltier,
1450 R. E., Sullivan, A., Thomson, D. S., and Weber, R. J.: Single-particle mass spectrometry of
1451 tropospheric aerosol particles, *J Geophys Res-Atmos*, 111, Artn D23s32Doi
1452 10.1029/2006jd007340, 2006.
- 1453 Murphy, D. M., Froyd, K. D., Schwarz, J. P., and Wilson, J. C.: Observations of the chemical
1454 composition of stratospheric aerosol particles, *Q J Roy Meteor Soc*, 140, 1269-1278,
1455 10.1002/qj.2213, 2014.
- 1456 Nieminen, T., Kerminen, V. M., Petaja, T., Aalto, P. P., Arshinov, M., Asmi, E., Baltensperger, U.,
1457 Beddows, D. C. S., Beukes, J. P., Collins, D., Ding, A. J., Harrison, R. M., Henzing, B., Hooda, R., Hu,
1458 M., Horrak, U., Kivekas, N., Komsaare, K., Krejci, R., Kristensson, A., Laakso, L., Laaksonen, A.,
1459 Leaitch, W. R., Lihavainen, H., Mihalopoulos, N., Nemeth, Z., Nie, W., O'Dowd, C., Salma, I., Sellegri,
1460 K., Svenningsson, B., Swietlicki, E., Tunved, P., Ulevicius, V., Vakkari, V., Vana, M., Wiedensohler,
1461 A., Wu, Z. J., Virtanen, A., and Kulmala, M.: Global analysis of continental boundary layer new
1462 particle formation based on long-term measurements, *Atmos Chem Phys*, 18, 14737-14756,
1463 10.5194/acp-18-14737-2018, 2018.
- 1464 Pan, L. L., Honomichl, S. B., Kinnison, D. E., Abalos, M., Randel, W. J., Bergman, J. W., and Bian, J.:
1465 Transport of chemical tracers from the boundary layer to stratosphere associated with the
1466 dynamics of the Asian summer monsoon, *Journal of Geophysical Research: Atmospheres*, 121,
1467 14.159-114.174, 10.1002/2016jd025616, 2016.
- 1468 Park, M., Randel, W. J., Gettelman, A., Massie, S. T., and Jiang, J. H.: Transport above the Asian
1469 summer monsoon anticyclone inferred from Aura Microwave Limb Sounder tracers, *J Geophys
1470 Res-Atmos*, 112, Artn D1630910.1029/2006jd008294, 2007.
- 1471 Park, M., Randel, W. J., Emmons, L. K., and Livesey, N. J.: Transport pathways of carbon monoxide
1472 in the Asian summer monsoon diagnosed from Model of Ozone and Related Tracers (MOZART), *J
1473 Geophys Res-Atmos*, 114, Artn D0830310.1029/2008jd010621, 2009.

- 1474 Piani, C., Durran, D., Alexander, M. J., and Holton, J. R.: A Numerical Study of Three-Dimensional
1475 Gravity Waves Triggered by Deep Tropical Convection and Their Role in the Dynamics of the
1476 QBO, *Journal of the Atmospheric Sciences*, 57, 3689-3702, 10.1175/1520-
1477 0469(2000)057<3689:Ansotd>2.0.Co;2, 2000.
- 1478 Pissò, I., and Legras, B.: Turbulent vertical diffusivity in the sub-tropical stratosphere, *Atmos.*
1479 *Chem. Phys.*, 8, 697-707, 10.5194/acp-8-697-2008, 2008.
- 1480 Ploeger, F., Günther, G., Konopka, P., Fueglistaler, S., Müller, R., Hoppe, C., Kunz, A., Spang, R.,
1481 Grooss, J. U., and Riese, M.: Horizontal water vapor transport in the lower stratosphere from
1482 subtropics to high latitudes during boreal summer, *J Geophys Res-Atmos*, 118, 8111-8127,
1483 10.1002/jgrd.50636, 2013.
- 1484 Ploeger, F., Gottschling, C., Griessbach, S., Grooss, J. U., Günther, G., Konopka, P., Müller, R., Riese,
1485 M., Stroh, F., Tao, M., Ungermann, J., Vogel, B., and von Hobe, M.: A potential vorticity-based
1486 determination of the transport barrier in the Asian summer monsoon anticyclone, *Atmos Chem*
1487 *Phys*, 15, 13145-13159, 10.5194/acp-15-13145-2015, 2015.
- 1488 Ploeger, F., Konopka, P., Walker, K., and Riese, M.: Quantifying pollution transport from the Asian
1489 monsoon anticyclone into the lower stratosphere, *Atmos Chem Phys*, 17, 7055-7066,
1490 10.5194/acp-17-7055-2017, 2017.
- 1491 Ploeger, F., Diallo, M., Charlesworth, E., Konopka, P., Legras, B., Laube, J. C., Groß, J. U., Günther,
1492 G., Engel, A., and Riese, M.: The stratospheric Brewer–Dobson circulation inferred from age of air
1493 in the ERA5 reanalysis, *Atmos. Chem. Phys. Discuss.*, 2021, 1-27, 10.5194/acp-2020-1253, 2021.
- 1494 Pommrich, R., Müller, R., Grooss, J. U., Konopka, P., Ploeger, F., Vogel, B., Tao, M., Hoppe, C. M.,
1495 Günther, G., Spelten, N., Hoffmann, L., Pumphrey, H. C., Viciani, S., D'Amato, F., Volk, C. M., Hoor,
1496 P., Schlager, H., and Riese, M.: Tropical troposphere to stratosphere transport of carbon
1497 monoxide and long-lived trace species in the Chemical Lagrangian Model of the Stratosphere
1498 (CLaMS), *Geosci Model Dev*, 7, 2895-2916, 10.5194/gmd-7-2895-2014, 2014.
- 1499 Randel, W. J., and Park, M.: Deep convective influence on the Asian summer monsoon anticyclone
1500 and associated tracer variability observed with Atmospheric Infrared Sounder (AIRS), *J Geophys*
1501 *Res-Atmos*, 111, Artn D1231410.1029/2005jd006490, 2006.
- 1502 Riccobono, F., Schobesberger, S., Scott, C. E., Dommen, J., Ortega, I. K., Rondo, L., Almeida, J.,
1503 Amorim, A., Bianchi, F., Breitenlechner, M., David, A., Downard, A., Dunne, E. M., Duplissy, J.,
1504 Ehrhart, S., Flagan, R. C., Franchin, A., Hansel, A., Junninen, H., Kajos, M., Keskinen, H., Kupc, A.,
1505 Kürten, A., Kvashin, A. N., Laaksonen, A., Lehtipalo, K., Makhmutov, V., Mathot, S., Nieminen, T.,
1506 Onnela, A., Petaja, T., Praplan, A. P., Santos, F. D., Schallhart, S., Seinfeld, J. H., Sipila, M., Spracklen,
1507 D. V., Stozhkov, Y., Stratmann, F., Tome, A., Tsagkogeorgas, G., Vaattovaara, P., Viisanen, Y., Vrtala,
1508 A., Wagner, P. E., Weingartner, E., Wex, H., Wimmer, D., Carslaw, K. S., Curtius, J., Donahue, N. M.,
1509 Kirkby, J., Kulmala, M., Worsnop, D. R., and Baltensperger, U.: Oxidation Products of Biogenic
1510 Emissions Contribute to Nucleation of Atmospheric Particles, *Science*, 344, 717-721,
1511 10.1126/science.1243527, 2014.
- 1512 Rollins, A. W., Thornberry, T. D., Watts, L. A., Yu, P., Rosenlof, K. H., Mills, M., Baumann, E.,
1513 Giorgetta, F. R., Bui, T. V., Hopfner, M., Walker, K. A., Boone, C., Bernath, P. F., Colarco, P. R.,
1514 Newman, P. A., Fahey, D. W., and Gao, R. S.: The role of sulfur dioxide in stratospheric aerosol
1515 formation evaluated by using in situ measurements in the tropical lower stratosphere, *Geophys*
1516 *Res Lett*, 44, 4280-4286, 10.1002/2017gl072754, 2017.
- 1517 Rosen, J. M.: The Boiling Point of Stratospheric Aerosols, *J Appl Meteorol*, 10, 1044-1046,
1518 10.1175/1520-0450(1971)010<1044:tbposa>2.0.co;2, 1971.

- 1519 Sahyoun, M., Freney, E., Brito, J., Duplissy, J., Gouhier, M., Colomb, A., Dupuy, R., Bourianne, T.,
1520 Nowak, J. B., Yan, C., Petäjä, T., Kulmala, M., Schwarzenboeck, A., Planche, C., and Sellegri, K.:
1521 Evidence of New Particle Formation Within Etna and Stromboli Volcanic Plumes and Its
1522 Parameterization From Airborne In Situ Measurements, *Journal of Geophysical Research:*
1523 *Atmospheres*, 124, 5650-5668, 10.1029/2018jd028882, 2019.
- 1524 Santee, M. L., Manney, G. L., Livesey, N. J., Schwartz, M. J., Neu, J. L., and Read, W. G.: A
1525 comprehensive overview of the climatological composition of the Asian summermonsoon
1526 anticyclone based on 10 years of Aura Microwave Limb Sounder measurements, *J Geophys Res-*
1527 *Atmos*, 122, 5491-5514, 10.1002/2016jd026408, 2017.
- 1528 Schneider, J., Weigel, R., Klimach, T., Dragoneas, A., Appel, O., Hünig, A., Molleker, S., Köllner, F.,
1529 Clemen, H.-C., Eppers, O., Hoppe, P., Hoor, P., Mahnke, C., Krämer, M., Rolf, C., Grooß, J.-U., Zahn,
1530 A., Obersteiner, F., Ravegnani, F., Ulanovsky, A., Schlager, H., Scheibe, M., Diskin, G. S., DiGangi, J.
1531 P., Nowak, J. B., Zöger, M., and Borrmann, S.: Aircraft-based observation of meteoric material in
1532 lower stratospheric aerosol particles between 15 and 68° N, *Atmos. Chem. Phys. Discuss.*, in
1533 review, <https://doi.org/10.5194/acp-2020-660>, 2020.
- 1534 Sellegri, K., Rose, C., Marinoni, A., Lupi, A., Wiedensohler, A., Andrade, M., Bonasoni, P., and Laj, P.:
1535 New Particle Formation: A Review of Ground-Based Observations at Mountain Research
1536 Stations, *Atmosphere-Basel*, 10, Artn 49310.3390/Atmos10090493, 2019.
- 1537 Sokolov, L., and Lepuchov, B.: Protocol of interaction between Unit for Connection with Scientific
1538 Equipment (UCSE) and on-board scientific equipment of Geophysica aircraft (Second edition),
1539 Myasishchev Design Bureau (MDB), 1998.
- 1540 Song, I.-S., Chun, H.-Y., and Lane, T. P.: Generation Mechanisms of Convectively Forced Internal
1541 Gravity Waves and Their Propagation to the Stratosphere, *Journal of the Atmospheric Sciences*,
1542 60, 1960-1980, 10.1175/1520-0469(2003)060<1960:Gmoci>2.0.Co;2, 2003.
- 1543 Stenke, A., Schraner, M., Rozanov, E., Egorova, T., Luo, B., and Peter, T.: The SOCOL version 3.0
1544 chemistry-climate model: description, evaluation, and implications from an advanced transport
1545 algorithm, *Geosci Model Dev*, 6, 1407-1427, 10.5194/gmd-6-1407-2013, 2013.
- 1546 Stohl, A., Forster, C., Frank, A., Seibert, P., and Wotawa, G.: Technical note: The Lagrangian
1547 particle dispersion model FLEXPART version 6.2, *Atmos. Chem. Phys.*, 5, 2461-2474,
1548 10.5194/acp-5-2461-2005, 2005.
- 1549 Stolzenburg, D., Simon, M., Ranjithkumar, A., Kürten, A., Lehtipalo, K., Gordon, H., Ehrhart, S.,
1550 Finkenzeller, H., Pichelstorfer, L., Nieminen, T., He, X. C., Brilke, S., Xiao, M., Amorim, A., Baalbaki,
1551 R., Baccarini, A., Beck, L., Bräkling, S., Caudillo Murillo, L., Chen, D., Chu, B., Dada, L., Dias, A.,
1552 Dommen, J., Duplissy, J., El Haddad, I., Fischer, L., Gonzalez Carracedo, L., Heinritzi, M., Kim, C.,
1553 Koenig, T. K., Kong, W., Lamkaddam, H., Lee, C. P., Leiminger, M., Li, Z., Makhmutov, V., Manninen,
1554 H. E., Marie, G., Marten, R., Müller, T., Nie, W., Partoll, E., Petäjä, T., Pfeifer, J., Philippov, M.,
1555 Rissanen, M. P., Rörup, B., Schobesberger, S., Schuchmann, S., Shen, J., Sipilä, M., Steiner, G.,
1556 Stozhkov, Y., Tauber, C., Tham, Y. J., Tomé, A., Vazquez-Pufleau, M., Wagner, A. C., Wang, M.,
1557 Wang, Y., Weber, S. K., Wimmer, D., Wlasits, P. J., Wu, Y., Ye, Q., Zauner-Wieczorek, M.,
1558 Baltensperger, U., Carslaw, K. S., Curtius, J., Donahue, N. M., Flagan, R. C., Hansel, A., Kulmala, M.,
1559 Lelieveld, J., Volkamer, R., Kirkby, J., and Winkler, P. M.: Enhanced growth rate of atmospheric
1560 particles from sulfuric acid, *Atmos. Chem. Phys.*, 20, 7359-7372, 10.5194/acp-20-7359-2020,
1561 2020.
- 1562

- 1563 Stroh, F., and the StratoClim group: First detailed airborne and balloon measurements of
 1564 microphysical, dynamical, and chemical processes in the Asian Summer Monsoon Anticyclone:
 1565 Overview and First Results of the 2016/2017 StratoClim field campaigns., in preparation for
 1566 submission to Atmos. Chem. Phys., 2021.
- 1567 Tang, M. J., Cox, R. A., and Kalberer, M.: Compilation and evaluation of gas phase diffusion
 1568 coefficients of reactive trace gases in the atmosphere: volume 1. Inorganic compounds, Atmos.
 1569 Chem. Phys., 14, 9233-9247, 10.5194/acp-14-9233-2014, 2014.
- 1570 Thomason, L., and Peter, T.: SPARC assessment of stratospheric aerosol properties, WCRP-124,
 1571 WMO/TD-No. 1295, SPARC Report, 2006.
- 1572 Thomason, L. W., and Vernier, J. P.: Improved SAGE II cloud/aerosol categorization and
 1573 observations of the Asian tropopause aerosol layer: 1989-2005, Atmos Chem Phys, 13, 4605-
 1574 4616, 10.5194/acp-13-4605-2013, 2013.
- 1575 Tissier, A. S., and Legras, B.: Convective sources of trajectories traversing the
 1576 tropical tropopause layer, Atmos. Chem. Phys., 16, 3383-3398, 10.5194/acp-16-3383-2016,
 1577 2016.
- 1578 Tzella, A., and Legras, B.: A Lagrangian view of convective sources for transport of air across the
 1579 Tropical Tropopause Layer: distribution, times and the radiative influence of clouds, Atmos.
 1580 Chem. Phys., 11, 12517-12534, 10.5194/acp-11-12517-2011, 2011.
- 1581 Venzac, H., Sellegrì, K., Laj, P., Villani, P., Bonasoni, P., Marinoni, A., Cristofanelli, P., Calzolari, F.,
 1582 Fuzzi, S., Decesari, S., Facchini, M. C., Vuillermoz, E., and Verza, G. P.: High frequency new particle
 1583 formation in the Himalayas, P Natl Acad Sci USA, 105, 15666-15671, 10.1073/pnas.0801355105,
 1584 2008.
- 1585 Vernier, J.-P., Fairlie, T. D., Deshler, T., Ratnam, M. V., Gadhavi, H., Kumar, B. S., Natarajan, M.,
 1586 Pandit, A. K., Raj, S. T. A., Kumar, A. H., Jayaraman, A., Singh, A. K., Rastogi, N., Sinha, P. R., Kumar,
 1587 S., Tiwari, S., Wegner, T., Baker, N., Vignelles, D., Stenchikov, G., Shevchenko, I., Smith, J., Bedka,
 1588 K., Kesarkar, A., Singh, V., Bhate, J., Ravikiran, V., Rao, M. D., Ravindrababu, S., Patel, A., Vernier,
 1589 H., Wienhold, F. G., Liu, H., Knepp, T. N., Thomason, L., Crawford, J., Ziemba, L., Moore, J.,
 1590 Crumeyrolle, S., Williamson, M., Berthet, G., Jégou, F., and Renard, J.-B.: BATAL: The Balloon
 1591 Measurement Campaigns of the Asian Tropopause Aerosol Layer, B Am Meteorol Soc, 99, 955-
 1592 973, 10.1175/bams-d-17-0014.1, 2018.
- 1593 Vernier, J. P., Thomason, L. W., and Kar, J.: CALIPSO detection of an Asian tropopause aerosol
 1594 layer, Geophys Res Lett, 38, Artn L0780410.1029/2010gl046614, 2011a.
- 1595 Vernier, J. P., Thomason, L. W., Pommereau, J. P., Bourassa, A., Pelon, J., Garnier, A., Hauchecorne,
 1596 A., Blanot, L., Trepte, C., Degenstein, D., and Vargas, F.: Major influence of tropical volcanic
 1597 eruptions on the stratospheric aerosol layer during the last decade, Geophys Res Lett, 38, Artn
 1598 L12807Doi 10.1029/2011gl047563, 2011b.
- 1599 Vernier, J. P., Fairlie, T. D., Natarajan, M., Wienhold, F. G., Bian, J., Martinsson, B. G., Crumeyrolle,
 1600 S., Thomason, L. W., and Bedka, K. M.: Increase in upper tropospheric and lower stratospheric
 1601 aerosol levels and its potential connection with Asian pollution, J Geophys Res-Atmos, 120,
 1602 1608-1619, 10.1002/2014jd022372, 2015.
- 1603 Viciani, S., D'Amato, F., Mazzinghi, P., Castagnoli, F., Toci, G., and Werle, P.: A cryogenically
 1604 operated laser diode spectrometer for airborne measurement of stratospheric trace gases,
 1605 Applied Physics B, 90, 581-592, 10.1007/s00340-007-2885-2, 2008.

- 1606 Viciani, S., Montori, A., Chiarugi, A., and D'Amato, F.: A Portable Quantum Cascade Laser
1607 Spectrometer for Atmospheric Measurements of Carbon Monoxide, *Sensors*, 18, 2380,
1608 doi:10.3390/s18072380, 2018.
- 1609 Vincent, R. A., and Alexander, M. J.: Gravity waves in the tropical lower stratosphere: An
1610 observational study of seasonal and interannual variability, *Journal of Geophysical Research:*
1611 *Atmospheres*, 105, 17971-17982, 10.1029/2000jd900196, 2000.
- 1612 Vogel, B., Günther, G., Müller, R., Grooss, J. U., Hoor, P., Krämer, M., Müller, S., Zahn, A., and Riese,
1613 M.: Fast transport from Southeast Asia boundary layer sources to northern Europe: rapid uplift
1614 in typhoons and eastward eddy shedding of the Asian monsoon anticyclone, *Atmos Chem Phys*,
1615 14, 12745-12762, 10.5194/acp-14-12745-2014, 2014.
- 1616 Vogel, B., Müller, R., Günther, G., Spang, R., Hanumanthu, S., Li, D., Riese, M., and Stiller, G. P.:
1617 Lagrangian simulations of the transport of young air masses to the top of the Asian monsoon
1618 anticyclone and into the tropical pipe, *Atmos Chem Phys*, 19, 6007-6034, 10.5194/acp-19-6007-
1619 2019, 2019.
- 1620 von der Weiden, S. L., Drewnick, F., and Borrmann, S.: Particle Loss Calculator - a new software
1621 tool for the assessment of the performance of aerosol inlet systems, *Atmos Meas Tech*, 2, 479-
1622 494, DOI 10.5194/amt-2-479-2009, 2009.
- 1623 von Hobe, M., Ploeger, F., Konopka, P., Kloss, C., Ulanowski, A., Yushkov, V., Ravegnani, F., Volk, C.
1624 M., Pan, L. L., Homomichl, S. B., Tilmes, S., Kinnison, D. E., Garcia, R. R., and Wright, J. S.: Upward
1625 transport into and within the Asian monsoon anticyclone as inferred from StratoClim trace gas
1626 observations, *Atmos. Chem. Phys. Discuss.*, 2020, 1-31, 10.5194/acp-2020-891, 2020.
- 1627 Wang, M., Kong, W., Marten, R., He, X.-C., Chen, D., Pfeifer, J., Heitto, A., Kontkanen, J., Dada, L.,
1628 Kürten, A., Yli-Juuti, T., Manninen, H. E., Amanatidis, S., Amorim, A., Baalbaki, R., Baccarini, A.,
1629 Bell, D. M., Bertozzi, B., Bräkling, S., Brilke, S., Murillo, L. C., Chiu, R., Chu, B., De Menezes, L.-P.,
1630 Duplissy, J., Finkenzeller, H., Carracedo, L. G., Granzin, M., Guida, R., Hansel, A., Hofbauer, V.,
1631 Krechmer, J., Lehtipalo, K., Lamkaddam, H., Lampimäki, M., Lee, C. P., Makhmutov, V., Marie, G.,
1632 Mathot, S., Mauldin, R. L., Mentler, B., Müller, T., Onnela, A., Partoll, E., Petäjä, T., Philippov, M.,
1633 Pospisilova, V., Ranjithkumar, A., Rissanen, M., Rörup, B., Scholz, W., Shen, J., Simon, M., Sipilä, M.,
1634 Steiner, G., Stolzenburg, D., Tham, Y. J., Tomé, A., Wagner, A. C., Wang, D. S., Wang, Y., Weber, S. K.,
1635 Winkler, P. M., Wlasits, P. J., Wu, Y., Xiao, M., Ye, Q., Zauner-Wieczorek, M., Zhou, X., Volkamer, R.,
1636 Riipinen, I., Dommen, J., Curtius, J., Baltensperger, U., Kulmala, M., Worsnop, D. R., Kirkby, J.,
1637 Seinfeld, J. H., El-Haddad, I., Flagan, R. C., and Donahue, N. M.: Rapid growth of new atmospheric
1638 particles by nitric acid and ammonia condensation, *Nature*, 581, 184-189, 10.1038/s41586-020-
1639 2270-4, 2020.
- 1640 Wehner, B., Werner, F., Ditas, F., Shaw, R. A., Kulmala, M., and Siebert, H.: Observations of new
1641 particle formation in enhanced UV irradiance zones near cumulus clouds, *Atmos Chem Phys*, 15,
1642 11701-11711, 10.5194/acp-15-11701-2015, 2015.
- 1643 Weigel, R., Hermann, M., Curtius, J., Voigt, C., Walter, S., Bottger, T., Lepukhov, B., Belyaev, G., and
1644 Borrmann, S.: Experimental characterization of the CONDensation PARTICLE counting System for
1645 high altitude aircraft-borne application, *Atmos Meas Tech*, 2, 243-258, 10.5194/amt-2-243-
1646 2009, 2009.
- 1647 Weigel, R., Borrmann, S., Kazil, J., Minikin, A., Stohl, A., Wilson, J. C., Reeves, J. M., Kunkel, D., de
1648 Reus, M., Frey, W., Lovejoy, E. R., Volk, C. M., Viciani, S., D'Amato, F., Schiller, C., Peter, T., Schlager,
1649 H., Cairo, F., Law, K. S., Shur, G. N., Belyaev, G. V., and Curtius, J.: In situ observations of new
1650 particle formation in the tropical upper troposphere: the role of clouds and the nucleation
1651 mechanism, *Atmos Chem Phys*, 11, 9983-10010, 10.5194/acp-11-9983-2011, 2011.

- 1652 Weigel, R., Volk, C. M., Kandler, K., Hosen, E., Gunther, G., Vogel, B., Grooss, J. U., Khaykin, S.,
 1653 Belyaev, G. V., and Borrmann, S.: Enhancements of the refractory submicron aerosol fraction in
 1654 the Arctic polar vortex: feature or exception?, *Atmos Chem Phys*, 14, 12319-12342, DOI
 1655 10.5194/acp-14-12319-2014, 2014.
- 1656 Weigel, R., Mahnke, C., Baumgartner, M., Krämer, M., Spichtinger, P., Spelten, N., Afchine, A., Rolf,
 1657 C., Viciani, S., D'Amato, F., Tost, H., Belyaev, G. V., and Borrmann, S.: In-Situ observation of New
 1658 Particle Formation (NPF) in the tropical tropopause layer of the 2017 Asian Monsoon
 1659 Anticyclone: Part II - NPF inside ice clouds, *Atmos. Chem. Phys. Discuss.*, acp-2020-1285, 2021b.
- 1660 Weigelt, A., Hermann, M., van Velthoven, P. F. J., Brenninkmeijer, C. A. M., Schlaf, G., Zahn, A., and
 1661 Wiedensohler, A.: Influence of clouds on aerosol particle number concentrations in the upper
 1662 troposphere, *J Geophys Res-Atmos*, 114, Artn D0120410.1029/2008jd009805, 2009.
- 1663 Williamson, C., Kupc, A., Wilson, J., Gesler, D. W., Reeves, J. M., Erdesz, F., McLaughlin, R., and
 1664 Brock, C. A.: Fast time response measurements of particle size distributions in the 3-60 nm size
 1665 range with the nucleation mode aerosol size spectrometer, *Atmos Meas Tech*, 11, 3491-3509,
 1666 10.5194/amt-11-3491-2018, 2018.
- 1667 Williamson, C. J., Kupc, A., Axisa, D., Bilsback, K. R., Bui, T., Campuzano-Jost, P., Dollner, M., Froyd,
 1668 K. D., Hodshire, A. L., Jimenez, J. L., Kodros, J. K., Luo, G., Murphy, D. M., Nault, B. A., Ray, E. A.,
 1669 Weinzierl, B., Wilson, J. C., Yu, F., Yu, P., Pierce, J. R., and Brock, C. A.: A large source of cloud
 1670 condensation nuclei from new particle formation in the tropics, *Nature*, 574, 399-403,
 1671 10.1038/s41586-019-1638-9, 2019.
- 1672 WMO: Meteorology -- A three-dimensional science, *WMO Bull*, 134--138, 1957.
- 1673 WMO: International Meteorological Tables, WMO-No.188.TP97, edited by: Letestu, S., Secretariat
 1674 of the World Meteorological Organization, Geneva, Switzerland, 1966.
- 1675 Wright, C. J., and Gille, J. C.: HIRDLS observations of gravity wave momentum fluxes over the
 1676 monsoon regions, *Journal of Geophysical Research: Atmospheres*, 116, 10.1029/2011jd015725,
 1677 2011.
- 1678 Yu, F. Q., Luo, G., Bates, T. S., Anderson, B., Clarke, A., Kapustin, V., Yantosca, R. M., Wang, Y. X., and
 1679 Wu, S. L.: Spatial distributions of particle number concentrations in the global troposphere:
 1680 Simulations, observations, and implications for nucleation mechanisms, *J Geophys Res-Atmos*,
 1681 115, Artn D1720510.1029/2009jd013473, 2010.
- 1682 Yu, P., Rosenlof, K. H., Liu, S., Telg, H., Thornberry, T. D., Rollins, A. W., Portmann, R. W., Bai, Z.,
 1683 Ray, E. A., Duan, Y., Pan, L. L., Toon, O. B., Bian, J., and Gao, R.-S.: Efficient transport of
 1684 tropospheric aerosol into the stratosphere via the Asian summer monsoon anticyclone,
 1685 *Proceedings of the National Academy of Sciences*, 114, 6972-6977, 10.1073/pnas.1701170114,
 1686 2017.
- 1687 Yu, P. F., Toon, O. B., Neely, R. R., Martinsson, B. G., and Brenninkmeijer, C. A. M.: Composition and
 1688 physical properties of the Asian Tropopause Aerosol Layer and the North American
 1689 Tropospheric Aerosol Layer, *Geophys Res Lett*, 42, 2540-2546, 10.1002/2015gl063181, 2015.
- 1690 Zhang, Y., McMurry, P. H., Yu, F. Q., and Jacobson, M. Z.: A comparative study of nucleation
 1691 parameterizations: 1. Examination and evaluation of the formulations, *J Geophys Res-Atmos*,
 1692 115, Artn D2021210.1029/2010jd014150, 2010.
- 1693

1694 **Figure captions**

1695 Figure 1: (a) Flight patterns of the StratoClim 2017 mission over Nepal, India, Bangladesh, and
1696 the Bay of Bengal. (b) Regions with elevated number concentrations of nucleation-mode
1697 particles (N_{nm} , ambient conditions) of sizes in the diameter range $6 \text{ nm} < d_p < 15 \text{ nm}$ from COPAS
1698 measurements are indicated by the colour-code and by symbol size along the flight tracks.

1699 Figure 2: Synopsis of vertical profiles of the total number concentration (median with 10th, 25th,
1700 75th, 90th, and 99th percentiles) of sub-micrometre sized particles as a function of potential
1701 temperature obtained from condensation nuclei (CN) detections over (a) Brazil (TROCCINOX,
1702 2005), over (b) West Africa (SCOUT-AMMA, 2006) and over (c) the Indian subcontinent
1703 (StratoClim 2017). During TROCCINOX (a) and SCOUT-AMMA (b) the number concentrations N_4
1704 at lower heights ($\theta < 350 \text{ K}$) were measured aboard the DLR Falcon (cf. Borrmann et al. (2010)
1705 and Weigel et al. (2011)). All high-altitude measurements ($\theta > 350 \text{ K}$) from the M-55 *Geophysica*
1706 and the entire StratoClim 2017 data set result from COPAS measurements. (c) The median
1707 profile of $N_{5.3}$ from repeated measurements (over the years 2004 – 2007) with the NMASS multi-
1708 channel CN counter over Central America (aboard the NASA WB-57F, data courtesy of J. C.
1709 Wilson, Denver University, 2011). All number concentrations are given at ambient conditions.

1710 Figure 3: (a) 1 Hz-resolved particle mixing ratios n_6 and n_{10} (grey-shaded COPAS data points)
1711 with n_6 median profile from StratoClim 2017 together with COPAS data from other tropical
1712 regions (over Brazil, TROCCINOX 2005 and over West Africa, SCOUT-AMMA 2006, cf. (Borrmann
1713 et al., 2010)). The median profile of measurements in the tropics over the Americas (Brock et al.,
1714 1995) is coloured in green. (b) The vertical distribution of the mixing ratio of nucleation-mode
1715 particle ($n_{nm} = n_{6-15}$) in compliance with the NPF criterion (cf. Section 0). (c) The 1 Hz-resolved
1716 mixing ratio of non-volatile particles (i.e. thermostable at $\sim 270^\circ\text{C}$) from COPAS measurements
1717 throughout StratoClim 2017 with corresponding median profile, including 25th and 75th
1718 percentile. Herein, the n_6 median profile is implied from Panel a for comparison. (d) The fraction
1719 $f(= n_{10nv}/n_{10} \cdot 100)$ of non-volatile particles with median, and with 25th and 75th percentiles.

1720 Figure 4: Frequency of the duration of observed NPF events during the StratoClim 2017 mission.
1721 (a) as frequency distribution of the NPF duration, (b) as vertical profile as a function of mean
1722 potential temperature and coloured with reference to the mean mixing ratio $\overline{n_{nm}}$ of the
1723 nucleation-mode particles.

1724 Figure 5: (a) Diurnal variation of the occurrence frequency of NPF events. (b) The diurnal
1725 distribution of NPF events' mean particle mixing ratio $\overline{n_{nm}}$ with standard deviation σ , coloured
1726 by flight date, and (c) in colours of the (logarithmic) duration of respective event. Note, the mean
1727 horizontal distance is derived from the event duration based on a mean flight speed of 154 m s^{-1}
1728 ($\sigma = \pm 39 \text{ m s}^{-1}$, variable flight attitude remains unconsidered) and is understood as equivalent
1729 horizontal extension of a NPF event.

1730 Figure 6: Mean particle mixing ratio $\overline{n_{nm}}$ of individual NPF events as function of (left column) the
1731 vertical distance from the mean lapse-rate tropopause ($\overline{\Delta\theta}$), and of (right column) the equivalent
1732 latitude (90° represents the centre of the AMA as projected to polar coordinates). Data points
1733 are coloured by flight date (Panels a and b) and by CO mixing ratios (Panels c and d). (e) The
1734 mean particle mixing ratio $\overline{n_{nm}}$ as function of the equivalent latitude is colour-coded by the
1735 values $\overline{\Delta\theta}$ (colour scale on the left of panel (e)).

1736

1737 Figure 7: Results of a coagulation simulation based on the assumption of a distinct and expired
1738 burst-like event. The simulation's initial particle size distribution (black circles; horizontal bars
1739 indicate the width of each size bin) is merged from data of three COPAS detectors (for N_6 , N_{10} ,
1740 and N_{15}) and of the UHSAS-A ($65 \text{ nm} < d_p < 1 \mu\text{m}$) as detected during NPF encountered on 04
1741 August 2017, between 04:04:40 and 04:05:06 UTC. (a): The processing particle size distribution
1742 (coloured lines) over several hours. (b): The concentration of nucleation-mode particles (N_{nm})
1743 over the simulation's run time and its fractional contribution to the total particle number
1744 concentration (N_{total}). Furthermore, the simulated decay of variably multiplied N_{nm} (by factors
1745 0.1, 10, and 100) as initial input of the simulation under constant background conditions
1746 (dashed lines).

1747 Figure 8: Particle mixing ratio of fine-mode particles n_6 (grey dots in the background) and of
1748 nucleation-mode particles n_{nm} (colour-coded with reference to the potential temperature) in
1749 relationship to the CO mixing ratio. The median n_{nm} with the 25th and 75th percentile is shown in
1750 bin widths of $2.5 \text{ nmol mol}^{-1}$ of the CO mixing ratio (black dots).

1751 Figure 9: From backward trajectory analyses by means of the chemistry transport model ClAMS
1752 and based on ERA-5 data in Panel a) the geographic position of the last boundary layer (BL)
1753 contact of the NPF-connected air mass backward trajectories, in Panel b) the geographic position
1754 of the maximum ascent rate. Subpanels a.1 and a.2 (b.1 and b.2) provide 2-level zoom-ins of the
1755 respective main Panel a) or b) based on the same data set. The backward trajectories were
1756 analysed over the last 50 days prior to the NPF detection as starting point of each trajectory.
1757 Here, the data points are coloured with reference to the (logarithmic) mixing ratio n_{nm} of
1758 nucleation-mode particles, grey data points indicate transport times > 25 days.

1759 Figure 10: structured as in Figure 9, in Panel a) the last boundary layer (BL) contact of the NPF-
1760 connected air mass backward trajectories and in Panel b) the maximum ascent rate of these
1761 trajectories (for details of the trajectory analyses with ClAMS, cf. Figure 9). Here, the data points
1762 are coloured to the air mass transport time since the last BL contact, grey data points indicate
1763 transport times > 25 days.

1764 Figure 11: Vertical profile of the 1 Hz-resolved particle mixing ratio of nucleation-mode particles
1765 n_{nm} colour-coded by the air mass transport time (days) from the boundary layer (BL). For details
1766 of ClAMS analyses, cf. Figure 9 and Figure 10.

1767 Figure 12: Vertical profile of the event-wise mean particle mixing ratio of nucleation-mode
1768 particles $\overline{n_{\text{nm}}}$ with standard deviation σ (bars) as a function of the mean potential temperature
1769 ($\pm \sigma$). (a) The data points are colour-coded by the proportion of convective contribution to the
1770 air sample. (b) The data points are coloured by the time (days) since the release of the air mass
1771 at the top of a convective cell.

1772 Figure 13: Time series of data sampled during a section of a StratoClim 2017 flight (KTM 6) on
1773 06 August 2017. Except the manoeuvre period between 09:20 and 09:30 (UTC), a constant
1774 altitude and pressure level (Panel a) were maintained. Particle mixing ratios n_6 , n_{10} and n_{15} and
1775 $n_{10}\text{nv}$ (Panel b), the mixing ratio of the nucleation-mode particles n_{nm} (Panel c), the CO mixing
1776 ratio (Panel d), the ambient air temperature (T_{amb}), and the temperature fluctuation ($T_{\text{amb}} - T_{\text{mean}}$)
1777 (Panel e) feature different characteristics and sequence during two NPF phases (oblique hatched
1778 areas).

1779 Figure 14: Close-up view of the two sections of StratoClim 2017 flight (KTM 6) on
1780 06 August 2017 over time ranges of more than 1 hour of flight time, respectively, including the

1781 two identified NPF periods (horizontal bar in panels a and b). For analysing the observed
1782 temperature anomaly, the 1 Hz-resolved temperature data are filtered by the noise-reducing
1783 running average over 201 data points (T_{201}). The wave fit (T_{Fit}) is approximated to the noise-
1784 filtered data set within the period of identified NPF (cf. Appendix B for details). The overlaid fit
1785 function approximates the characteristic structure of the observed temperature anomaly only
1786 within the two NPF periods.

1787

1788

1789 Figure A- 1: For the time intervals shown in Figure 14: the difference between the 1 Hz-data
1790 ($T_{1\text{Hz}}$) and the filtered data with 201-seconds running average (T_{201}) reveals the high-frequency
1791 noise of the temperature measurement (red data points). The dashed reference lines indicate
1792 the standard deviation ($\pm 1 \sigma$ and $\pm 3 \sigma$) of the noise signal within given time intervals. The
1793 effectiveness of the wave fit approximation to the filtered data set during the NPF periods is
1794 represented by the difference $T_{201}-T_{\text{Fit}}$. During NPF this deviation is small while away from NPF
1795 the wave fit increasingly deviates from the temperature measurement. The deviation of the
1796 overlaid wave fit from the untreated 1 Hz signal is shown with the differences $T_{1\text{Hz}}-T_{\text{Fit}}$: during
1797 NPF mainly the noise signal remains.

1798 Figure A- 2: Simulated influence of temperature anomalies (up to ~ 4 K) on the quotient of
1799 saturation ratios S/S_0 of pure sulphuric acid (H_2SO_4) in reference to any initial saturation ratio S_0
1800 (including supersaturation), over a range of initial air temperatures at which NPF was observed
1801 during StratoClim 2017.

1802

1803 **Figures**

1804

1805

1806

1807

1808

1809

1810

1811

1812

1813

1814

1815

1816

1817

1818

1819

1820

1821

1822

1823

1824

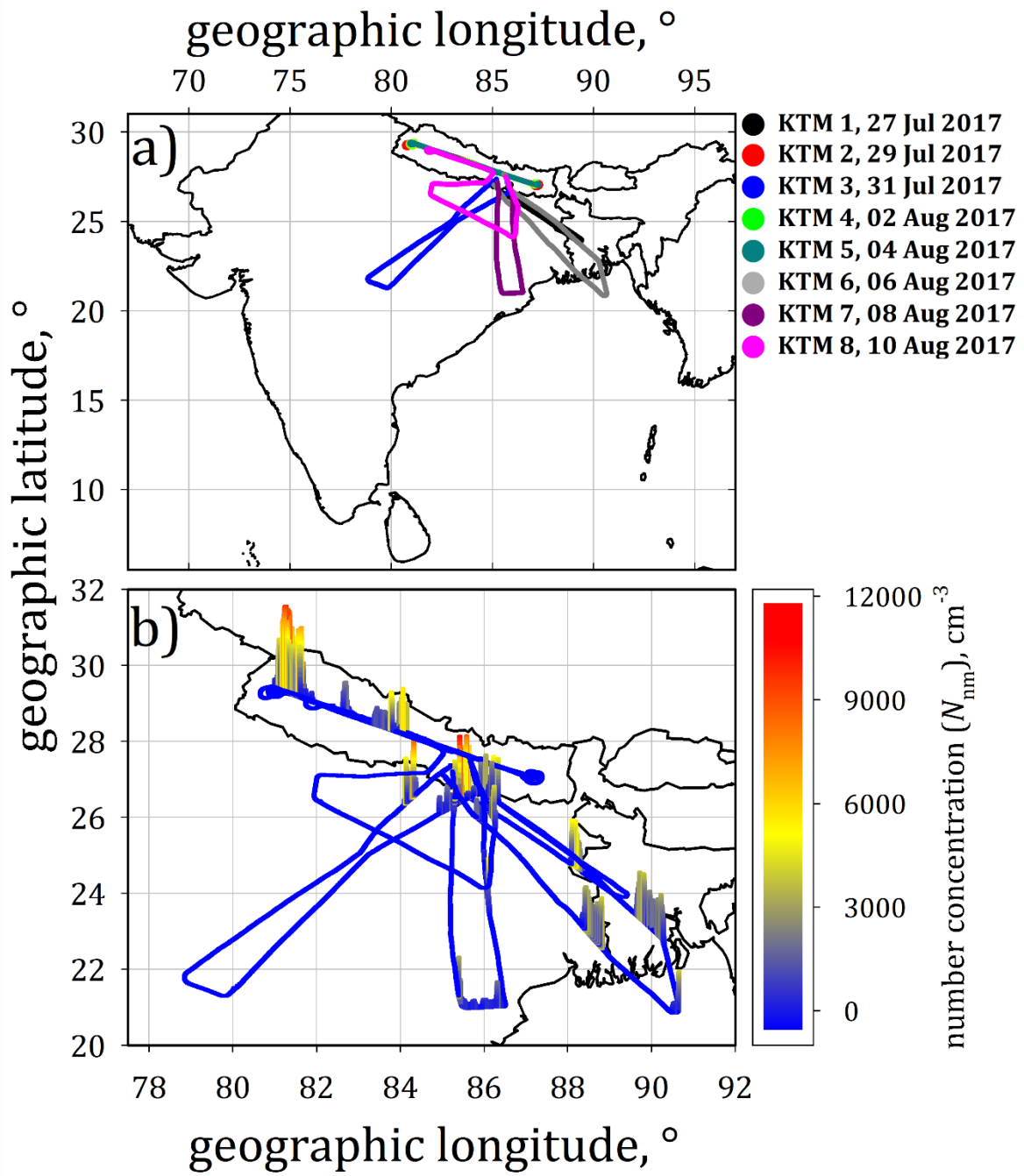
1825

1826

1827

1828

1829 **Figure 1**



1830
1831
1832
1833
1834
1835
1836
1837
1838
1839
1840
1841
1842
1843
1844
1845
1846
1847
1848
1849
1850
1851
1852
1853
1854
1855
1856

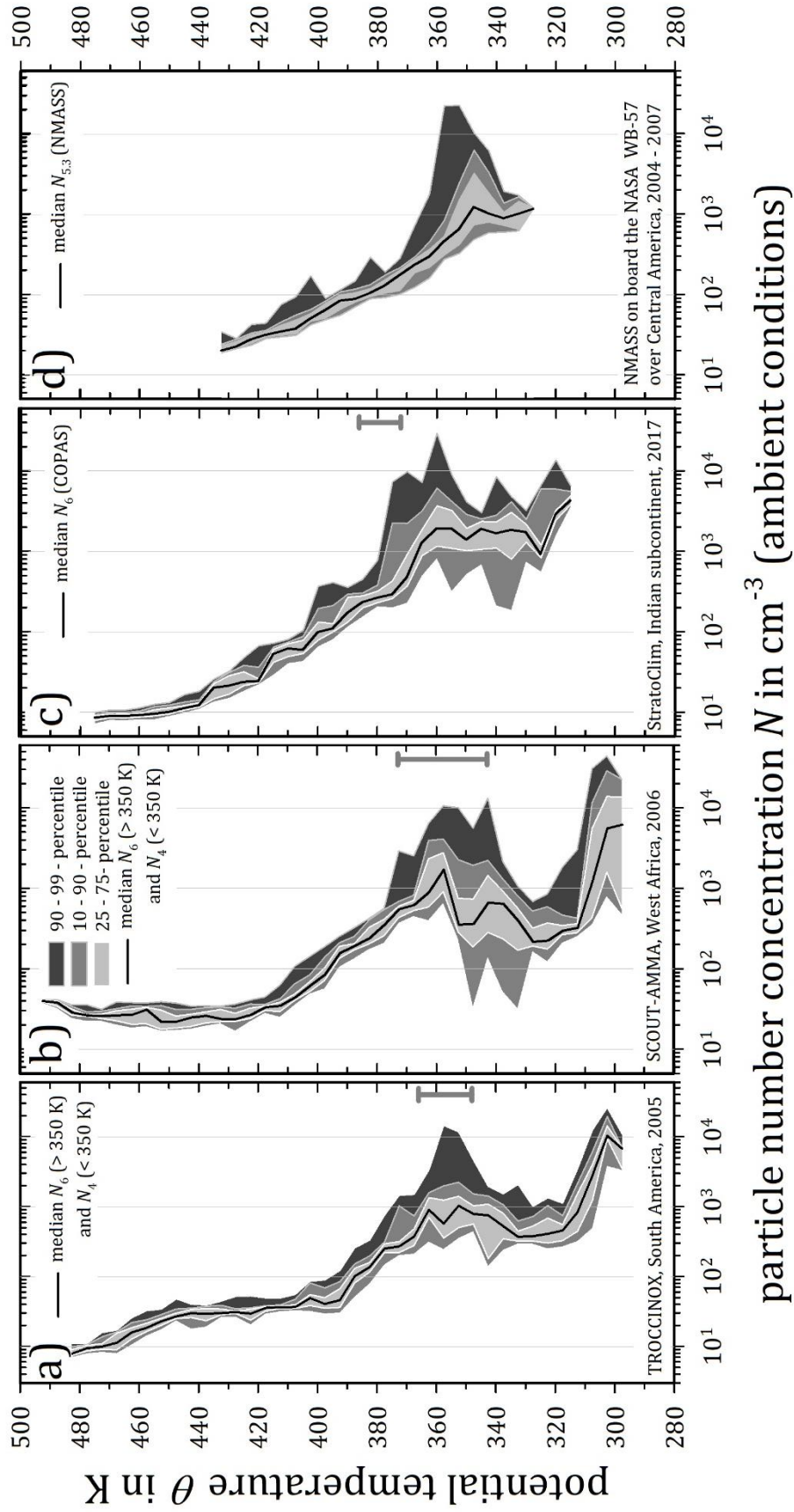


Figure 2

1857
 1858
 1859
 1860
 1861
 1862
 1863
 1864
 1865
 1866
 1867
 1868
 1869
 1870
 1871
 1872
 1873
 1874
 1875
 1876
 1877
 1878
 1879
 1880
 1881
 1882
 1883

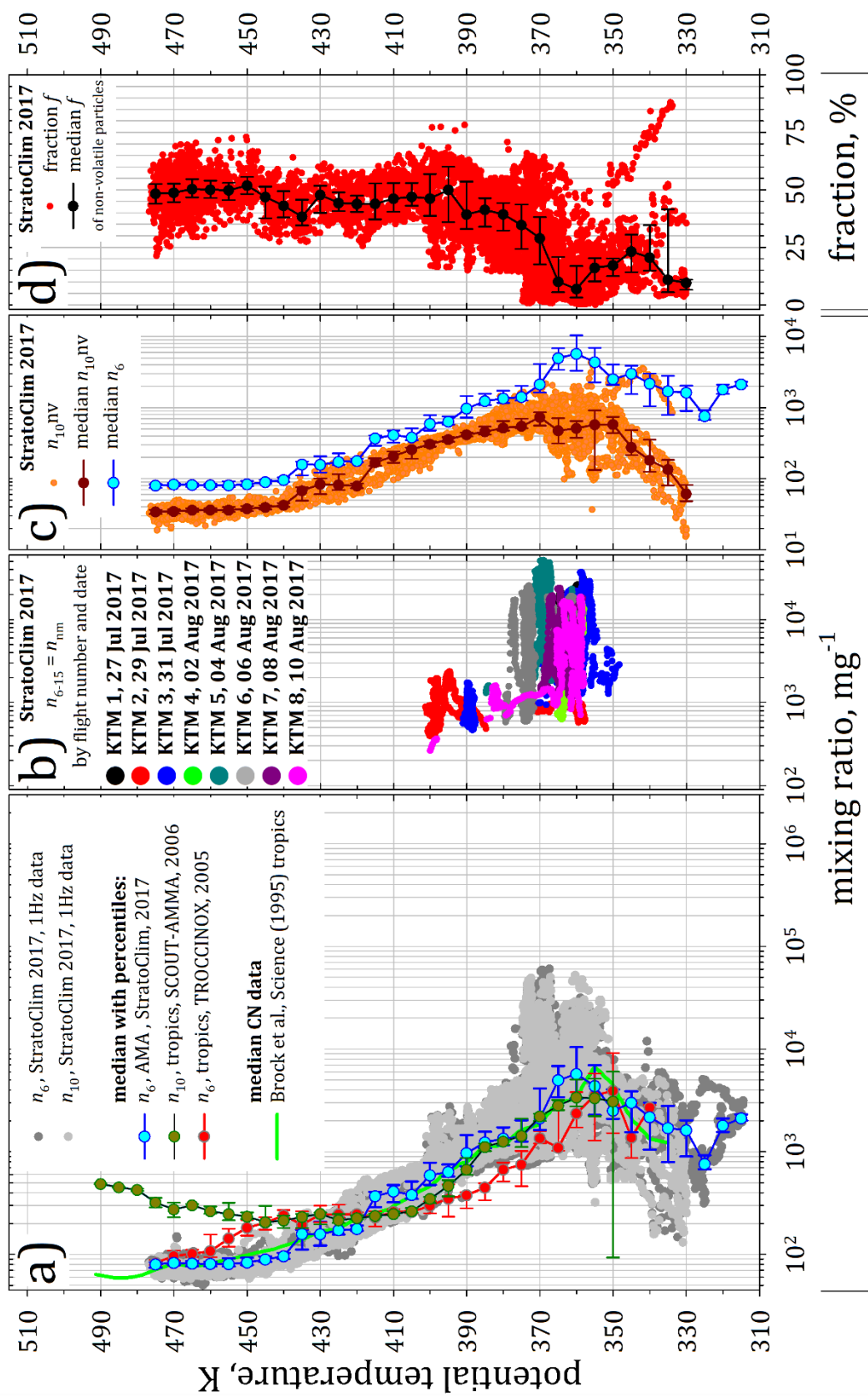


Figure 3

1884
1885
1886
1887
1888
1889
1890
1891
1892
1893
1894
1895
1896
1897
1898
1899
1900
1901
1902
1903
1904
1905
1906
1907
1908
1909
1910

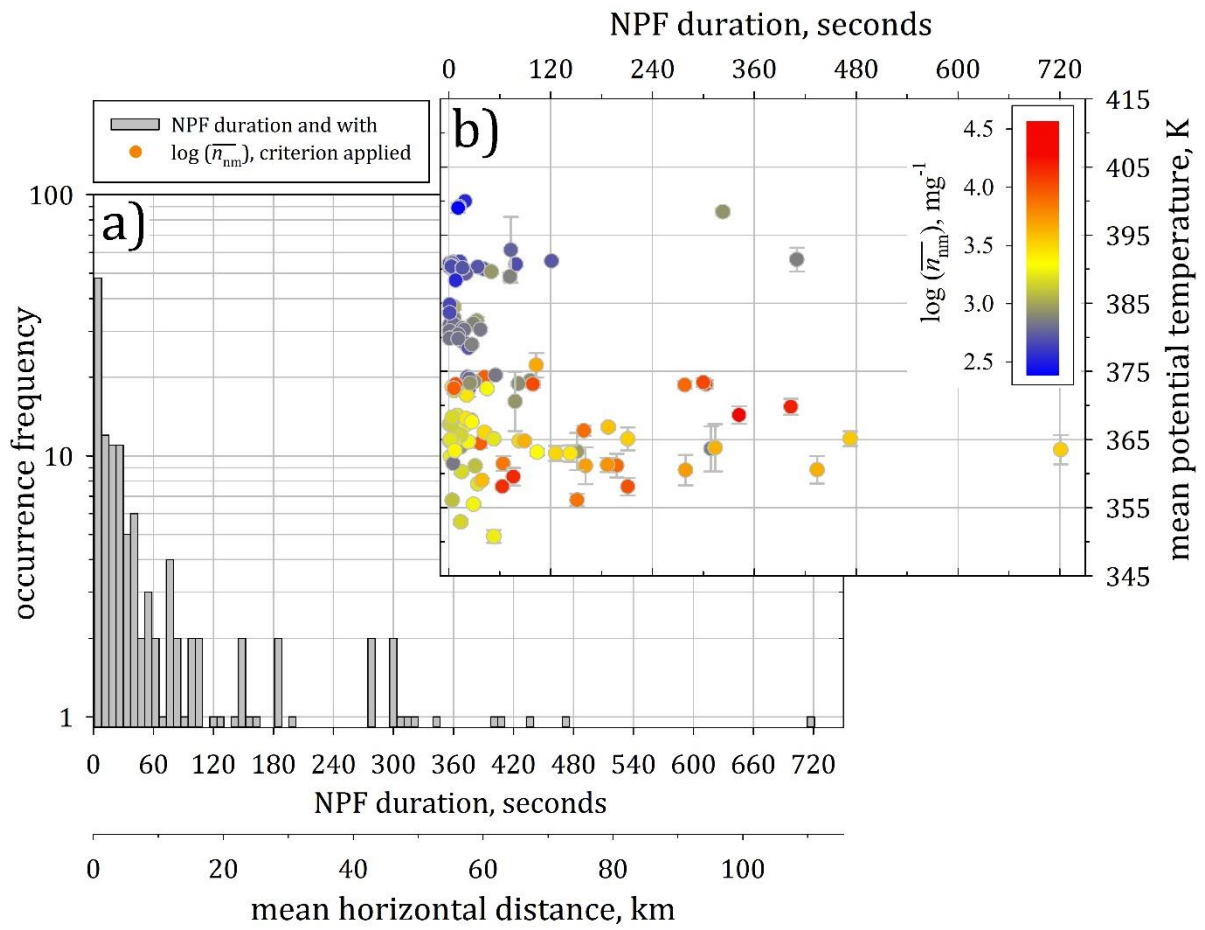


Figure 4

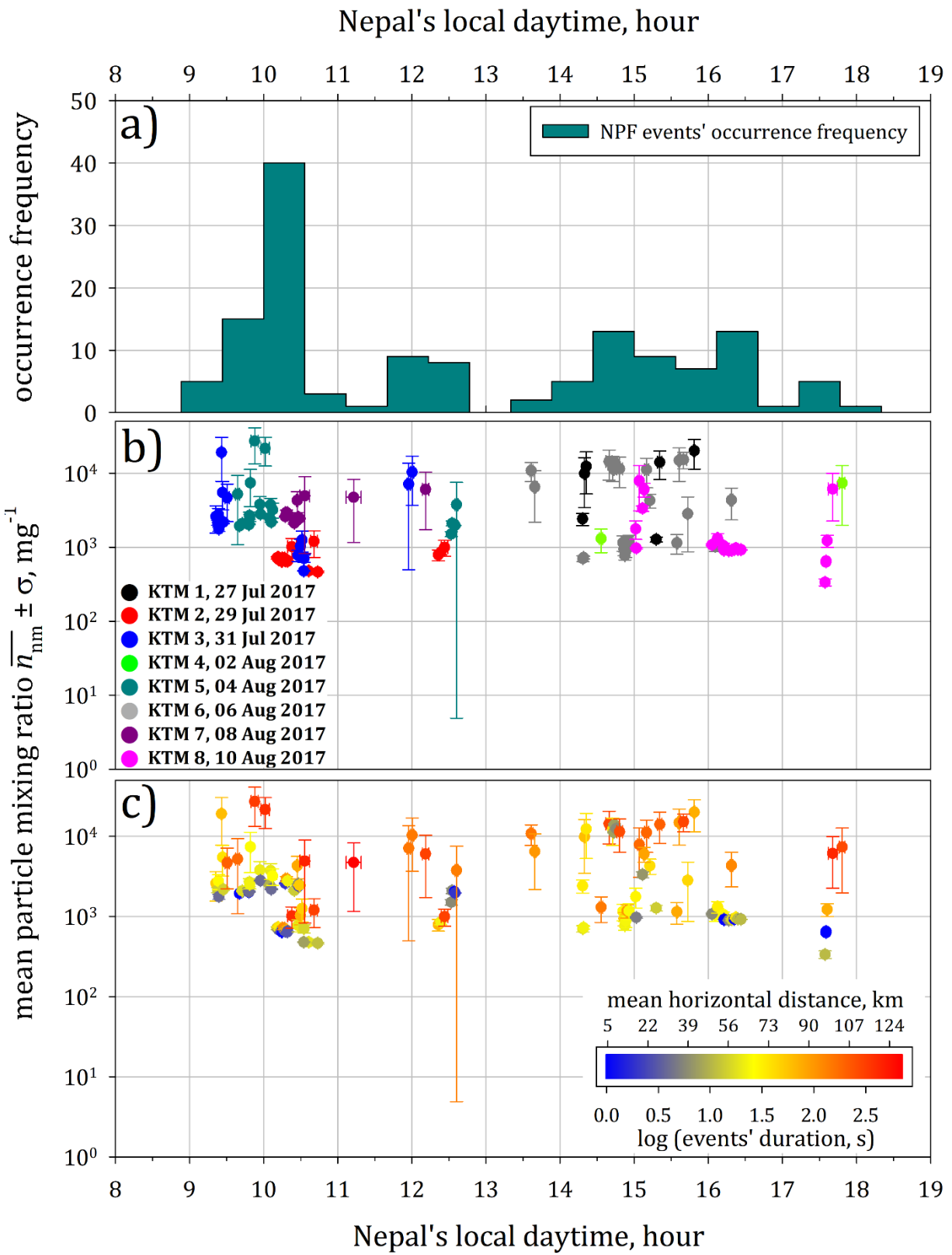


Figure 5

1938
 1939
 1940
 1941
 1942
 1943
 1944
 1945
 1946
 1947
 1948
 1949
 1950
 1951
 1952
 1953
 1954
 1955
 1956
 1957
 1958
 1959
 1960
 1961
 1962
 1963
 1964

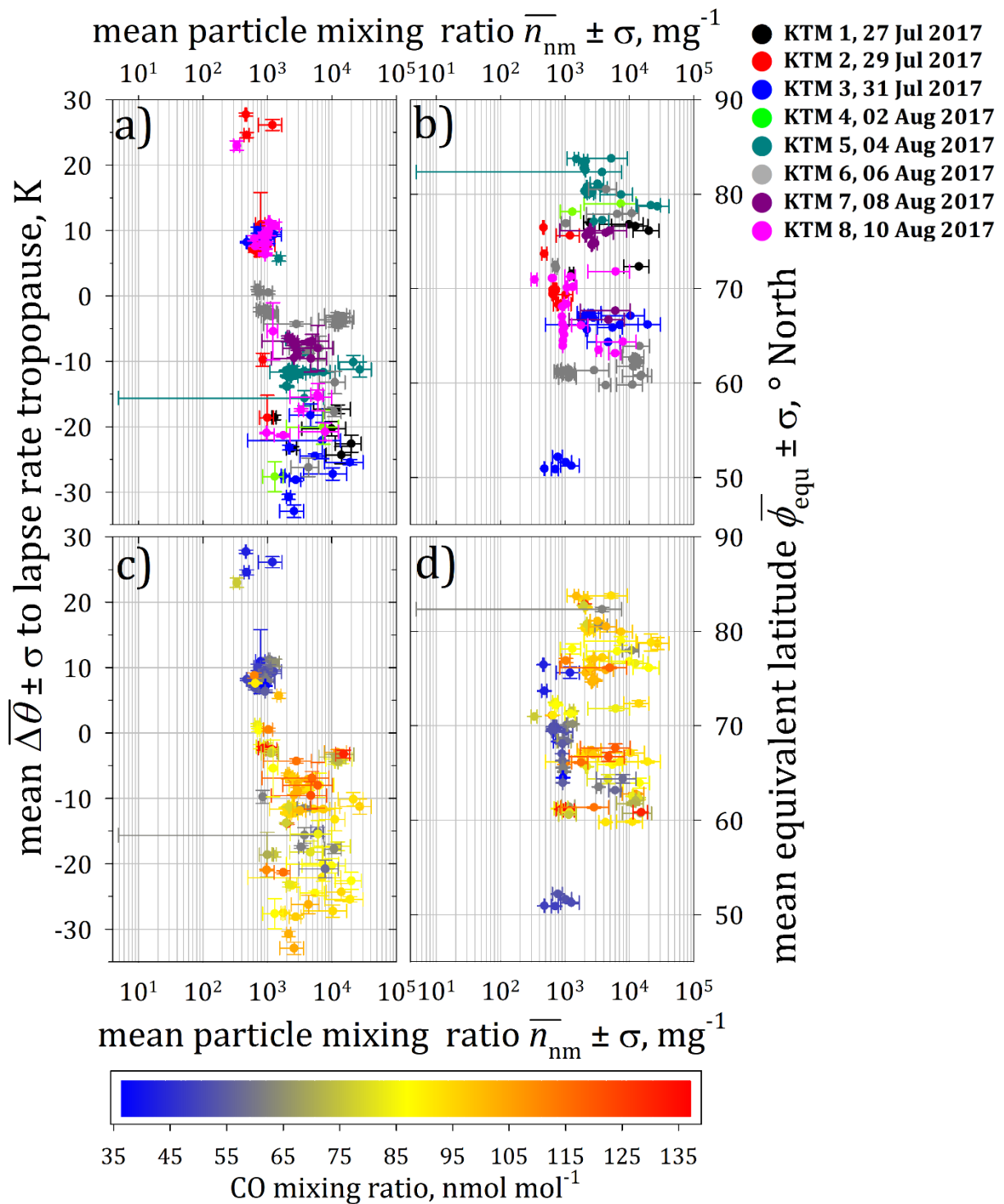


Figure 6

1965
 1966
 1967
 1968
 1969
 1970
 1971
 1972
 1973
 1974
 1975
 1976
 1977
 1978
 1979
 1980
 1981
 1982
 1983
 1984
 1985
 1986
 1987
 1988
 1989
 1990

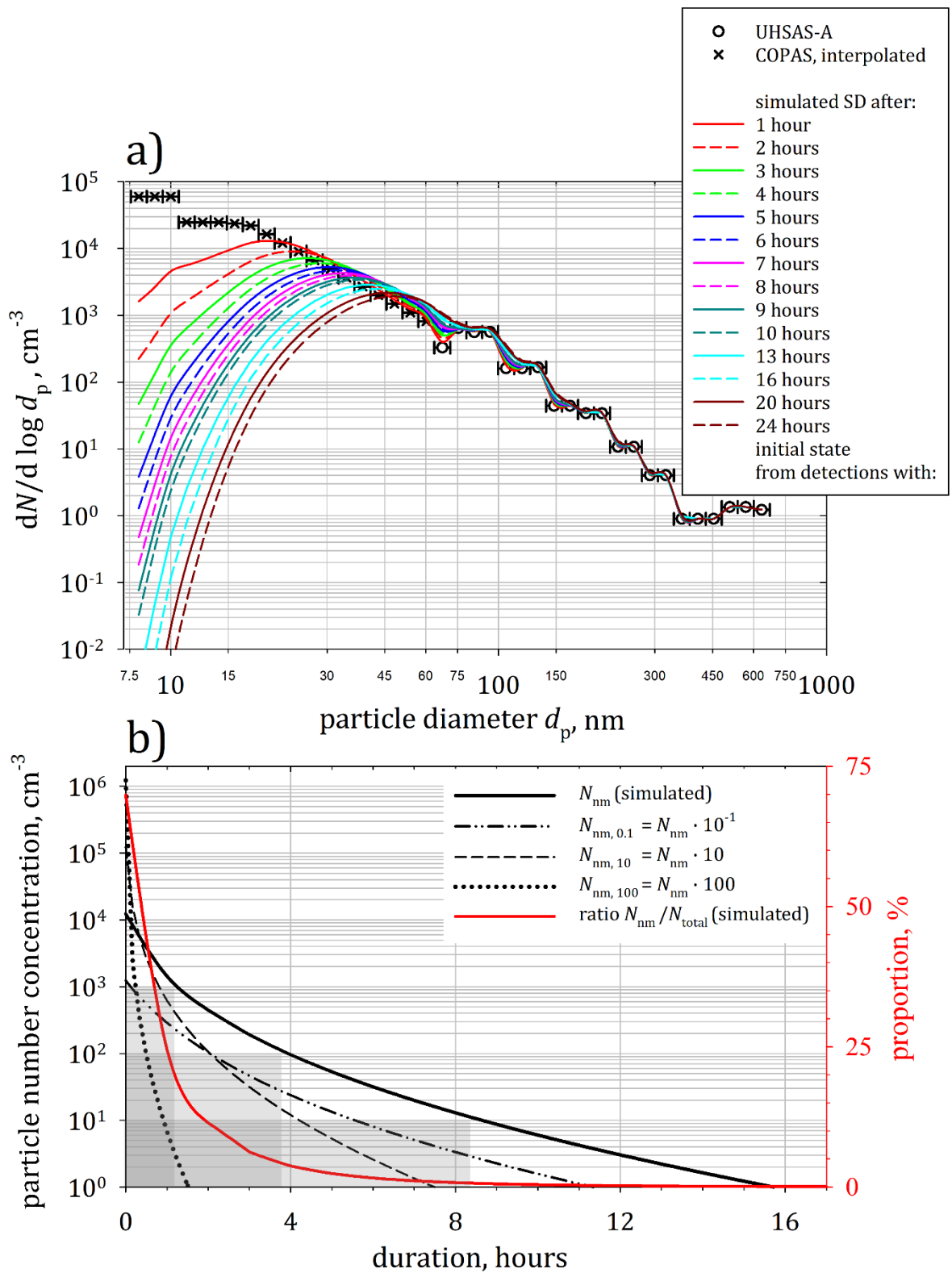


Figure 7

1991
1992
1993
1994
1995
1996
1997
1998
1999
2000
2001
2002
2003
2004
2005
2006
2007
2008
2009
2010
2011
2012
2013
2014
2015
2016

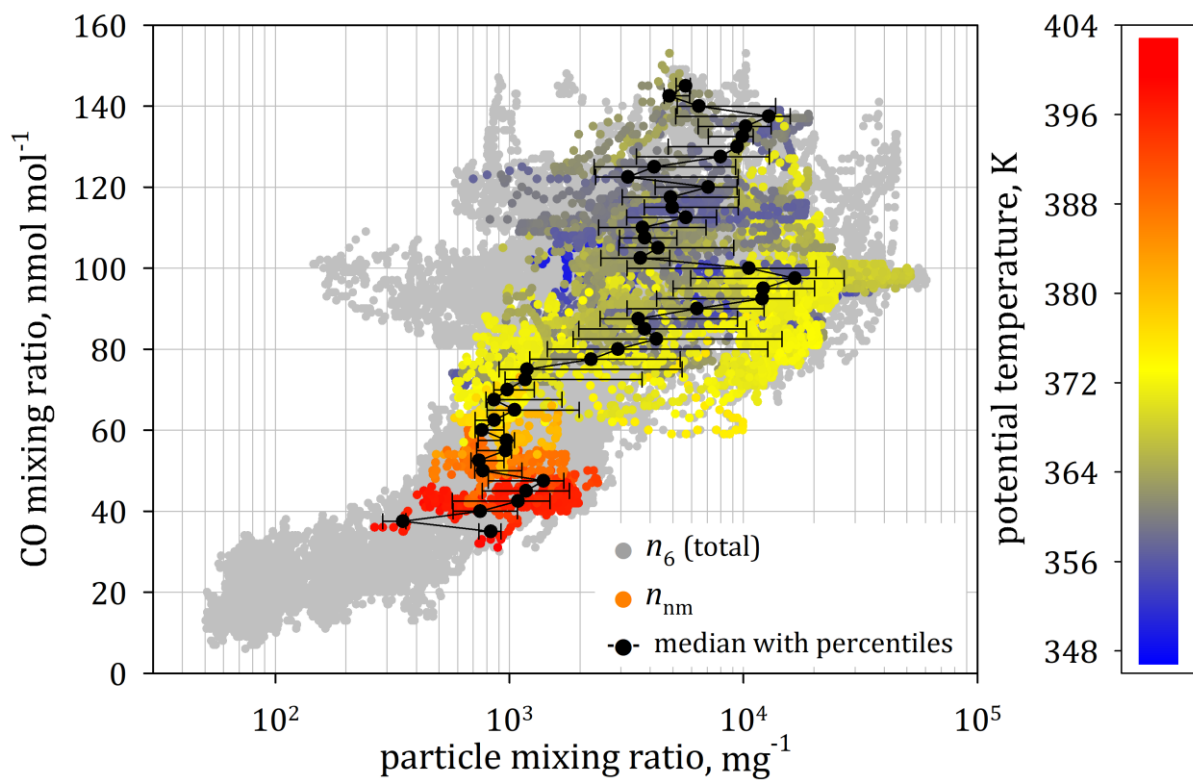
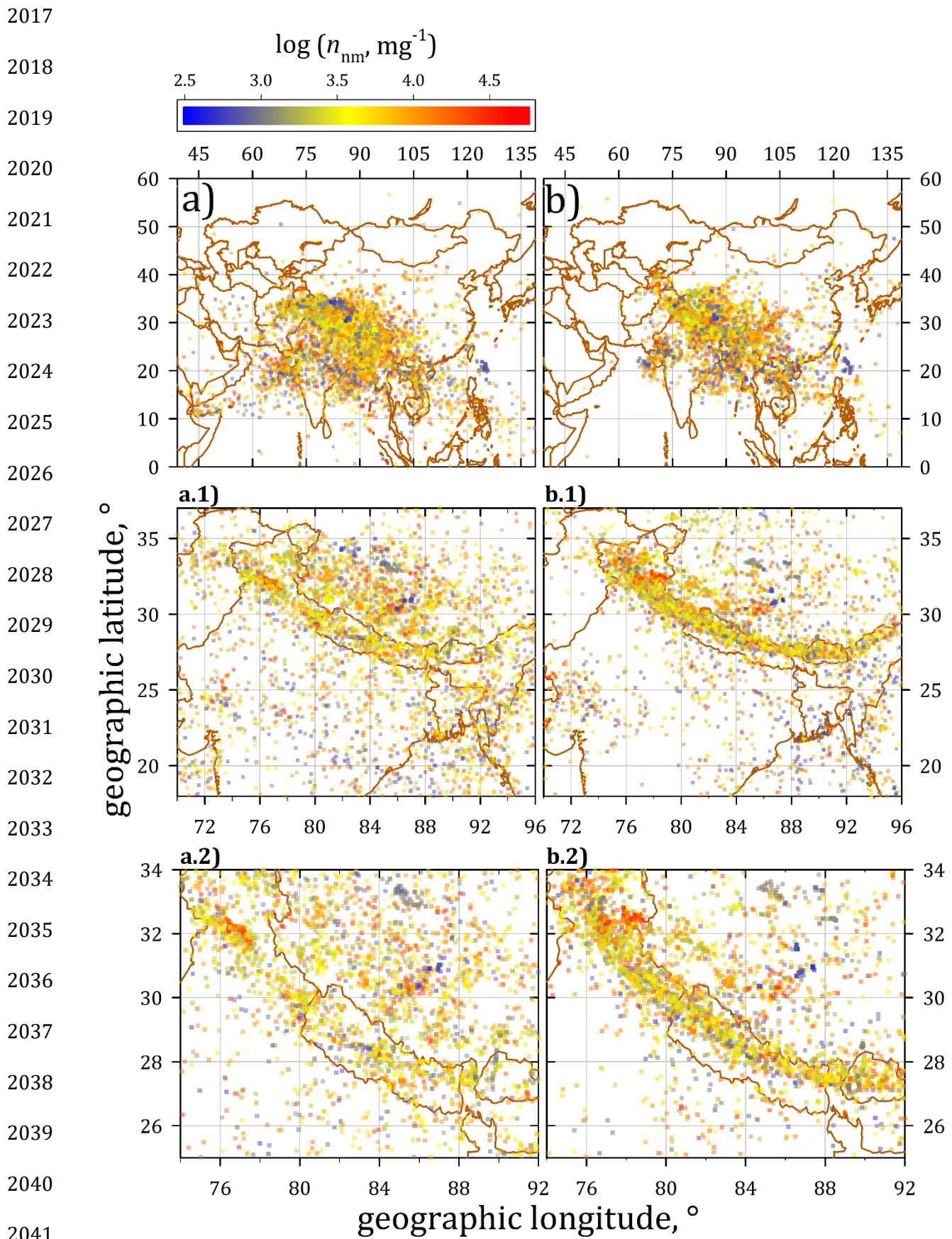


Figure 8



2043
2044
2045
2046
2047
2048
2049
2050
2051
2052
2053
2054
2055
2056
2057
2058
2059
2060
2061
2062
2063
2064
2065
2066
2067
2068

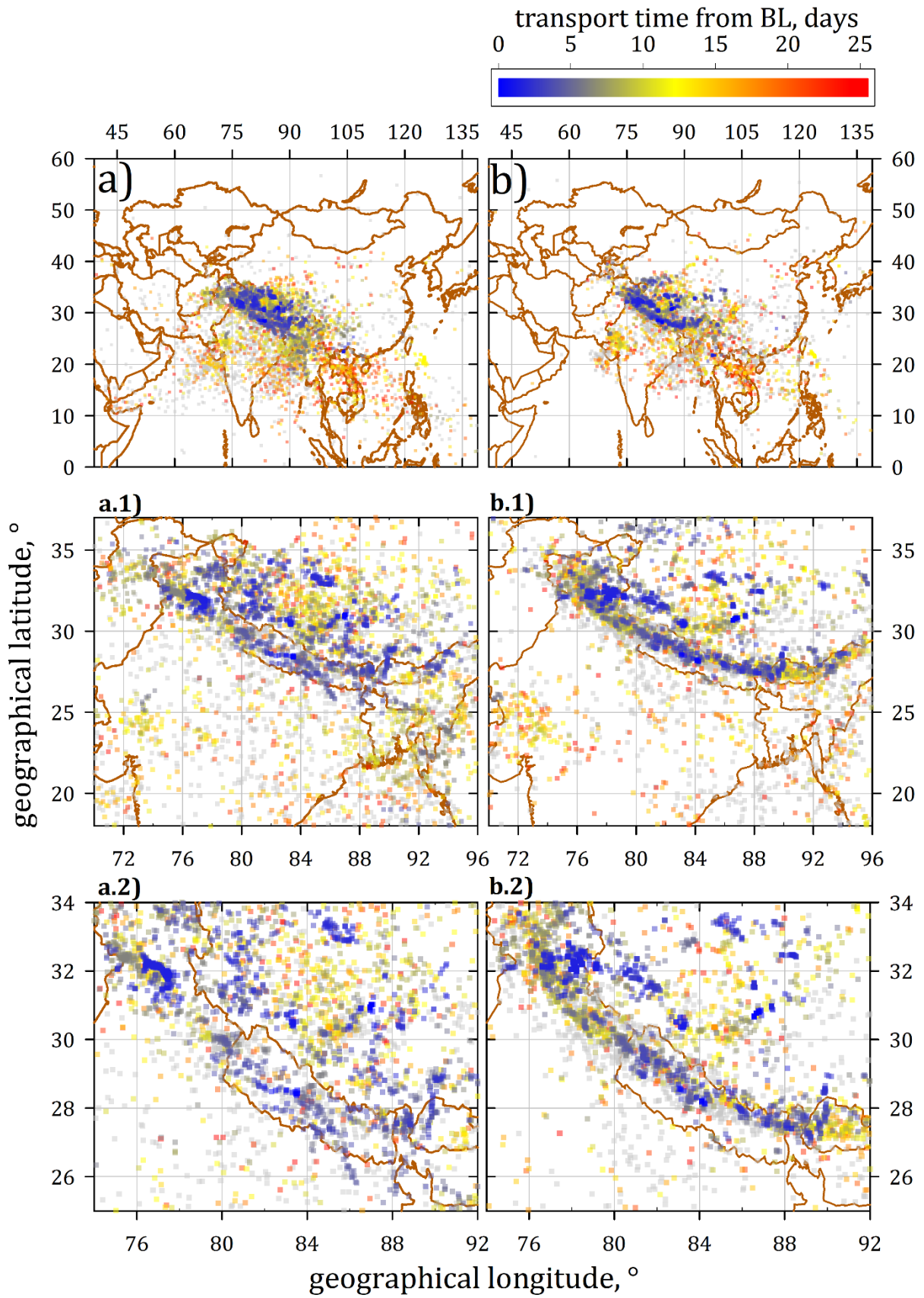


Figure 10

2069
2070
2071
2072
2073
2074
2075
2076
2077
2078
2079
2080
2081
2082
2083
2084
2085
2086
2087
2088
2089
2090
2091
2092
2093
2094
2095

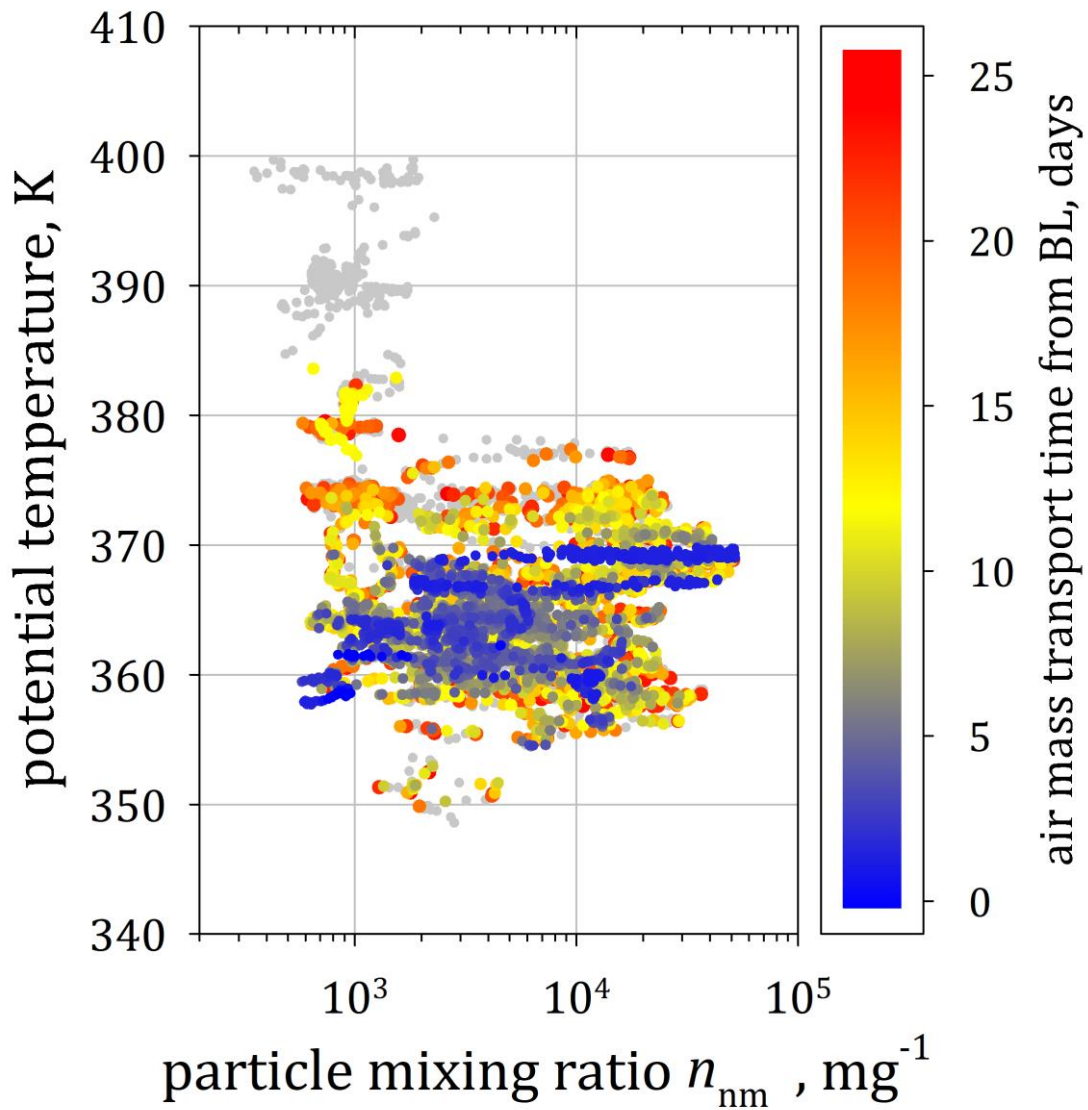


Figure 11

2096
2097
2098
2099
2100
2101
2102
2103
2104
2105
2106
2107
2108
2109
2110
2111
2112
2113
2114
2115
2116
2117
2118
2119
2120
2121
2122
2123
2124

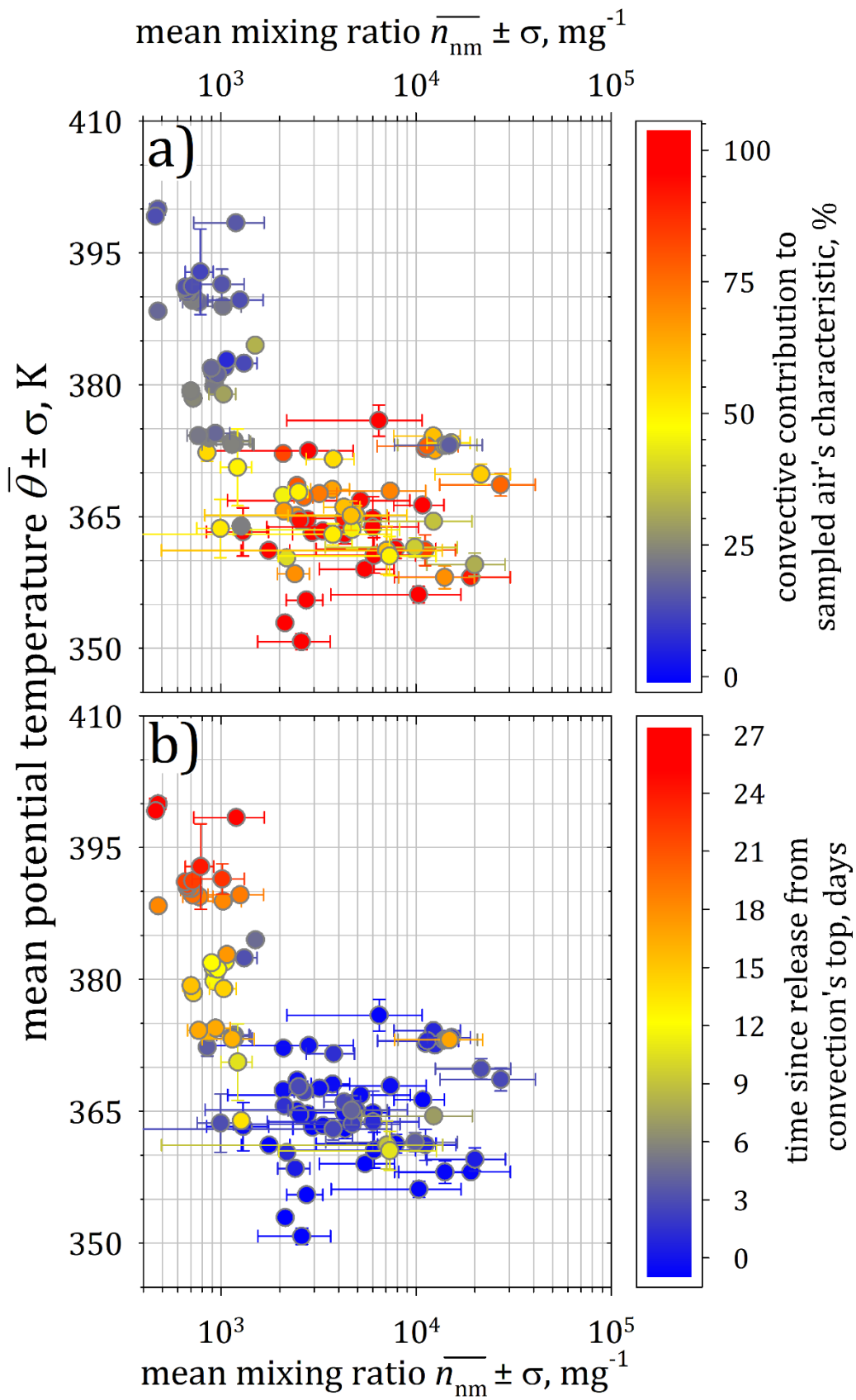


Figure 12

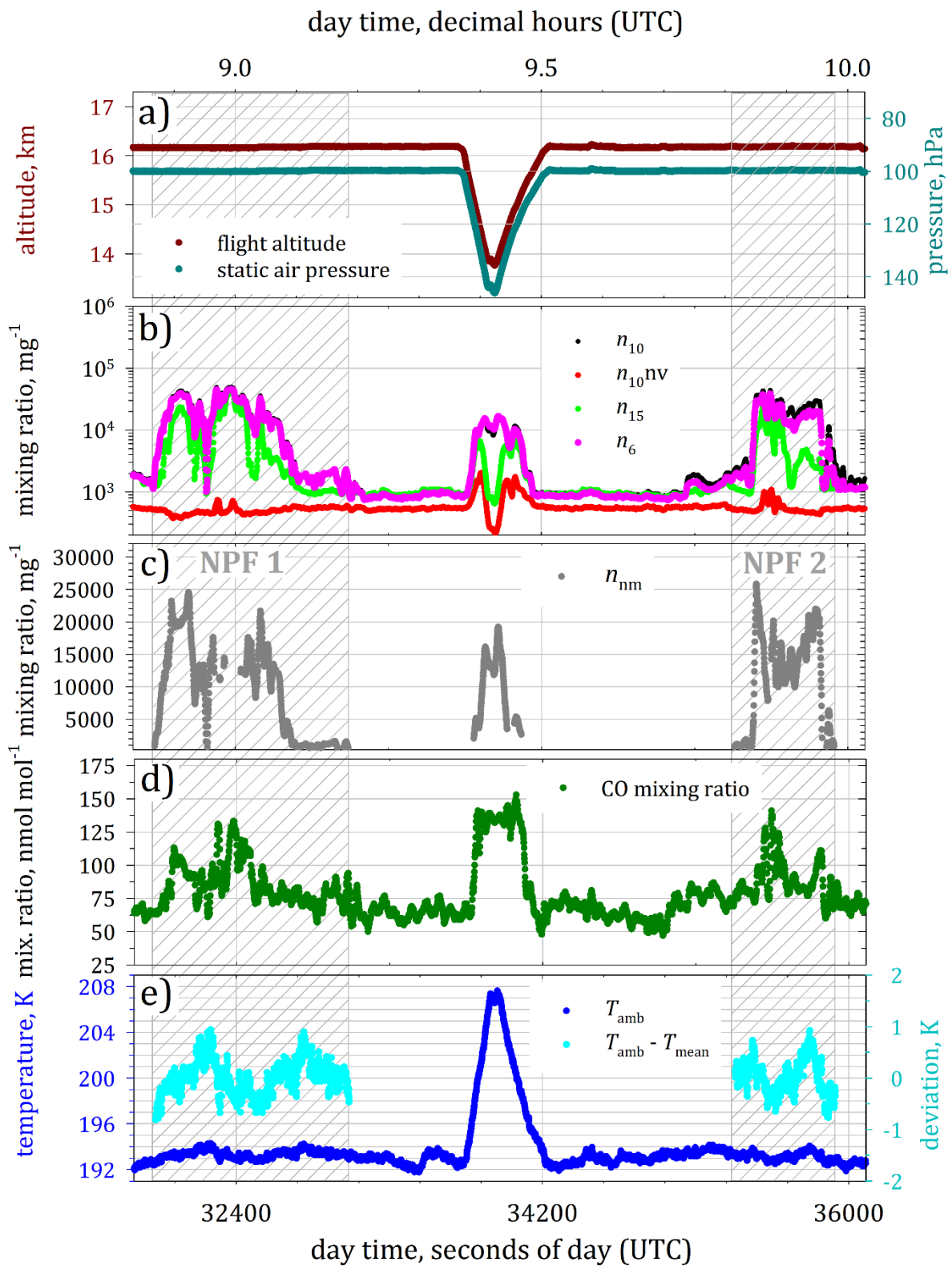


Figure 13

2153
2154
2155
2156
2157
2158
2159
2160
2161
2162
2163
2164
2165
2166
2167
2168
2169
2170
2171
2172
2173
2174
2175
2176
2177
2178
2179
2180
2181

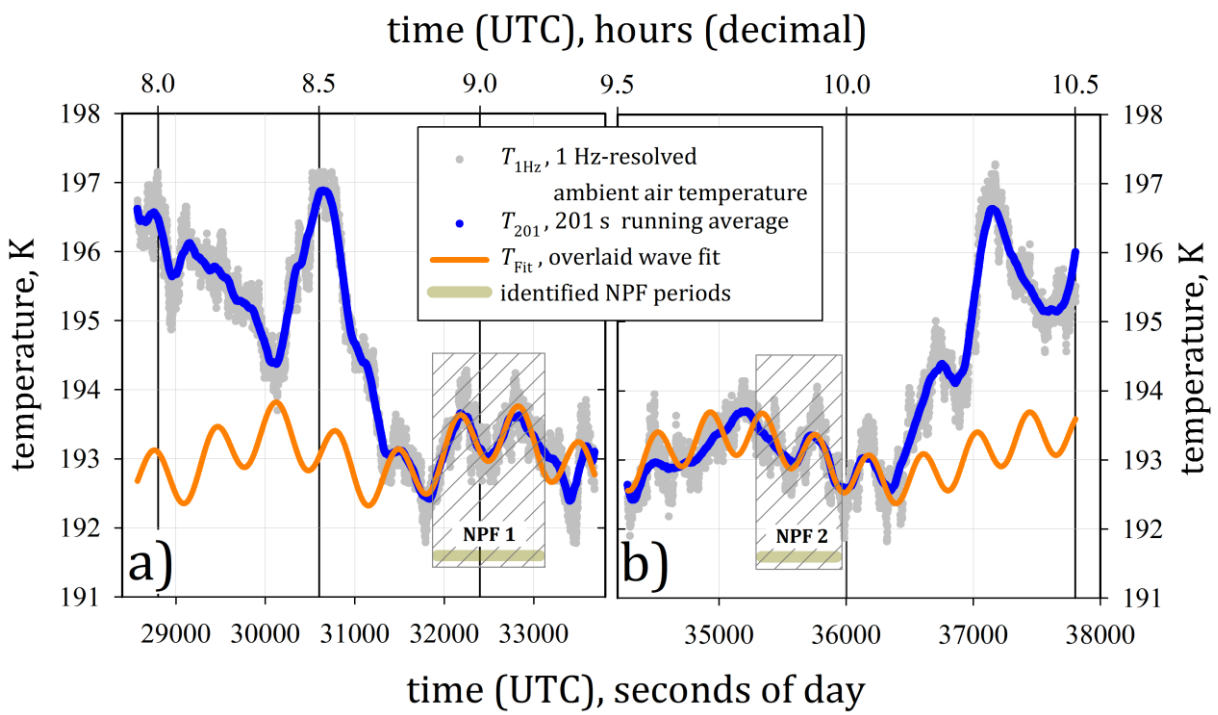


Figure 14

2182
2183
2184
2185
2186
2187
2188
2189
2190
2191
2192
2193
2194
2195
2196
2197
2198
2199
2200
2201
2202
2203
2204
2205
2206
2207
2208
2209
2210

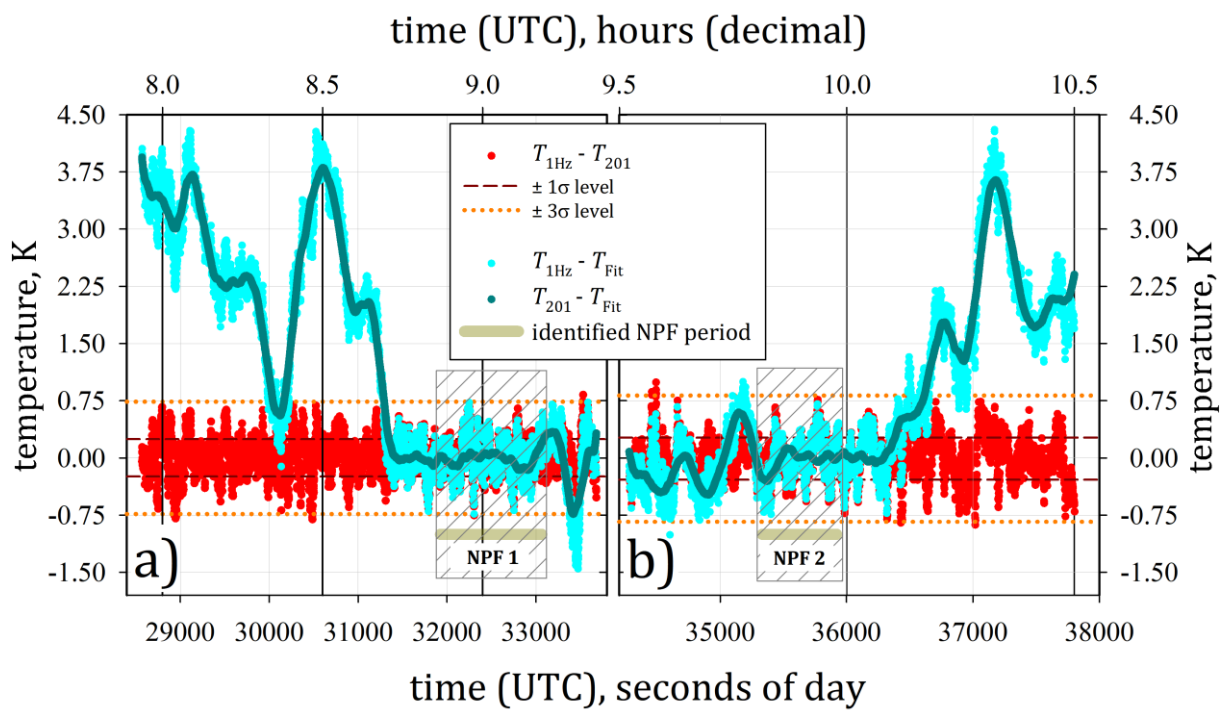


Figure A- 1

2211
2212
2213
2214
2215
2216
2217
2218
2219
2220
2221
2222
2223
2224
2225
2226
2227
2228
2229
2230

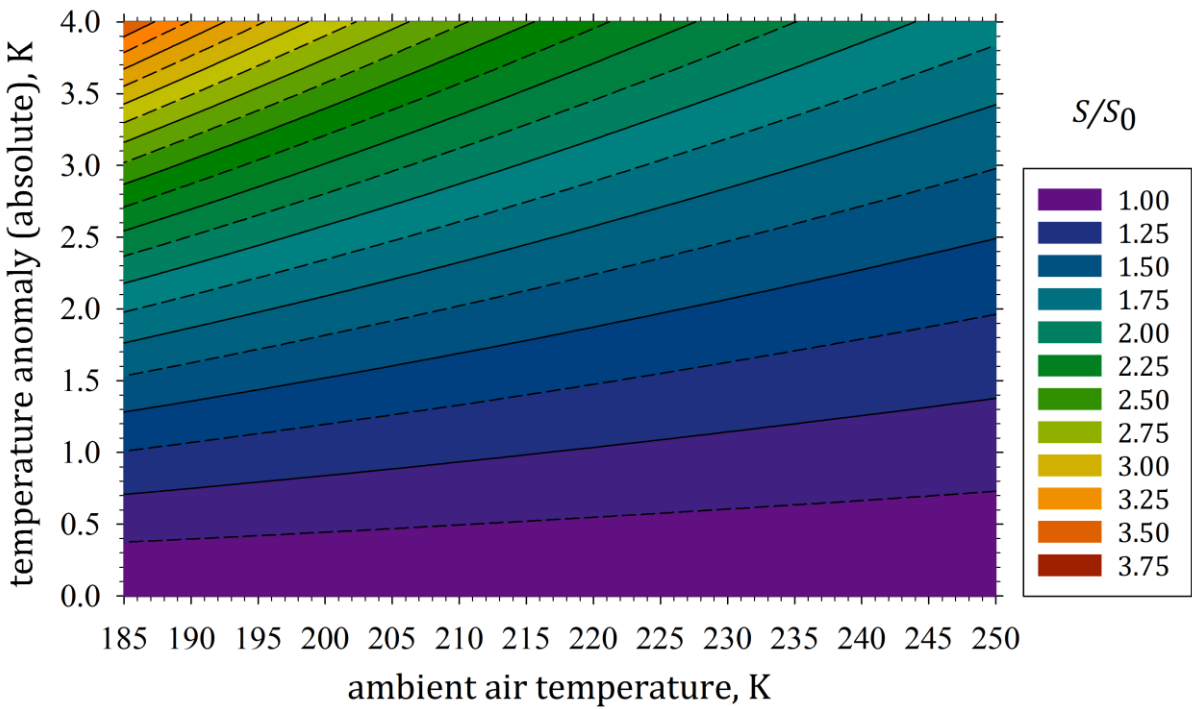


Figure A- 2

2231 **Tables**
 2232

pressure, hPa	particle diameter, nm										$\bar{\Lambda}_{6-15}$, %	κ_L (dimensionless)
	6	7	8	9	10	11	12	13	14	15		
	particle size dependent transmission efficiency, %											
80	60	65	70	74	77	79	81	82.5	84	85	24.25	1.32
150	70	75	77.5	81	83	84.5	86.5	87.5	88.5	89	17.75	1.22
300	77.5	81.5	84	86.5	88	89.5	90.5	91.5	92	92.5	12.65	1.14
400	80	83	85	87.5	89	90.5	91.5	92	92.8	93.5	11.52	1.13

2233

2234 **Table 1**

2235 Pressure-dependent corrections κ_L for number concentrations of nucleation-mode particles due
 2236 to particle losses ($\bar{\Lambda}_{6-15}$) in the aerosol line configuration (both COPAS instruments attached to a
 2237 single aerosol inlet) as deployed during StratoClim 2017, by using the Particle Loss Calculator
 2238 (von der Weiden et al., 2009) modified for low pressure applications. $\kappa_L = 100/(100-\bar{\Lambda}_{6-15})$,
 2239 correspondingly to Weigel et al. (2009).

	$T_{Fit} = f(x, a, b, c, d) + f'(x, a', b', c', d')$							
	<i>a</i>	<i>b</i>	<i>c</i>	<i>d</i>	<i>a'</i>	<i>b'</i>	<i>c'</i>	<i>d'</i>
NPF period 1	0.35	0.0025	1.75	193.05	0.42	0.00925	-0.6	0
NPF period 2	0.35	0.0025	1.75	193.05	0.33	0.015	-0.8	0

2240

2241 **Table 2**

2242 List of parameters of the wave fit to identify the wave-character of two temperature anomalies,
 2243 which were coincidentally observed with two NPF events, respectively, during the StratoClim
 2244 flight KTM 6 on 06 August 2017.